

A 5902 II

Dr.6

POLISH ACADEMY OF SCIENCES – WROCLAW BRANCH

WROCLAW UNIVERSITY OF TECHNOLOGY

Biblioteka Główna i OINT
Politechniki Wrocławskiej



100100354456

ISSN 1644-9665
INDEX 375667



ARCHIVES OF CIVIL AND MECHANICAL ENGINEERING

**Quarterly
Vol. V, No. 4**

WROCLAW 2005

ADVISORY COMMITTEE

Chairman – JAN KMITA¹

JAN BILISZCZUK (Poland)
CZESLAW CEMPEL (Poland)
JERZY GRONOSTAJSKI (Poland)
ANTONI GRONOWICZ (Poland)
M.S.J. HASHMI (Ireland)
HENRYK HAWRYLAK (Poland)
RYSZARD IZBICKI (Poland)
WACLAW KASPRZAK (Poland)
MICHAEL KETTING (Germany)
MICHAŁ KLEIBER (Poland)
VADIM L. KOŁMOGOROV (Russia)

ADOLF MACIEJNY (Poland)
ZDZISŁAW MARCINIĄK (Poland)
KAZIMIERZ RYKALUK (Poland)
ANDRZEJ RYŻYŃSKI (Poland)
ZDZISŁAW SAMSONOWICZ (Poland)
WOJCIECH SZCZEPIŃSKI (Poland)
PAWEŁ ŚNIADY (Poland)
RYSZARD TADEUSIEWICZ (Poland)
TARRAS WANHEIM (Denmark)
WŁADYSŁAW WŁOSIŃSKI (Poland)
JERZY ZIÓŁKO (Poland)
JÓZEF ZASADZIŃSKI (Poland)

EDITORIAL BOARD

Editor-in-chief – JERZY GRONOSTAJSKI²

ROBERT ARRIEUX (France)
AUGUSTO BARATA DA ROCHA (Portugal)
GHEORGHE BRABIE (Romania)
LESŁAW BRUNARSKI (Poland)
EDWARD CHLEBUS (Poland)
L. DEMKOWICZ (USA)
KAZIMIERZ FLAGA (Poland)
YOSHINOBI FUJITANI (Japan)
FRANCISZEK GROSMAN (Poland)
MIECZYŚLAW KAMIŃSKI (Poland)
Scientific secretary – SYLWESTER KOBIELAK

ANDRZEJ KOCAŃDA (Poland)
WACŁAW KOLLEK (Poland)
PIOTR KONDERLA (Poland)
ZBIGNIEW KOWAL (Poland)
TED KRAUTHAMMER (USA)
ERNEST KUBICA (Poland)
KRZYSZTOF KURZYDŁOWSKI (Poland)
TADEUSZ MIKULCZYŃSKI (Poland)
HARTMUT PASTERNAK (Germany)
MACIEJ PIETRZYK (Poland)
EUGENIUSZ RUSIŃSKI (Poland)
HANNA SUCHNICKA (Poland)

¹ The Faculty of Civil Engineering, Wrocław University of Technology
Wybrzeże Wyspiańskiego 27, 50-370 Wrocław, Poland
Tel. +48 71 320 41 35, Fax. +48 71 320 41 05, E-mail: jan.kmita@pwr.wroc.pl

² The Faculty of Mechanical Engineering, Wrocław University of Technology
ul. Łukasiewicza 5, 50-371 Wrocław, Poland
Tel. +48 71 320 21 73, Fax. +48 71 320 34 22, E-mail: jerzy.gronostajski@itma.pwr.wroc.pl

POLISH ACADEMY OF SCIENCES – WROCLAW BRANCH
WROCLAW UNIVERSITY OF TECHNOLOGY

DAR



ARCHIVES OF CIVIL AND MECHANICAL ENGINEERING

Quarterly
Vol. V, No. 4

WROCLAW 2005

EDITOR IN CHIEF

JERZY GRONOSTAJSKI

EDITORIAL LAYOUT AND PROOF-READING

EWA SOBESTO, SEBASTIAN ŁAWRUSEWICZ

SECRETARY

TERESA RYGŁOWSKA

Publisher: Committee of Civil and Mechanical Engineering
of Polish Academy of Sciences – Wrocław Branch,
Faculty of Civil Engineering and Faculty of Mechanical Engineering
of Wrocław University of Technology

© Copyright by Oficyna Wydawnicza Politechniki Wrocławskiej, Wrocław 2005

OFICYNA WYDAWNICZA POLITECHNIKI WROCŁAWSKIEJ
Wybrzeże Wyspiańskiego 27, 50-370 Wrocław

ISSN 1644-9665

Drukarnia Oficyny Wydawniczej Politechniki Wrocławskiej. Zam. nr 1191/2005.

Contents

M. NAPIÓRKOWSKA-ALYKOW, W. GLABISZ, Parametric identification procedure based on the Walsh wavelet packet approach for estimation of signal function derivatives	5
Ł. KONAT, G. PEKALSKI, J. RABIEGA, U. SACHADEL, Material tests of a bridge from 1796 over the Strzegomka River in Łażany, Lower Silesia	27
A. BIEGUS, D. WOJCZYSZYN, Coefficients of buckling length of chords for out-of-plane instability of small-bay trusses	43
D. BĘBEN, Z. MAŃKO, Tests of arch bridge made from corrugated steel plates	53
K. NADOLNY, B. BALASZ, Modelling the surfaces of grinding wheels whose structure is zonally diversified	77
Cz.MACHELSKI, G. ANTONISZYN, Load rate of the circumferential sector of soil-steel bridge structures	85

Spis treści

M. NAPIÓRKOWSKA-ALYKOW, W. GLABISZ, Falkowa analiza pakietowa Walsha w wyznaczaniu pochodnych sygnału	5
Ł. KONAT, G. PEKALSKI, J. RABIEGA, U. SACHADEL, Badania materiałowe mostu na rzece Strzegonce wybudowanego w 1796 roku w Łażanach na Dolnym Śląsku	27
A. BIEGUS, D. WOJCZYSZYN, Współczynniki długości wyboczeniowej pasów z płaszczyzny ustroju „krótkich” kratownic	43
D. BĘBEN, Z. MAŃKO, Badania mostu łukowego wykonanego ze stalowych blach falistych	53
K. NADOLNY, B. BALASZ, Modelowanie powierzchni narzędzi ściernych o strefowo zróżnicowanej budowie	77
Cz.MACHELSKI, G. ANTONISZYN, Intensywność obciążenia wycinka obwodowego mostowej konstrukcji gruntowo-powłokowej.....	85

Parametric identification procedure based on the Walsh wavelet packet approach for estimation of signal function derivatives

M. NAPIÓRKOWSKA-AŁYKOW, W. GLABISZ

Wrocław University of Technology, Wybrzeże Wyspiańskiego 27, 50-370 Wrocław

The identification of mathematical models which can represent discrete dynamic systems is a problem of considerable importance in applied mechanics. The algorithm is tested on single degree of freedom system, which is described by linear and nonlinear differential equations with constant and variable coefficients.

Keywords: *wavelet analysis, parametric identification, Walsh packet basis*

1. Introduction

The identification of real system parameters is a major problem in mechanics. In parametric identification, the derivatives of the system signal measured (e.g. displacement, acceleration) are particularly difficult to determine accurately, all the more because the signal is randomly disturbed. The problem also arises in the case of inaccurate measurements and mathematical models with higher-order derivatives [1]. The determination of signal function derivatives is much more difficult in a numerical analysis than in a situation where, for instance, accelerations have been measured and velocities and deflections are to be determined by integration, using the identification procedure [2]. In integration, the determination of integration constants poses a problem.

The aim of the paper was to generalize the results presented in Glabisz's paper [3], with regard to the use of the Walsh wavelet packet analysis for determining signal function derivatives. Glabisz's results represent a special case of the general algorithm which is presented here. The algorithm is based on wavelet packet analysis and allows one to generate derivatives of an indicated order, which are used to identify the parameters of the mathematical models adopted that describe the system investigated.

Below, wavelet packet analysis (with the Haar filter employed) is briefly introduced. In section 3, derivative order determination procedures and the required multipliers are given. Section 4 discusses parametric identification procedures. In section 5, numerical examples based on the proposed identification method are provided. The paper ends with a recapitulation and conclusions.

2. Short introduction to the Walsh wavelet packet analysis

In the literature, one can find numerous applications of the wavelet transformation, mainly to mathematical problems [4–7]. The foundations of wavelet analysis can be found, among others, in [8, 9, 10]. A detailed review of the papers on the wavelet transformation is presented in [11].

In the discrete wavelet transform (DWT), the signal f investigated is presented as its decomposition into a smooth signal part (using the scaling function $\phi_{j_0,k}$) expressed by the coefficients $f_k^{j_0} = \langle \phi_{j_0,k}, f \rangle = \int_R f_{j_0}(t) \phi_{j_0,k}(t) dt$ and a part comprising signal function details (using the wavelet function $\psi_{j-1,k}$), expressed by the coefficients $d_k^{j-1} = \langle \psi_{j-1,k}, f \rangle = \int_R f_{j-1}(t) \psi_{j-1,k}(t) dt$, where j represents the successive resolution levels [8, 12]:

$$f(t) = \sum_k f_k^{j_0} \phi_{j_0,k}(t) + \sum_{l=j_0}^{\infty} \sum_k d_k^{l-1} \psi_{l-1,k}(t). \quad (1)$$

Equation (1) shows that the function $f(t)$ can be decomposed into a smooth part $f_j(t)$ and the part $d_j(t)$ representing local fluctuations. In wavelet analysis, the smooth part of the signal function is decomposed into a smooth part and a details part, while the details part from the higher level is left unchanged [8, 9, 10, 12]. As opposed to the wavelet transformation, in wavelet packet analysis the details part is also subjected to decomposition into a smooth part and a details part. In classic wavelet analysis, the space V can be decomposed into orthogonal subspaces in which base functions are defined by the following equations [8, 9]:

$$\phi(t) = \sum_k h_k \phi_{1k}(t) = \sqrt{2} \sum_k h_k \phi(2t - k), \quad (2)$$

where h_k are the low-pass filter coefficients,

$$\psi(t) = \sqrt{2} \sum_k g_k \phi(2t - k), \quad (3)$$

where g_k are the wavelet expansion coefficients referred to as high-pass filter coefficients [8, 9, 10, 12]. In wavelet packet analysis, a similar division can be applied to the details space W .

In a general case, for $n = 0, 1, \dots$, one can define the following functions [13, 14]:

$$w_{2n}(t) = \sqrt{2} \sum_k h_k w_n(2t - k), \quad (4)$$

$$w_{2n+1}(t) = \sqrt{2} \sum_k g_k w_n(2t - k) \quad (5)$$

which form the sequences of base functions in the space V_j . The different combinations of functions (4) and (5) and the functions created through scaling and translating them form a set of orthonormal bases $\{w_n(t)\}$ which may be used to describe the space elements V_j . Such a collection of base functions is called a library of packet bases and functions $w_{n,j,k} = 2^{j/2} w_n(2^j t - k)$ are referred to as a wavelet packet. An exemplary scheme of the space V_3 decomposition by wavelet packet analysis for a space with base $\{w_{n,j,k}(t)\}$ denoted as $w_{n,j}$ is shown in Figure 1.

$w_{0,3}$							
$w_{0,2}$				$w_{1,2}$			
$w_{0,1}$		$w_{1,1}$		$w_{2,1}$		$w_{3,1}$	
$w_{0,0}$	$w_{1,0}$	$w_{2,0}$	$w_{3,0}$	$w_{4,0}$	$w_{5,0}$	$w_{6,0}$	$w_{7,0}$

Fig. 1. Scheme of the space V_3 decomposition by wavelet analysis

In this paper, wavelet packets generated from the Haar filters for which $h_0 = h_1 = g_0 = -g_1 = 1/\sqrt{2}$ are used. For example, the Haar wavelet base \mathbf{H} (one of the potential packet bases) has the following discrete representation (at $j = 3$) [1]:

$$\mathbf{H}_{8 \times 8} = \begin{bmatrix} 1 & 1 & 1 & 1 & 1 & 1 & 1 & 1 \\ 1 & 1 & 1 & 1 & -1 & -1 & -1 & -1 \\ 1 & 1 & -1 & -1 & & & & \\ & & & & 1 & 1 & -1 & -1 \\ 1 & -1 & & & & & & \\ & & 1 & -1 & & & & \\ & & & & 1 & -1 & & \\ & & & & & & 1 & -1 \end{bmatrix} \quad (6)$$

The function $w_{0,0}$ shown in the packet analysis algorithm chart (Figure 1) forms the first row of the Haar packet base \mathbf{H} . The second row of the matrix \mathbf{H} corresponds to the base function $w_{1,0}$ in the chart. Two base functions of the packet base $w_{1,1}$ form the third row and the fourth row. Rows 5, 6, 7 and 8 of the matrix \mathbf{H} represent four base functions of the packet base $w_{1,2}$. The Haar filter-based wavelet bases $\{w_n(t)\}$ are called the Walsh bases. Figure 2 shows the Walsh base functions in the space V_3 whose decomposition is illustrated in Figure 1 [1, 13, 14].

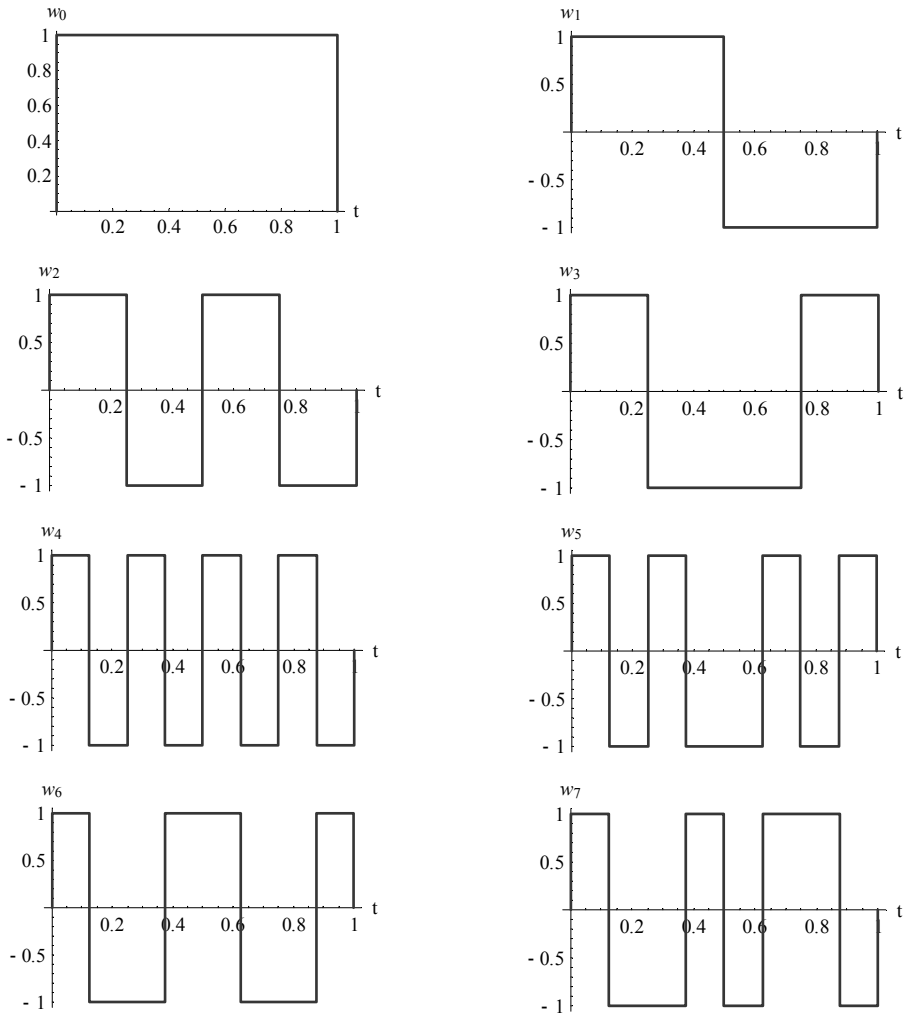


Fig. 2. The Walsh wavelet base functions

Alternatively, the space V_3 can be reproduced on the basis of different combinations of the Walsh base functions. Examples of decomposition of the space V_3 for $n = 4$ are shown in Figure 3 [1].

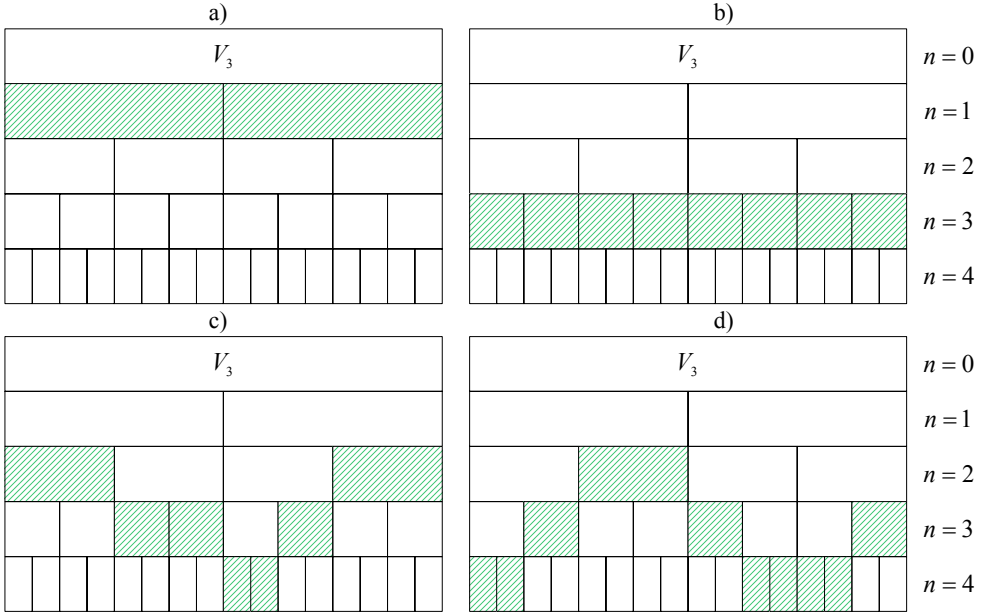


Fig. 3. Examples of decompositions of the space V_3 in base of the Walsh functions for $n = 4$

3. Procedures for estimating signal derivatives

Signal function derivatives can be determined using different algorithms, e.g. polynomial data interpolation. Wavelet packet analysis based on the Haar filter turns out to be an effective tool for determining signal function derivatives [15]. Using the low- and high-pass Haar filters one can calculate weighted sum $((a+b)/\sqrt{2})$ and weighted difference $((a-b)/\sqrt{2})$ of the consecutive pairs of numbers a and b obtained while measuring the signal function investigated. The Walsh wavelet packet analysis consists in repeated filtering of the input signal function. The Walsh wavelet packet analysis algorithm may provide the smoothed form of the input signal and its derivatives, provided that one knows the multipliers $C^p(n)$ which make it possible to scale the sequences of numbers (obtained at the successive stages of packet analysis) used for identification.

Glabisz in [3] proposed an algorithm for reproducing signal function derivatives on the basis of the first (from the left) blocks of signal expansion coefficients (Figure 4),

which is a special case of the algorithm presented here. The multiplier $C^0(n)$ on the basis of which the filtered form of the signal function is determined is written as [3]:

$$C^0(n) = \left(\frac{1}{\sqrt{2}}\right)^n. \tag{7}$$

If $p \leq n$, the multipliers $C^p(n)$ for the p -th derivative are obtained from an analysis of the sequences of the successive stages of signal function filtration. The multipliers $C^p(n)$ depend on, among other things, the filtration stage n , the Haar filter coefficients, the size N of the set representing the input signal function, the signal function sampling rate $\Delta = t/N$ and the order p of the signal function derivative sought [1, 3].

Generalizing the results reported in Glabisz's paper [3], one can reproduce the signal function derivatives from the other blocks of signal expansion coefficients at the n -th level of signal filtration. Figure 4 shows the Walsh wavelet packet analysis flow chart with digitally marked blocks which may be the basis for determining the derivatives of the signal analysed. The digit assigned to each block represents the order of the derivative reproducible from the data contained in the block. The filtered input signal form is assigned the digit 0.

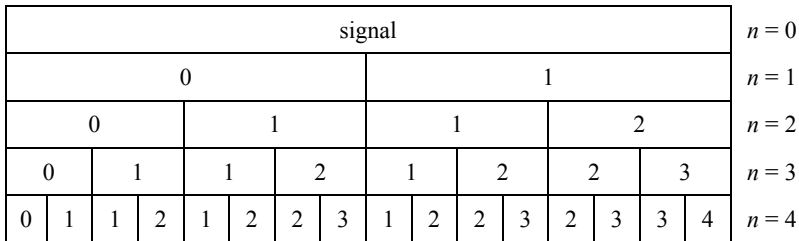


Fig. 4. Flow chart of packet analysis algorithm

The elements of the sequences of numbers (blocks) from which derivatives can be reproduced are generated by applying various (for each block) differential schemes to the input signal. It is immediately noticeable in Figure 4 that, for example, the first signal function derivative can be reproduced from the 2nd, 3rd and 5th block of coefficients at the $n = 3$ level of filtration.

The first signal function derivative ($p = 1$) can be obtained by multiplying the blocks of the n -th stage of packet analysis, which occur in positions $2^{m-1} + 1$ ($m = 1, 2, \dots, n$), by the multiplier identified by tracking the filtration sequences and given by the following relation [1]:

$$C^1(n) = (-1) \left(\frac{1}{\sqrt{2}}\right)^n 4 \cdot 2^{m-1} (2^n \Delta)^{-1}, \quad m = 1, 2, \dots, n. \tag{8}$$

The differential schemes for calculating a derivative of a specified order (p) at the chosen n -th stage of wavelet packet analysis differ significantly from each other as a result of the order in which the input signal is filtered by the low- and high-pass filters. Relation (8) formulates the multiplier for the first derivative whose place of occurrence at the n -th stage of packet analysis is defined by the number $2^{m-1} + 1$.

Similar formulas can be worked out for high-order derivatives, but they are significantly much more complex than the ones applicable exclusively to the first (counting from the left block of coefficients at the n -th stage of the analysis) derivatives of the successive orders at the n -th stage of analysis. Therefore the formulas are not presented here, but a simple algorithm for determining them was derived from their analysis.

In the flow chart shown in Figure 4, one can notice a recurrence formula which allows one to determine the order of the derivative reproducible from any block coefficients occurring at the chosen stage of wavelet packet analysis. The flow chart of a recurrence procedure which generates the information sought at the n -th stage of analysis, on the basis of the information available at the preceding stage ($n-1$), is shown in Figure 5. At the n -th stage of analysis the orders of reproducible derivatives are determined on the basis of the information block from the ($n-1$)-th stage due to a simple transformation consisting in increasing the order of the derivatives by 1 [1].

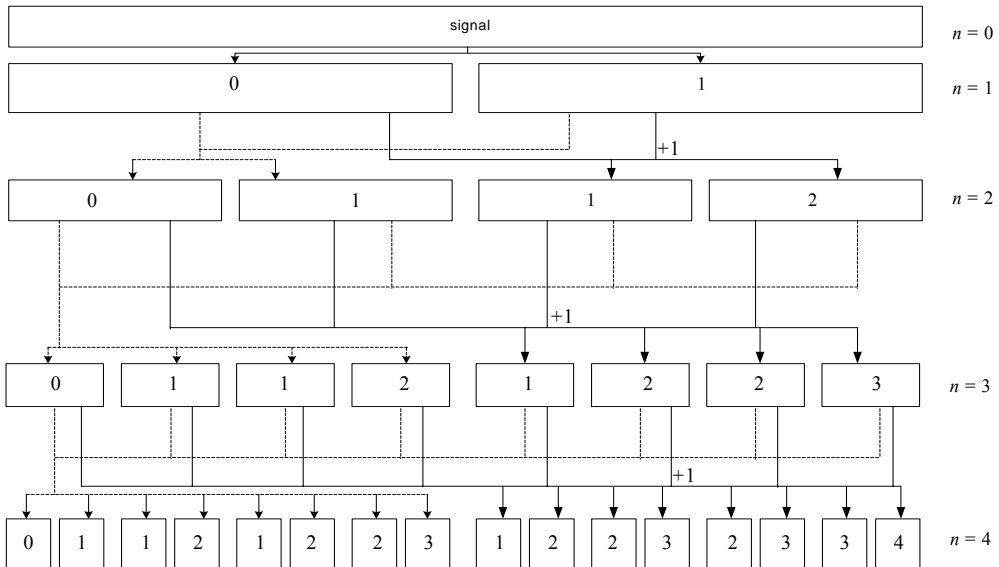


Fig. 5. Flow chart of recurrence procedure for determining reproducible derivative order on the basis of blocks from any stage of packet analysis

If one examines the formulas (not quoted here because of their complex form) for the multipliers needed for reproducing the second- and the higher-order derivatives,

one can devise a simple practical recurrence scheme for generating them. Figure 6 shows a recurrence scheme for generating multipliers at any stage of packet analysis with the Haar filter. The scheme together with the chart shown in Figure 5 allows one to reproduce a derivative of a chosen order on the basis of the block that defines its order (Figure 5) and using an appropriate multiplier (Figure 6). The recurrence schemes are applicable to a whole class of signal derivatives. One special case from this class was considered in [3].

The multipliers sought are obtained by filtering the signal function with the low-pass filter. They allow one to reproduce the input signal representation – level $n = 1$, the left block of coefficients in Figure 6. The multiplier values for reproducing the first signal function derivative (the second, from the left, block of coefficients for level $n = 1$) are calculated by multiplying the left block of coefficients at this stage of filtration by $-2/\Delta$ (Figure 6).

The next level multipliers are obtained by multiplying the first level multipliers by $1/\sqrt{2}$ and by $1/2\sqrt{2}$ (the two first, from the left, blocks of coefficients). The next second filtration level multipliers are derived by multiplying the multipliers obtained from the first two coefficient blocks by $-2/\Delta$ (the third and the fourth blocks of coefficients beginning from the left).

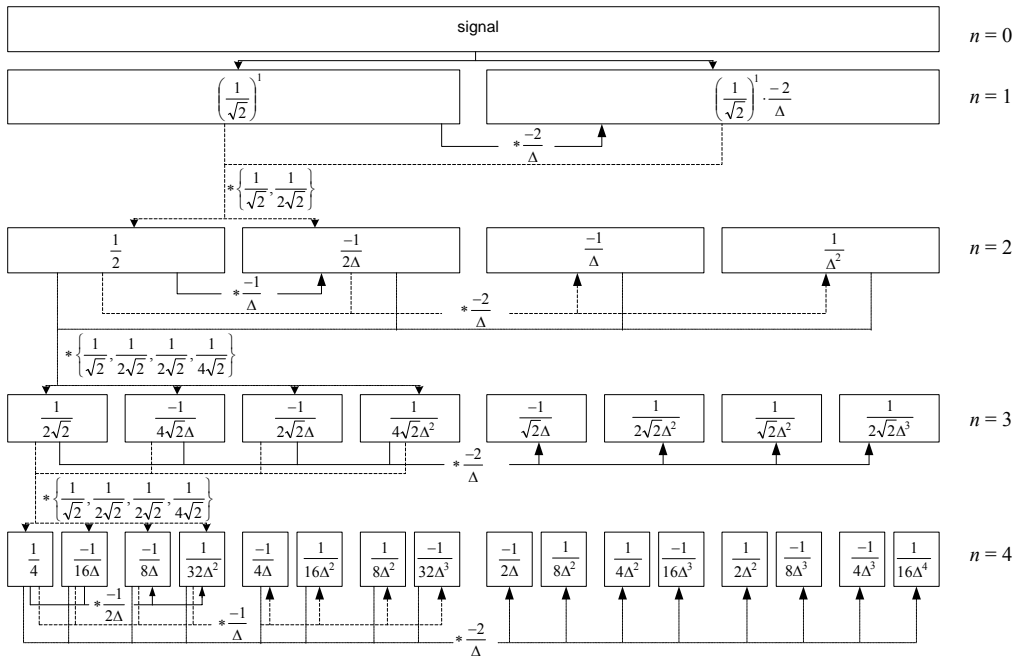


Fig. 6. Recurrence schemes for determining multipliers needed for reproducing derivatives

For example, if multipliers for the third signal derivative are to be formulated, it becomes apparent from Figure 5 that this derivative can be reproduced from the eighth block of numbers at $n = 3$ (beginning from the left) and from the 8th, 12th, 14th and 15th blocks (beginning from the left) at $n = 4$. The recurrence scheme shown in Figure 6 allows one to calculate the appropriate multipliers which in the case considered assume the values:

$-\frac{1}{2\sqrt{2}\Delta^3}$ (for the block at $n = 3$) and $-\frac{1}{32\Delta^3}$, $-\frac{1}{16\Delta^3}$, $-\frac{1}{8\Delta^3}$, $-\frac{1}{4\Delta}$ (for respectively the 8th, 12th, 14th and 15th blocks at $n = 4$).

The recurrence schemes for determining derivative orders and multiplier values can be easily verified by carrying out a Walsh-base packet analysis of the discrete representations of smooth functions whose derivatives are known.

4. Parametric identification procedure

The parametric identification procedure consists in determining the parameters of the adopted mathematical models having the form of equations or systems of linear or nonlinear differential equations. If such assumptions are accepted, the determination of the measured signal function derivatives poses a problem. The order of the derivatives depends on the order of the differential equation adopted to describe the problem.

The feasibility of the use of the Walsh-base wavelet analysis for identifying simple models of dynamical systems was tested for several cases. The analysis was carried out for linear and nonlinear systems described by the second-order equations with constant and variable coefficients and also for differential equations of the order 4. The identification was based on known sequences of numbers obtained by constant-frequency sampling of known system response $q(t)$ and known excitation $f(t)$, which are represented by the set of discrete values $q_i(t)$ and $f_i(t)$, respectively. The algorithm proposed is capable of determining higher-order derivatives. The latter were used in the identification of the parameters sought. The least squares method was employed for the identification while the minimum of the functional H was sought in the form:

$$H(a, b, c) = \sum_i \left| a\ddot{q}_i(t) + b\dot{q}_i(t) + c^n q_i(t) - f_i(t) \right|^2, \quad (9)$$

$$H(a, b, c, d, e) = \sum_i \left| a\overset{\dots}{q}_i(t) + b\overset{\dots}{q}_i(t) + c\overset{\dots}{q}_i(t) + d\overset{\cdot}{q}_i(t) + e^n q_i(t) - f_i(t) \right|^2.$$

The quantities a, b, c, d, e are the parameters sought.

In the cases tested, the effect of the different blocks of coefficients proportional to a chosen derivative (at a given packet analysis stage n) on the accuracy of the results

was investigated. The recurrence algorithms presented here were tested on, among others, the cases identical to those reported in [3] whereby the generalization presented could be evaluated.

5. Numerical examples

The algorithm proposed was tested for a case of 1-DOF system vibrations. Let us assume that a mathematical description of a linear system is sought in the form:

$$a\ddot{q}(t) + b\dot{q}(t) + cq(t) = f(t) \quad (10)$$

and for a nonlinear system as

$$a\ddot{q}(t) + b\dot{q}(t) + cq^3(t) = f(t), \quad (11)$$

where a , b and c are the parameters sought. The results of the identification of Equation (10) for $a = 2$, $b = 0.1$, $c = 5$ and Equation (11) for $a = 1$, $b = 0.1$, $c = 1$ and $f = 11\cos(t)$, depending on signal packet analysis stage n which is a source of equinumerous sets (with the size l) describing $q(t)$, $\dot{q}(t)$ and $\ddot{q}(t)$ in a discrete way, are shown in Tables 1 and 2, where the parameter values estimated and their relative errors are compared with the accurate values. The results presented in the tables were obtained for sets with the size $N = 16384$ at different system response and excitation sampling rates over the time $t \in \langle 0, 10 \rangle$.

Each table includes:

- relative errors λ_i (in per cent) for each of the parameters calculated from

$$\lambda_i = \frac{p_i - p_i^0}{p_i^0} \cdot 100\% \quad (\text{where } p_i \text{ is the identified value of the } i\text{-th parameter and } p_i^0$$

is its accurate value),

- global errors δ (in per cent) determined on the basis of the input signals q_i calculated from

$$\delta = \sqrt{\frac{\sum_{i=1}^N (q_i - \tilde{q}_i)^2}{\sum_{i=1}^N (q_i)^2}} \cdot 100\%, \quad (12)$$

where \tilde{q}_i stands for the response of a system with the parameters identified. One should note that relative errors λ_i can be determined only in test problems with

known accurate values of the parameters sought. The errors δ given by relation (12) can be the basis for evaluating the results of the identification procedure for systems whose parameters are not known beforehand. The analysis was carried out for different successive (beginning from the left) packet transformation blocks being the source for the reproduction of the first derivative. The analysis whose results are given in Tables 1 and 2 was performed assuming that the second derivative is reproduced from the first (from the left) block of the n -th stage of analysis, whose elements are proportional to the second derivative.

According to the tables, when the different data blocks (beginning from the left) are used to reproduce the first derivative at the specified n -th level of packet analysis, the error δ has a comparable value [1]. If the errors for the next levels n of wavelet packet analysis are compared, one can notice that the error gradually increases as a result of the segmentally constant approximation of the system response and its derivatives over ever longer time intervals. At higher packet analysis levels the signal function and its derivatives are reproduced from sequences of fewer numbers whereby the identification procedure runs faster, but the solution error increases. If one examines the results obtained (Tables 1 and 2), it will become apparent that the model parameters can be determined with a relative error below 1% based on such a small number as $4 \times 8 = 32$, 24 of which are signal packet expansion coefficients and the other 8 are excitation measurement results. The percentage error of the coefficients determined will be below 0.1% if 128 numbers are used for the identification. The size of the error is not affected by the choice of the block from which the first signal derivative is determined.

The 1-DOF system described by Equations (10) and (11) was also tested for randomly disturbed system response signal functions. The possible random disturbances in the signal function measured $q(t)$ were generated using the uniform distribution and drawing numbers from a range of $\pm 3\%$, $\pm 5\%$ and $\pm 10\%$ of amplitude values q_i , which were then added to q_i . The results of identifying the parameters of models (10) and (11) at random disturbances of signal q_i of $\pm 5\%$ and at undisturbed excitation $f(t)$ for different second derivative reproduction sets are shown in Tables 3 and 4, respectively. The results of the tests are extensively reported in [1].

A comparison of the examples of results shows that the Walsh packet analysis filtration is sufficient for identifying model parameters. In this case $l = 16$ and $l = 32$ respectively for the linear and nonlinear models. In contrast to the results of the analyses of the systems without random disturbances, the global solution error δ depends on the data block which is the basis for the reproduction of derivatives. It appears that at lower levels of wavelet packet analysis this error is smaller if the first blocks on the basis of which the highest derivative in the equation can be determined are used in the analysis [1].

Table 1. Results of identification of linear 1-DOF system (10) at $N = 16384$ for different first derivative reproduction sets

Level n wavelet packet analysis	Elements l	Sets of reproduction 1-st derivative	Identified parameters (exact values: $a = 2$, $b = 0.1$, $c = 5$)						Error δ %
			a		b		c		
			Estimation	Error λ_a %	Estimation	Error λ_b %	Estimation	Error λ_c %	
5	512	1	1.9999	-0.005	0.1001	0.1	5.0000	0.0	0.0164831
		2	1.9999	-0.005	0.1001	0.1	5.0000	0.0	0.0164831
		3	1.9999	-0.005	0.1001	0.1	5.0000	0.0	0.0164831
		4	1.9999	-0.005	0.1001	0.1	5.0000	0.0	0.0164831
7	128	1	1.9993	-0.035	0.1001	0.1	5.0005	0.01	0.136325
		2	1.9993	-0.035	0.1001	0.1	5.0005	0.01	0.136325
		3	1.9993	-0.035	0.1001	0.1	5.0005	0.01	0.136325
		4	1.9993	-0.035	0.1001	0.1	5.0005	0.01	0.136325
9	32	1	1.9902	-0.49	0.1003	0.3	5.0076	0.152	1.95268
		2	1.9902	-0.49	0.1006	0.6	5.0076	0.152	1.94954
		3	1.9902	-0.49	0.1007	0.7	5.0076	0.152	1.9486
		4	1.9902	-0.49	0.1007	0.7	5.0076	0.152	1.9486
11	8	1	1.8417	-7.915	0.1042	4.2	5.1245	2.49	30.0391
		2	1.8420	-7.9	0.1096	9.6	5.125	2.5	29.8719
		3	1.8421	-7.895	0.111	11.0	5.1251	2.502	29.8258
		4	1.8421	-7.895	0.111	11.0	5.1251	2.502	29.8258

Table 2. Results of identification of nonlinear 1-DOF system (11) at $N = 16384$ for different first derivative reproduction sets

Level n wavelet packet analysis	Elements l	Sets of reproduction 1-st derivative	Identified parameters (exact values: $a = 1, b = 0.1, c = 1$)						Error δ %
			a		b		c		
			Estimation	Error λ_a %	Estimation	Error λ_b %	Estimation	Error λ_c %	
5	512	1	0.9999	-0.01	0.1001	0.1	1.0002	0.02	0.0766528
		2	0.9999	-0.01	0.1001	0.1	1.0002	0.02	0.0766528
		3	0.9999	-0.01	0.1001	0.1	1.0002	0.02	0.0766528
		4	0.9999	-0.01	0.1001	0.1	1.0002	0.02	0.0766528
7	128	1	0.9997	-0.03	0.1004	0.4	1.0037	0.37	0.699945
		2	0.9997	-0.03	0.1005	0.5	1.0037	0.37	0.698557
		3	0.9997	-0.03	0.1005	0.5	1.0037	0.37	0.698557
		4	0.9997	-0.03	0.1005	0.5	1.0037	0.37	0.698557
9	32	1	0.9956	-0.44	0.1046	4.6	1.0598	5.98	9.80947
		2	0.9956	-0.44	0.1061	6.1	1.0598	5.98	9.73271
		3	0.9956	-0.44	0.1064	6.4	1.0597	5.97	9.70763
		4	0.9956	-0.44	0.1065	6.5	1.0597	5.97	9.70177
11	8	1	0.6388	-36.12	0.4083	308.3	1.8112	81.12	53.7946
		2	0.6583	-34.17	0.5478	447.8	1.8197	81.97	53.9383
		3	0.6543	-34.57	0.5676	467.6	1.8229	82.29	54.2641
		4	0.6537	-34.63	0.5726	472.6	1.8225	82.25	54.3316

Table 3. Results of identification of 1-DOF linear system (10) at $N = 16384$ and 5% disturbance amplitude for different second derivative reproduction sets

Level n wavelet packet analysis	Elements l	Sets of reproduction 2-nd derivative	Identified parameters (exact values: $a = 2, b = 0.1, c = 5$)						Error δ %
			a		b		c		
			Estimation	Error λ_a %	Estimation	Error λ_b %	Estimation	Error λ_c %	
9	32	1	1.4806	-25.97	0.0576	-42.4	4.3746	-12.508	45.9513
		2	0.9567	-52.165	0.1199	19.9	3.5665	-28.67	86.2384
		3	0.4059	-79.705	0.1066	6.6	2.288	-54.24	95.5541
		4	0.2552	-87.24	0.0849	-15.1	2.1610	-56.78	94.6817
10	16	1	1.9423	-2.885	0.1041	4.1	5.0990	1.98	14.7009
		2	1.8699	-6.505	0.0853	-14.7	4.7904	-4.192	7.3686
		3	1.7282	-13.59	0.0895	-10.5	4.8208	-3.584	29.6565
		4	1.4658	-26.71	0.1545	54.5	4.0696	-18.608	24.9122
11	8	1	1.8389	-8.055	0.1045	4.5	5.1225	2.45	30.2992
		2	1.9059	-4.705	0.0806	-19.4	5.2056	4.112	26.5837
		3	2.0577	2.885	0.1211	21.1	5.3741	7.482	16.2594
		4	1.8898	-5.51	0.0820	-18.0	5.1644	3.288	26.4069

Table 4. Results of identification of 1-DOF linear system (11) at $N = 16384$ and 5% disturbance amplitude for different second derivative reproduction sets

Level n wavelet packet analysis	Elements l	Sets of reproduction 2-nd derivative	Identified parameters (exact values: $a = 2, b = 0.1, c = 5$)						Error δ %
			a		b		c		
			Estimation	Error λ_a %	Estimation	Error λ_b %	Estimation	Error λ_c %	
9	32	1	0.9956	-0.4347	0.1046	4.6938	1.0598	5.9847	9.80947
		2	1.0024	0.2402	0.1052	5.2812	1.0605	6.0509	7.3683
		3	1.0271	2.7169	0.1081	8.1781	1.0607	6.0791	4.0758
		4	1.0040	0.4027	0.1054	5.4097	1.0606	6.0640	6.77747
10	16	1	0.9647	-3.5216	0.0864	-13.5223	1.2393	23.9322	33.4533
		2	0.9886	-1.1324	0.0586	-41.3125	1.2382	23.8261	32.8488
		3	1.0698	6.9857	-0.0678	-167881	1.2033	20.3305	54.1916
		4	0.9942	-0.5727	0.0517	-48.2203	1.2381	23.8117	32.7546
11	8	1	0.6388	-36.1168	0.4083	308.394	1.8112	81.12	53.7946
		2	0.6639	-33.6041	0.4781	378.176	1.8100	81.00	53.3256
		3	0.6184	-38.1542	0.8451	745.129	1.7301	73.01	59.6729
		4	0.6709	-32.9049	0.4854	385.472	1.8105	81.05	53.1913

The causes of the dependence of the solution error δ on the data blocks at the lower stages of packet analysis are the different sequences of low- and high-pass filters used. If a low-pass filter is used early in the systems with disturbance, this will result in the smoothing of the signal (partial filtering out of the introduced disturbance) and consequently, the effect of the ensuing high-pass filtering will have a smaller error. The computation of smooth signal derivatives yields better numerical results than those yielded by the low-pass filtering of the derivatives calculated from disturbed signals [1].

The algorithm proposed can also be applied to systems described by numerical models with slow variable parameters if segmentally constant approximation is sufficient to identify them. If the division of the signal into equinumerous sets is adopted, the approach proposed can be used to identify the parameters on the basis of each of the sets. The identification in zero initial conditions and at the observation time $t = 40$ sec was based on a sequence of $N = 32768$ excitation force and system response measurements. The results of the identification of Equation (11) for $a = 1.0 + t/10$, $a = 1$, $b = 0.1$, $c = 5.0 - t/10$ and $f = 11 \cos(t)$ are shown in Figures 7–9, where the solid line and dots represent respectively the identification result and the accurate solution.

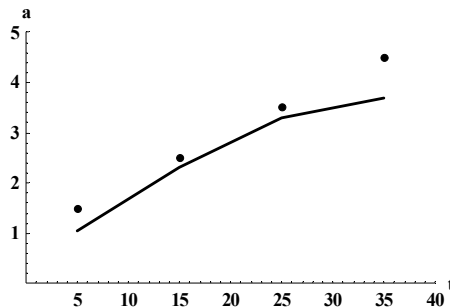


Fig. 7. Identification result for the parameter a of Equation (11) at $a = 1.0 + t/10$, $b = 0.1$ and $c = 5.0 - t/10$

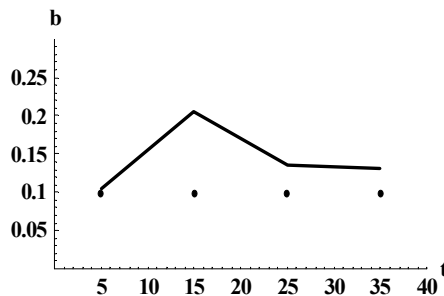


Fig. 8. Identification result for the parameter b of Equation (11) at $a = 1.0 + t/10$, $b = 0.1$ and $c = 5.0 - t/10$

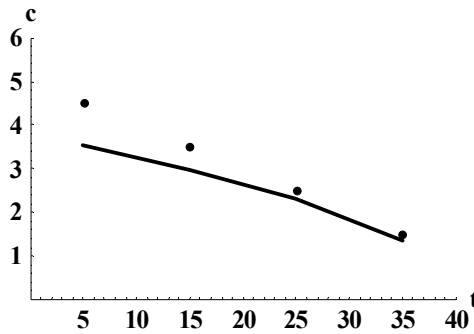


Fig. 9. Identification result for the parameter c of Equation (11) at $a = 1.0 + t/10$, $b = 0.1$ and $c = 5.0 - t/10$

The wavelet packet analysis-based algorithm capable of generating signal function derivatives was also applied to systems described by the differential equations of order 4 used as examples:

$$a \overset{\dots}{q}(t) + b \overset{\dots}{q}(t) + c \overset{\dots}{q}(t) + d \overset{\dots}{q}(t) + eq(t) = f(t), \quad (13)$$

$$a \overset{\dots}{q}(t) + b \overset{\dots}{q}(t) + c \overset{\dots}{q}(t) + d \overset{\dots}{q}(t) + eq^3(t) = f(t) \quad (14)$$

for the respective linear and nonlinear problems used as examples. The identification results for the system described by Equations (13) and (14) are shown in Tables 5 and 6, respectively. The analyses were performed for a set of the size $N = 16384$. The same principle as that used for the analysis of the equations of order 2 was adopted to reproduce the other (not mentioned in the third columns of the tables) derivatives in the model. The results of the analysis used as an example for the randomly disturbed response signal function of system (13) and (14) are presented in [1]. The results for the cases with and without random disturbances fully confirm the conclusions formulated for similar problems for models with lower-level derivatives.

It is often very difficult to determine the high derivatives of the signal measured. The reproduction of higher-order derivatives is usually avoided because of the poor results of parameter identification. The Walsh base packet analysis of the signal allows one to effectively determine its high derivatives which, as shown in Tables 5 and 6, make the identification of model parameters possible. In the case of models with high-order signal derivatives, special care must be taken when selecting packet analysis stage n whose coefficients are the basis for the reproduction of the signal and its derivatives. In order to select this stage one must carry out an analysis of global solution error δ .

Table 5. Identification results for linear system (13) at $N = 16384$ for different fourth derivative reproduction sets

Level n wavelet packet analysis	Elements l	Sets of reproduction 4-th derivative	Identified parameters (exact values: $a = 30, b = 8, c = 15, d = 6, e = 2$)										Error δ %
			a		b		c		d		e		
			Estima- tion	Error λ_a %	Estima- tion	Error λ_b %	Estima- tion	Error λ_c %	Estima- tion	Error λ_d %	Estima- tion	Error λ_e %	
9	32	1	28.7604	-4.132	8.5151	6.4387	13.1979	-12.014	6.4462	7.4366	1.4703	-26.485	2.9918
		2	28.9385	-3.538	8.4413	5.5162	13.442	-10.386	6.3903	6.505	1.5375	-23.125	2.5812
		3	29.6841	-1.053	8.1437	1.7962	14.4442	-3.7053	6.1722	2.87	1.8099	-9.505	0.9479
		4	30.4346	1.448	8.0426	0.5325	15.6234	4.156	5.9201	-1.3316	2.2398	11.99	1.5733
10	16	1	30.2587	0.8623	7.8769	-1.5387	15.2979	1.986	5.8915	-1.8083	2.0784	3.92	0.2583
		2	30.286	0.9533	7.8741	-1.5737	15.3242	2.1613	5.8926	-1.79	2.0843	4.215	0.3017
		3	30.5091	1.697	7.8322	-2.0975	15.5538	3.692	5.8849	-1.9183	2.1376	6.88	0.8003
		4	29.996	-0.0133	8.3862	-7.6725	14.3355	-4.43	6.4653	7.755	1.7408	-12.96	1.6497
11	8	1	30.6317	2.1056	8.1040	1.3	15.2567	1.7113	6.1269	2.115	2.0468	2.34	1.3354
		2	30.6612	2.204	8.1024	1.28	15.2783	1.8553	6.1264	2.1066	2.0514	2.57	1.3924
		3	30.7142	2.3806	8.1175	1.4687	15.2669	1.7793	6.1409	2.3483	2.0409	2.045	1.5561
		4	30.8848	2.9493	8.2042	2.5525	15.1911	1.274	6.2198	3.6633	1.9956	-0.22	2.2430

Table 6. Identification results for nonlinear system (14) at $N = 16384$ for different fourth derivative reproduction sets

Level n wavelet packet analysis	Elements l	Sets of reproduction 4-th derivative	Identified parameters (exact values: $a = 30, b = 8, c = 15, d = 6, e = 2$)										Error δ %
			a		b		c		d		e		
			Estima- tion	Error λ_a %	Estima- tion	Error λ_b %	Estima- tion	Error λ_c %	Estima- tion	Error λ_d %	Estima- tion	Error λ_e %	
8	64	1	27.2284	-9.23867	9.4888	18.61	12.3	-18.0	6.3675	6.125	1.8813	-5.935	10.934
		2	27.4582	-8.47267	9.3955	17.4438	12.5076	-16.616	6.3508	5.8466	1.892	-5.4	9.8301
		3	28.412	-8.62667	8.9711	12.1387	13.429	-10.4733	6.2434	4.0566	1.9383	-3.085	5.3816
		4	29.2912	-2.36267	7.8263	-2.1712	14.2936	-4.7093	5.7455	-4.2416	1.8998	-5.01	6.0861
9	32	1	30.0223	0.74333	7.2884	-8.895	15.3619	2.4126	5.5805	-6.9916	1.9930	-0.35	2.1977
		2	30.0862	0.28733	7.3182	-8.5225	15.3839	2.5593	5.6115	-6.475	1.9977	-0.115	1.8646
		3	30.2771	0.92366	7.4656	-6.68	15.4596	3.064	5.7107	-4.8216	2.0183	0.915	0.7097
		4	30.7544	2.51467	7.7231	-3.4612	15.3795	2.53	6.1363	2.2716	2.0493	2.465	0.8653
10	16	1	30.8831	2.94367	6.6443	-16.9462	15.9678	6.452	5.3957	-10.0717	2.0611	3.055	10.721
		2	30.8882	2.96067	6.6593	-16.7588	15.9463	6.3086	5.4140	-9.7666	2.0600	3.0	3.1259
		3	30.8906	2.96867	6.7938	-15.0775	15.8135	5.4233	5.5229	-7.5229	2.0567	2.835	3.0935
		4	30.7817	2.60567	6.9660	-12.925	15.4788	3.192	5.6581	-5.6983	2.0375	1.875	4.1067
11	8	1	35.0627	16.8757	-0.6871	-108.589	22.2087	48.058	1.5182	-74.6967	2.3337	16.685	15.712
		2	35.1115	17.0383	-0.7234	-109.043	22.2409	48.2727	1.5122	-74.7967	2.3336	16.68	15.781
		3	35.2758	17.586	-0.8624	-110.78	22.3467	48.978	1.4892	-75.12	2.3321	16.605	16.106
		4	35.9158	19.7193	-1.4263	-117.829	22.7543	51.6953	1.3848	-76.92	2.3227	16.135	17.641

6. Concluding remarks

Wavelet packet analysis was used for the parametric identification of discrete dynamical systems. An algorithm based on wavelet packet analysis, capable of generating signal derivatives, was developed. The algorithm allows one to reproduce signal derivatives on the basis of blocks of input signal expansion coefficients, obtained from a wavelet analysis with the Haar filter. The algorithm, using the least squares method, was tested on linear and nonlinear systems used as examples and described by the second-order equations with constant and variable coefficients and on differential equations of order 4 used as examples. Undisturbed and randomly disturbed system response signal functions were the basis for the analyses.

From the original algorithms presented – based on the Haar filter wavelet packet analysis – for identifying the parameters of dynamical systems one can conclude that:

- the Walsh wavelet packet analysis of dynamical system responses provides the basis for the efficient generation of the responses' derivatives which combined with the least squares method allow one to build an effective algorithm for identifying the parameters of linear and nonlinear mathematical models of the systems;
- the blocks of each of the Walsh wavelet packet analysis stages can be the basis for the effective reproduction of the filtered form of the signal function and its derivatives; the place of their occurrence in the packet analysis diagram and the coefficients required for reproduction are given by simple recurrence schemes;
- the appropriate – for the order of the differential equation of the mathematical model adopted – stage of packet analysis can provide the basis for reproducing derivatives from different blocks of wavelet expansion coefficients, which in the case of undisturbed signal functions are equivalent, while in the case of disturbed signal functions, the best results are obtained when the first blocks are used;
- the wavelet packet analysis level adopted when reproducing the signal function and its derivatives is a compromise between the size of the sets and the signal filtration stage, which is particularly important when the analysis is based on the functions of randomly disturbed signals;
- global solution error values can determine the choice of the stage of packet analysis whose result is to be used in the identification procedure and they provide a vital clue about how the suitability of mathematical models in nonlinear problems should be evaluated.

References

- [1] Napiórkowska-Alykow M.: *Analiza falkowa w parametrycznej identyfikacji dyskretnych układów dynamicznych*, PhD thesis, raport Instytutu Inżynierii Lądowej Politechniki Wrocławskiej, seria PRE nr 4/2004.

- [2] Worden K.: *Data processing and experimental design for restoring force surface method*. Part I: *Integration and differentiation of measured time data*, Mechanical Systems and Signal Processing, 1990, Vol. 4, No. 4, pp. 295–319.
- [3] Glabisz W.: *Identification of linear and non-linear systems with Walsh wavelets packets*, Archives of Civil and Mechanical Engineering, 2001, Vol. 1, No. 1, pp. 47–62.
- [4] Beylkin G.: *On wavelet based algorithms for solving differential equations*, [in:] J.J. Benedetto et al. (Eds.), *Wavelets: mathematics and applications*, CRC Press, 1993, Boca Raton, FL, pp. 449–466.
- [5] Bleistein N.: *Mathematical Methods for Wave Phenomena*, Elsevier Science and Technology, 1984.
- [6] Jensen A., Jensen A., la Cour-Harbo A.: *Ripples in mathematics: the discrete wavelet transform*, Springer-Verlag, New York, 2001.
- [7] Chen C.F., Hsiao C.H.: *Haar wavelet method for solving lumped and distributed-parameter systems*, IEE Proceeding Control Theory Applied, 1997, Vol. 144, No. 1, pp. 87–94.
- [8] Aboufadel E., Shlicker S.: *Discovering Wavelets*, A Wiley-Interscience Publication, 1999.
- [9] Chui Ch. K.: *An introduction to wavelets*, Academic Press, San Diego, California, 1992.
- [10] Ueda M., Lodha S.: *Wavelets: an elementary introduction and examples*, Computer Engineering and Information Sciences, Santa Cruz, USA, 1995.
- [11] Pitter S., Schneid J., Ueberhuber Ch.W.: *Wavelet Literature Survey*, Technical University, Vienna, 1993.
- [12] Daubechies I., Gilbert A.: *Harmonic analysis, wavelets and application*, lecture 1–8, 1997.
- [13] Glabisz W.: *State analysis of time-varying linear systems via Walsh-wavelet packets*, Archives of Civil and Mechanical Engineering, 2003, Vol. 3, No. 1, pp. 59–75.
- [14] Glabisz W.: *The use of Walsh-wavelet packets in linear boundary value problems*, Computers and Structures, 2004, No. 82, pp. 131–141.
- [15] Ljung L.: *System identification: theory for the user*, Prentice Hall PTR, New Jersey, 1987.

Falkowa analiza pakietowa Walsha w wyznaczaniu pochodnych sygnału

W zagadnieniach identyfikacji parametrycznej bardzo ważne jest wyznaczanie pochodnych sygnału. Wyznaczenie pochodnych jest szczególnie trudne wtedy, gdy w wyniku przeprowadzonych pomiarów dysponujemy często losowo zaburzonym i obciążonym błędem pomiarem, którym może być na przykład przemieszczenie punktu konstrukcji, a przyjęty model matematyczny ma postać równania różniczkowego z wysokimi pochodnymi mierzonej wielkości. Celem niniejszego artykułu jest wykazanie skuteczności pakietowej analizy falkowej w poszukiwaniu dobrych reprezentacji pochodnych analizowanego sygnału. Podstawą pakietowej analizy falkowej są funkcje Walsha oparte na filtrze Haara. Zaproponowany algorytm, który opiera się na pakietowej analizie falkowej, pozwala wygenerować pochodne wyższych rzędów. Pochodne te następnie wykorzystuje się w procesie identyfikacji parametrów modeli matematycznych opisujących zadany układ. Do identyfikacji zastosowano procedurę najmniejszych kwadratów i wykorzystano ją do analizy wybranych modeli liniowych i nieliniowych, w których występują pochodne do czwartego rzędu włącznie. Zaproponowany algorytm, poparty

przedstawionymi analizami, potwierdza skuteczność i efektywność pakietowej analizy falkowej w identyfikacji parametrów dyskretnych liniowych i nieliniowych układów dynamicznych.

Material tests of a bridge from 1796 over the Strzegomka River in Łaźany, Lower Silesia

Ł. Konat, G. Pękalski, J. Rabięga, U. Sachadel

Wrocław University of Technology, Wybrzeże Wyspiańskiego 25, 50-370 Wrocław

In 1928, Paul Katz (an employee of the Technische Hochschule Breslau) at the end of his paper “Die älteste eiserne Straßenbrücke des Europäischen Kontinents” [1] wrote: “If we have managed to provoke an interest of the mentioned institutions (Technische Hochschule Breslau, German Museum of Technology in München, authorities of the city of Breslau) in preservation of the bridge in Laasan (Łaźany), then our task has been fulfilled”. Publication [1] and much later papers [2–6], along with the present paper, stipulate similarly. Metallographic and strength tests made have shown that for construction of the bridge in Łaźany unique material, structure and architectonic solutions had been applied. The parts of the bridge structure have been made of grey pearlitic cast iron fulfilling all present-day requirements. There are still scarce preserved original parts of the bridge, whose documentation is available. Possibly, this is the last chance to rebuild the object, for example, in the settings of a Wrocław park, thus maintaining it for posterity.

Keywords: *bridge, cast iron, corrosion, structure, mechanical properties*

1. Introduction and short history of the bridge erection

Our study deals with the fragments of the arch bridge raised from the Strzegomka River bed in Łaźany (Laasan) near Strzegom in 1995. According to data from [4], the structure of the bridge was cast in ferrous alloy in the “Malapanew” steel mill in Ozimek, near Opole, in 1794. Initially, it was a stone bridge. News on building “iron” bridges in England and North America affected the decision of the founder of the object, Nicolas August W. von Burghauss (Count of Laasan and Peterwitz), to change the building material to more modern one, i.e. the cast iron. The count was simply in the vanguard of technological advance at the end of the eighteenth century. Hitherto, the commonly used materials were wood and stone and technical solutions of bridges made of these materials were based on experiences from past era. The use of cast iron was the novelty because the lack of experience and understanding of material properties forced designers to work intuitively, which frequently led to excessive use of material. Count Burghauss acted in strict co-operation with his friend, Prince von Reden, who recommended modernisation of furnaces and foundry equipment in the Malapane steel mill in Ozimek. The English engineer Wiliamson [3] managed to do that in 1789. After the modernisation the Malapane steel mill was not inferior to steel mills in England or Wales. That was confirmed by orders for making castings for bridges in Berlin (Kupferdamm – 1798), in Potsdam (Kavalierbrücke – 1801), in Park von Charlotten-

burg – 1803, and in Park von Paretz – 1804. In such circumstances, the bridge in Łaźany was erected. By making several small models and subjecting them to tests, a construction of the first trial archs began in August 1794, and in December that year, erection of the bridge itself. Transportation of arch parts of 8 m length and 2500 kg weight each as well as the remaining parts of total weight of 48000 kg was a great challenge at that time – they were transported by barges over the Odra River to Wrocław and then by wagons to Łaźany. Cast iron structure of the bridge was ready in 1795. Within 10 weeks 60 workers assembled the structure under the supervision of British engineer John Baidon, connecting the bridge parts by the simplest means such as bolts, clamps and wedges. The bridge had 12.5 m span (40 Fuss) and was 5.62 m wide (18 Fuss) (see Figures 1 and 2).

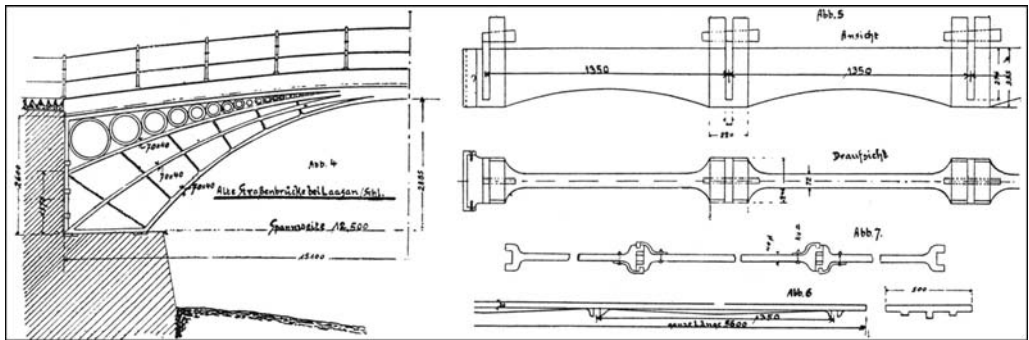


Fig. 1. Schematic diagram of the Łaźany bridge [1, 7]



Fig. 2. Illustration of the Łaźany bridge [7]

On July 30, 1796, the bridge was officially opened. It was only 15 years after the first iron bridge in the world had been built over the Severn River in Wales near Coalbrookdale (see Figure 3). The Łazany bridge was smaller, more slender and flat (see Figures 4 and 5). On that occasion Count Nicolas August W. von Burghaus commissioned striking of silver and copper commemorative medals, one of which has been preserved up to now and may be seen at the Medal Engraving Museum in Wrocław.

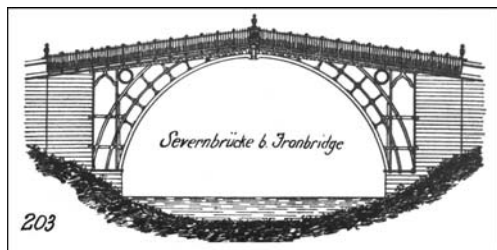


Fig. 3. First in the world, still existing iron bridge over the Severn River in Wales [7]



Fig. 4. Slender and flat structure of the Łazany bridge (compare to Figure 3) [7]

In order to evaluate the load capacity, in 1928, Paul Katz [1] derived material information from the Metallurgy and Mining Office of Prussia (Preußischen Bergwerks – und Hütten – A.G.), from the Metallurgy Office in Gliwice (Hüttenamt Gleiwitz) as well as from the Małapanew factory (Werk Malapane).

In 1995, fragments of the bridge were raised from the Strzegomka River bed. The road bridge in tests was quite accidentally damaged and later disassembled in the fifties of the twentieth century. Fragments of the bridge, which have been staying in water for almost 50 years, had been earlier in use for 149 years. The preserved part of the structure (the platform plate) has been subject to laboratory tests – some samples were taken for strength and metallographic tests.

The plate showed scarce, as for 50 years of exposure to river water, macroscopic corrosive changes. It was covered with many layers of corrosive products, solidly bounded to metallic surface. Their thickness did not exceed 5% of the plate thickness. Corrosive changes of the material were tending toward evenly distributed corrosion, and only in the vicinity of a hole in which a newel post was seated, a pitting corrosion was observed (see Figure 6).

In paper [4], it has been stated that the Strzegomka River bridge was made of grey cast iron. That indicates that in its structure there may appear: ferrite, pearlite, graphite and phosphide eutectic. Each of the above mentioned components shows different electrochemical potential (the lowest one for ferrite, the highest one for graphite). That is why between particular components of the iron the electrochemical corrosion cells could be created, which are conducive to development of the pitting and selective corrosion. The macroscopic state of the plate corrosion did not indicate that. The question

about the type and range of corrosive changes was then a prompt for getting interested in that material.



Fig. 5. Photograph of the bridge fragment taken in 1942 [7]

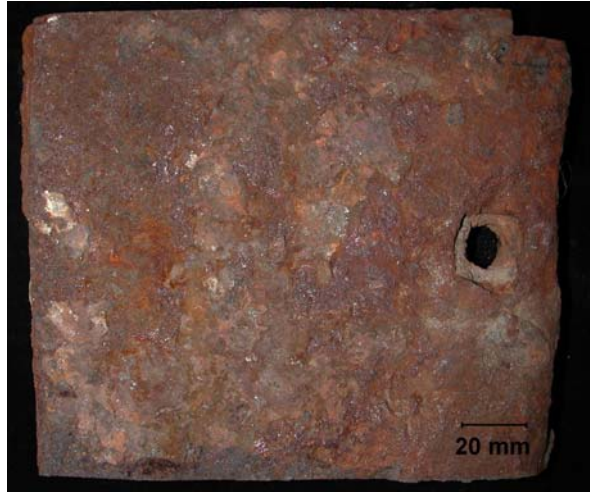


Fig. 6. Macroscopic view of the platform plate surface. Total surface is covered with multilayer corrosion products

Another reason for undertaking test works were the doubts concerning certain expressions in papers [4–6]. For example, the authors of [4] reported that the reason for lower than standard moduli for the cast iron subjected to tests (the Young modulus) could be a longer ageing time of material. According to test results of the structural aspects of materials degradation [e.g. 8 and 12] the “ageing processes” (rather structural degradation processes) in cast iron are not possible. Moreover, while an interdisciplinary scientists team, which undertakes tests on steel fragments of Wrocław bridges [12–15], has been operating at the Wrocław University of Technology for some time now, then the material of which the first iron bridge at the European continent was made of should also become the object of its interest.

From information contained in papers [4, 5] a conclusion can be drawn that fragments of the bridge under tests have been made of cast iron of pearlitic matrix. However, according to the table in the book edited by Frideric Staub [9] industrial methods of such iron production have not been developed until 1920. Earlier then in 1870–1890, the cast irons of ferritic and ferritic-pearlitic matrix with thick graphite and variable thickness graphite were produced.

Undoubtedly, the structure and the properties of such materials were very different and depended on the technology applied. However, they were characterised by repeatable properties. The paper [10] presents an example of cast iron pipes used for construction of great Versailles channel (for Versailles park fountain supply). For 330 years the pipe has been in operation and the evaluation of its present state shows “no signs” of visible corrosive changes.

Also there exists earlier data concerning application of cast iron in Europe. In paper [11], it has been said that L. Krug, the Augsburg builder, used the pipes of forged iron for distributing water in Nurnberg, in 1412. Several years later, because of corrosive destruction, they were replaced with wooden, lead and cast iron pipes. Of course, it is not known what structures the above-mentioned irons had. However, it is possible that for building the Łazany bridge the grey cast iron of pearlitic matrix was used for the first time in the world.

2. Chemical analysis and strength test results

The test results collected in Tables 1 and 2 constitute the initial data for further work. For example, they show differences in chemical analyses of the present and previous tests [4]. However, discrepancies are not large enough to indicate a change in the structure type of the cast iron tested.

Table 1. Chemical analysis results

Element contents [%]	Analysis acc. to [4]	Gravimetric analysis	X-ray microprobe	Average composition	Contents in grey cast irons
C	3.140	2.100	–	2.620	2.500–3.600
Mn	0.560	0.610	1.000	0.720	0.400–1.400
Si	2.400	1.480	1.460	1.780	0.300–3.500
P	0.260	0.570	0.390	0.410	0.100–1.000
S	0.030	0.040	–	0.035	max 0.12
Cr	–	0.100	–	–	–
Ni	–	0.050	–	–	–

Table 2. Strength and hardness test results

		Data acc. to [2]	Own tests
HB_{aver}	–	177	172
R_{caver}	MPa	501–516	567
UTS	MPa	161	167

Results for R_m and HB parameters presented in paper [4] and obtained in our own tests are very similar to each other (see Table 2). Figure 7 presents tension curves obtained in the current tests.

In publication [10] devoted to cast irons as well as in other contemporary elaborations, a series of empirical relationships is presented which enables approximate determination of other strength attributes of irons. They are based on the parameters R_m and HB and on chemical composition of irons. Using those relationships, the following values have been calculated for the material tested: compressive strength (R_c), torsional strength (R_t), shear strength (R_s) and bending strength (R_g). Based on the eutectic saturation degree (S_c), hardness of the iron has been also calculated and compared with measurement results:

$$S_c = \frac{C_c}{C_{eut}} = \frac{C_c}{4.26 - 0.31Si - 0.33P - 0.07Mn - 0.40S}$$

In order to calculate S_c , the results of gravimetric analysis from Table 1 have been adapted. The resultant eutectic saturation value S_c ranges from 0.60 to 0.93. At that value of S_c the best correlation with test results is obtained for relation [10]:

$$HB = 439 - \frac{177}{1.72 - S_c} = 144 - 249.$$

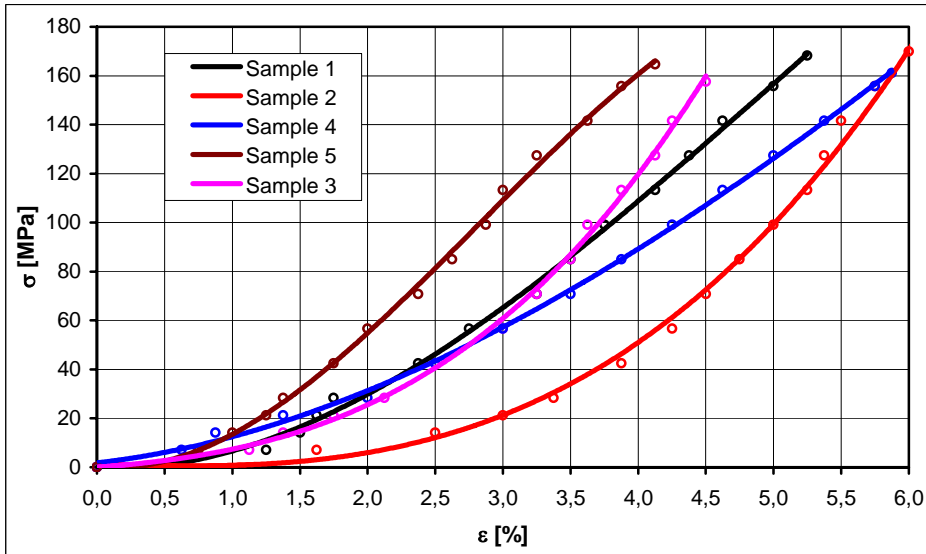


Fig. 7. Tension test curves for cast iron samples

Roughly calculated values for strength moduli for the material tested are as follows:

- | | |
|-------------------------|--|
| a) compressive strength | $R_c (\sigma_{dB}) = 567\text{--}668 \text{ MPa,}$ |
| b) torsional strength | $R_t (\sigma_{tB}) = 167\text{--}267 \text{ MPa,}$ |
| c) shear strength | $R_s (\sigma_{aB}) = 200\text{--}233 \text{ MPa,}$ |
| d) bending strength | $R_g (\sigma_{bB}) = 250\text{--}334 \text{ MPa.}$ |

Measurement and calculation results presented above coincide with the recent data concerning the methods of determining basic properties of cast irons [16]. Considering real thickness of the platform plate (50 mm) and average chemical composition of the material (disregarding the contents of sulphur, phosphorus and manganese) an approximate tensile strength and hardness have been determined. The corresponding values were: UTS , 160–170 MPa and HB , 160–170.

Standards related to grey cast irons do not allow us to determine their impact resistance (they do so for spheroid irons). Taking account of the fact that in other our papers the levels of impact resistance have been determined for steel at the temperature ranging from $-40\text{ }^{\circ}\text{C}$ to $+20\text{ }^{\circ}\text{C}$, such tests have also been made. The impact resistance of the iron tested was not changing (not decreasing) as a function of a temperature drop, and the values obtained did not exceed 5 J/cm^2 . This could be compared to the St3SX grade steel, which after 55 year use showed the impact resistance equal to 3.6 J/cm^2 at the temperature of $-40\text{ }^{\circ}\text{C}$ and steel used for construction of the Grunwaldzki bridge whose impact resistance is 10 J/cm^2 [8, 12 and 13].

Considering the chemical composition as well as obtained and calculated properties of cast iron, the material tested could be rated as grey iron of the ZL 150 grade according to PN-92/H-83100 standard (Grey Cast Iron, Classification). Currently, the material of similar properties is treated by the PN-EN 1561:2000 standard. It results from the standard that for such a material also fracture toughness is being evaluated, as it specifies the coefficient K_{ic} ($K_{ic} = 32\text{ MPa}\sqrt{\text{m}}$). Analysis of the strength data for the material indicates that the cast iron in tests fulfils all requirements imposed by the standard. For the cast iron type EN-GJL-150 the chemical composition is not being determined and therefore the chemical analysis results presented in Table 1 are compared to data from [9].

3. Microscopic test results

Figures 8 and 9 present the structure of the cast iron in the non-corroded regions. As can be seen from the microphotographs, graphite in the material subjected to tests has a form of flakes. According to the currently obligatory Standard PN-EN ISO 945 it can be defined by the IA3 standard. The structure of matrix is composed of pearlite of the lamellar shape and of pseudo-two-component phosphide eutectic. The presence of a large quantity of phosphorous eutectic testifies to rational selection of the chemical composition of the iron in the face of slenderness, frequent shape change and presence of thermal centers in the complex casting. Such a mixture that solidifies at the final stage of cast iron crystallization provides its flowing power and good filling of casting moulds. The lamellar and uniform dispersion of phase structure of pearlite testifies to slow iron cooling from the temperature of crystallization beginning to the ambient temperature. Such a status of the structure, close to the equilibrium one, provides the optimal mechanical properties and minimal level of internal stresses in the considered group of materials of such chemical composition.

Microscopic observations of corrosion samples (Figures 10–12) have shown that microscopically identified corrosive changes of the cast iron tested involve up to 10% of the plate thickness. Macroscopically, the corrosion is close to uniform in character. However, microscopically the corrosion is selective in character and appears as a result of corrosive cell activity between cathodic graphite and pearlite constituting a matrix of the iron. In surface layers (Figures 8 and 9), the iron matrix has been to-

tally dissolved in such a way that the plate material is composed of graphite precipitations and corrosion products. Somewhat deeper (Figure 12) pearlite deposits have been preserved, being distributed between the net of graphite precipitations. Edges of those areas are shredded and irregular in shape because of the selective corrosion in the area of mixture (ferrite + cementite). Ferrite is anodic in relation to cementite and therefore it submits first of all to corrosive (anodic) dissolving. Structures of the iron tested, outside the corroded zone, which have been observed in the scanning microscope are shown in Figures 13–17. Additionally, chemical microanalyses have been made with X-ray microprobe (Figures 18 and 19).

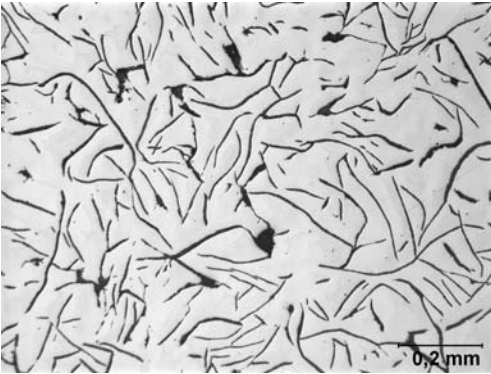


Fig. 8. Flake form of graphite in cast iron.
Non-etched microsection

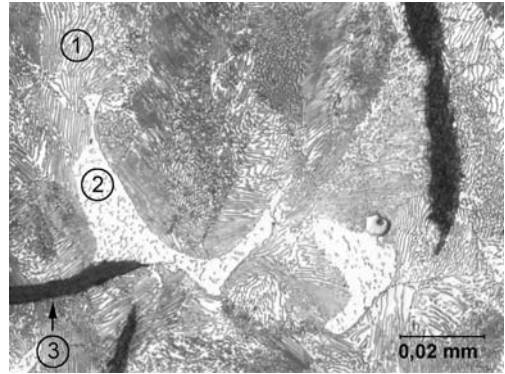


Fig. 9. Pearlitic matrix of cast iron (1) with precipitations of pseudo-two-component phosphide eutectic (2) and flake precipitations of graphite (3). Etched with 3% HNO₃

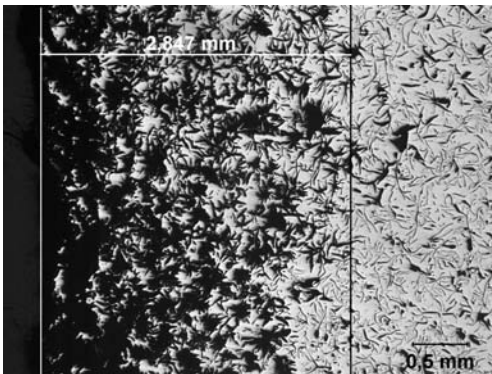


Fig. 10. Area of corrosive changes near the sample surface. Average depth of corrosive changes approaches 3 mm. Non-etched microsection

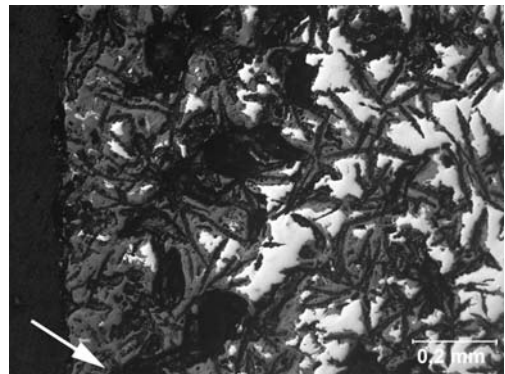


Fig. 11. Magnification of a picture shown in Figure 10. In the zone marked with arrow, only graphite in setting of corrosion products appears. Non-etched microsection

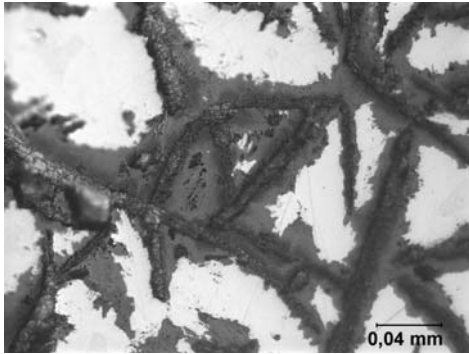


Fig. 12. Graphite with adjacent areas of partly dissolved pearlite (white fields). Non-etched microsection

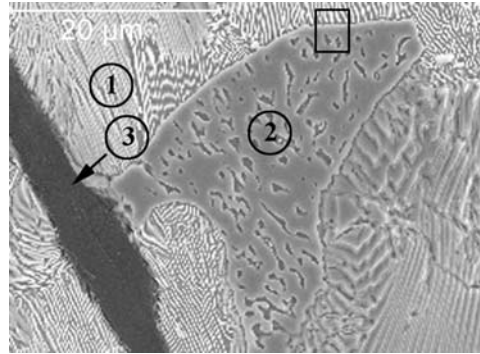


Fig. 13. Microstructure area whose superficial distribution of alloy elements has been made (Figure 14): ① – pearlitic matrix, ② – pseudo-two-component phosphide eutectic, ③ – graphite. Etched with 3% HNO₃

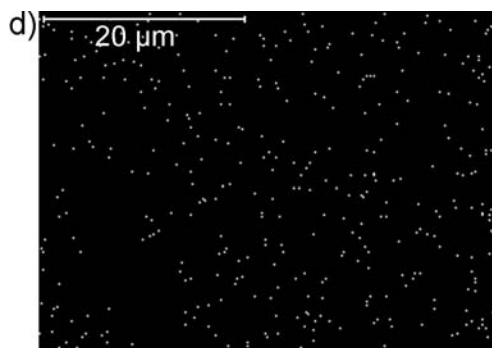
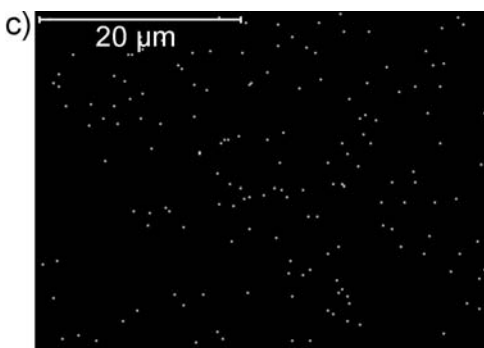
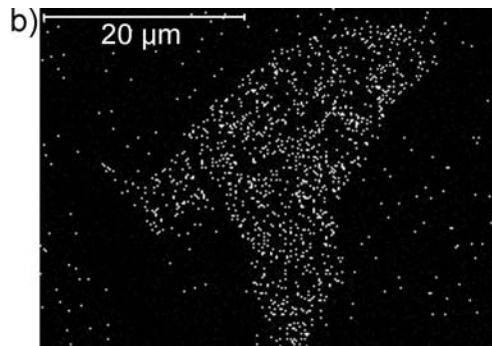
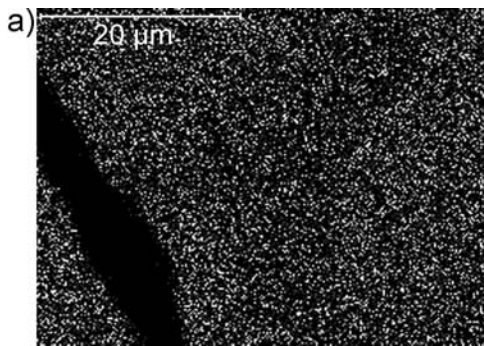


Fig. 14. Superficial distribution (mapping) of alloy elements in the cast iron tested: a) superficial distribution of iron (black area – graphite), b) superficial distribution of phosphorus (concentration of phosphorus in the phosphide eutectic area), c) superficial distribution of manganese, d) superficial distribution of silicon

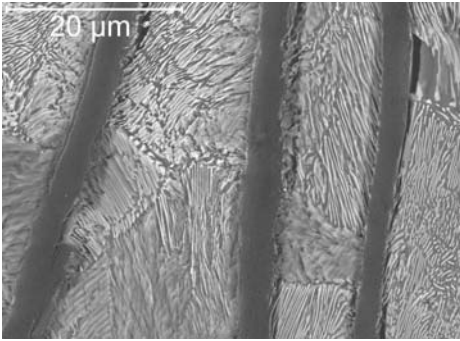


Fig. 15. Flake precipitations of graphite in pearlitic matrix. Microdiscontinuities of structure are visible at the borders of graphite-eutectoid. Etched with 3% HNO₃

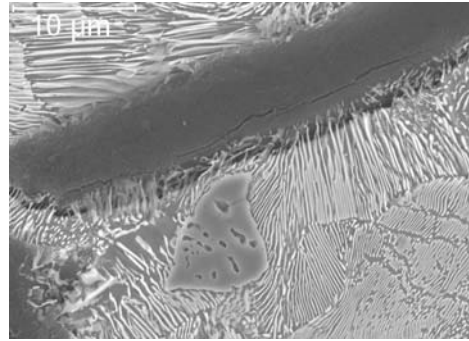


Fig. 16. Graphite precipitation with longitudinal microcrack in pearlitic matrix of a lamellar structure and precipitation of phosphide eutectic. Etched with 3% HNO₃

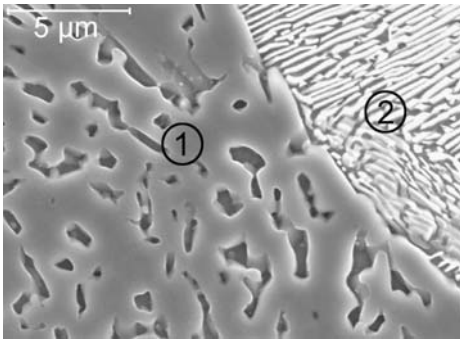


Fig. 17. Magnification of microstructure fragment marked in Figure 13 with frame: ① pseudo-two-component phosphide eutectic, ② pearlite of flake structure – the iron matrix. The area shown does not involve graphite precipitations. Etched with 3% HNO₃

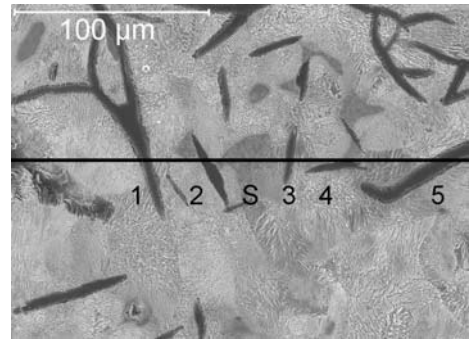


Fig. 18. Cast iron microstructure with a line along which chemical microanalysis has been conducted: 1–5 – subsequent precipitations of graphite, S – phosphide eutectic area. Etched with 3% HNO₃

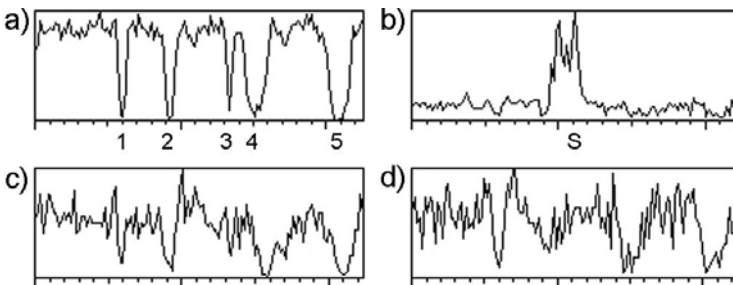


Fig. 19. Change in the content of selected elements along the line marked in Figure 18: a) iron, b) phosphorus, c) manganese, d) silicon

Observations made with scanning microscope and X-ray microprobe have introduced certain supplements compared to tests under light microscope (Figures 13–19). Presence of pseudo-two-component phosphide eutectic and pearlite of lamellar structure has been confirmed. Status of the matrix structure in the cast iron indicates its slow cooling. From here the changes in particular element content, which testify to relatively small segregation, are originating (Figure 19). The structures presented in Figures 13 and 16 and described later in this article are significant for fractures. Discontinuities can be seen at pearlite–graphite boundary, and microcracks – in the graphite itself. Along those microstructural “defects” a cracking process should run in the course of impact tests.

While summarizing the microscopic test results it could be stated that the platform plates have been made of pre-eutectic grey cast iron with pearlitic matrix, flake graphite and pseudo-two-component precipitations of phosphide eutectic. Graphite precipitations have not differed significantly in size and thickness. No part of the material samples tested has shown the presence of free ferrite grains.

4. Fractographic test results

In order to obtain fractures, the samples for impact tests with “U” notch have been used. They have been fractured with the Charpy hammer. Macroscopic structure of the fractures (Figure 20) has shown diversification neither within the group of samples, nor as a function of a temperature change.

All fractures were brittle in character (cast iron – low level of impact resistance). They mainly ran in the transcrystalline way, and only locally as intercrystalline. The presence of the intercrystalline fracture can be distinguished there by cracking zones, e.g. along the boundaries of phosphide eutectic precipitation (area 1 – Figure 21) and sometimes of graphite (Figures 22–26).

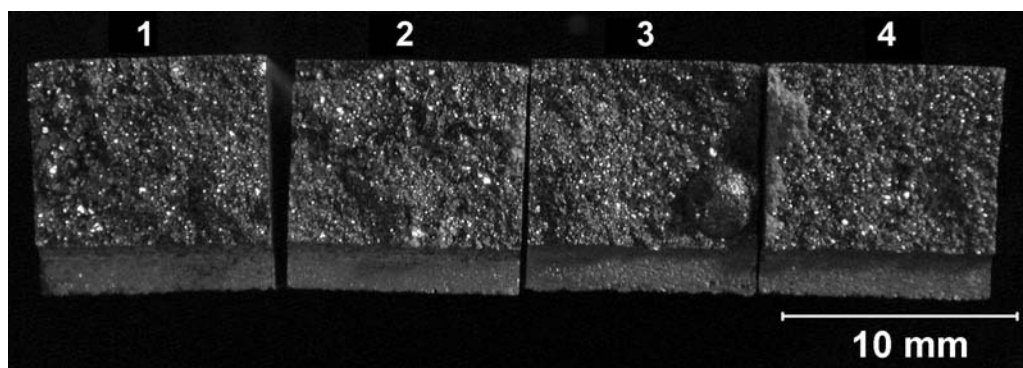


Fig. 20. Macroscopic view of fractures in impact samples: 1 – test temperature +20 °C, 2 – test temperature 0 °C, 3 – test temperature –20 °C, 4 – test temperature –40 °C

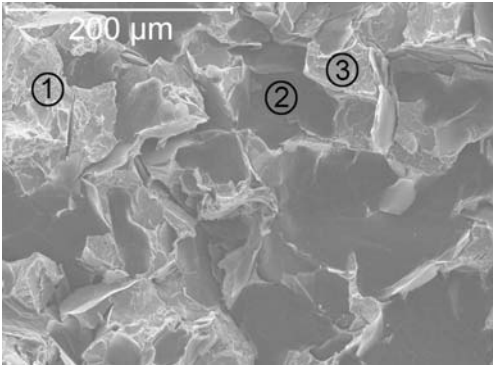


Fig. 21. Fracture of sample 4 (Figure 20):
① fracture area in contact with phosphide eutectic,
② graphite, ③ fracture area in metallic matrix

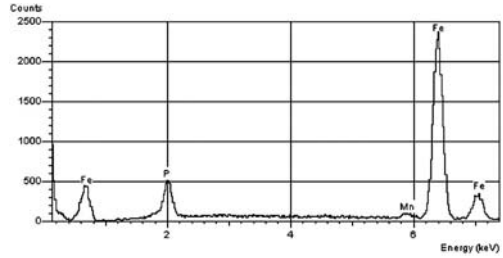


Fig. 22. Energy spectrum of X-ray radiation from area ① shown in Figure 21. High peak from phosphorus can be seen – a place after phosphide eutectic

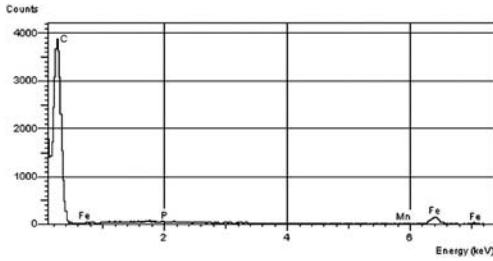


Fig. 23. Energy spectrum of X-ray radiation from area ② shown in Figure 21. High peak from graphite can be seen

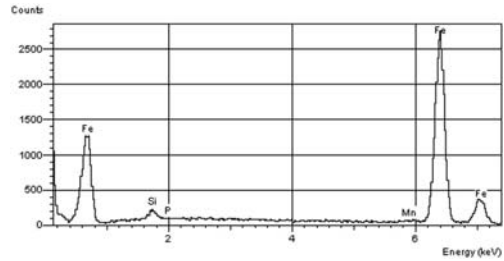


Fig. 24. Energy spectrum of X-ray radiation from area ③ shown in Figure 21. Only peaks from elements present in the cast iron in quantities specified in Table 1 can be seen

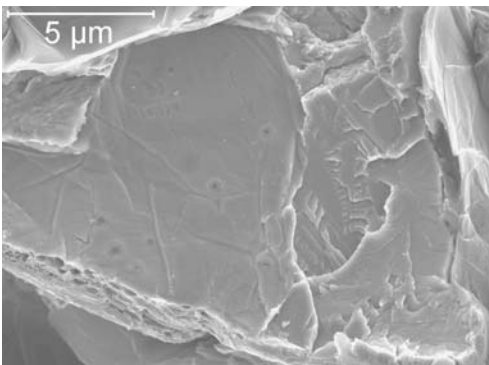


Fig. 25. Area ② (Figure 21). Transcrystalline brittle fracture

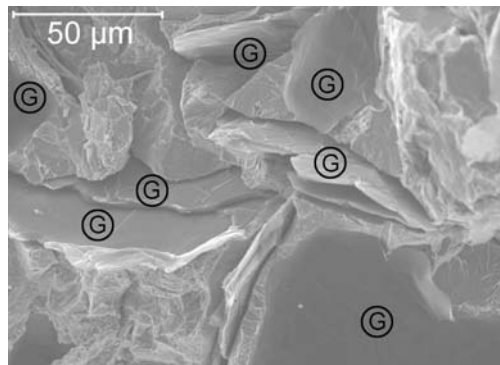


Fig. 26. Fracture area with graphite concentration (G). Intercrystalline fracture in the center

5. Summary

The material tests conducted confirm and supplement the results reported in other works [4–6]. On their basis it can be stated that the platform plates of the bridge crossing the Strzegomka River in Łazany and built in 1796 were made of pre-eutectic grey cast iron. The iron has matrix composed exclusively of lamellar pearlite, fine and homogeneous graphite and pseudo-two-component phosphide eutectic. In the areas that are not suffering from corrosion, the material fulfills the requirements of the current standard for grey cast iron of the EN-GJL-150 grade (previously the ZL 150 grade). Considering the average chemical composition and content ranges of alloy additions to those materials (Table 1) it can be concluded that it completely fulfils the presently determined requirements related to chemical composition [9].

The structure of the material in that slender and complicated in shape construction are well selected and perfectly made. The chemical composition and the structure of the material tested exclude the processes of the bridge structural degradation as a result of long-term use. They consist in precipitation of carbides and nitrides from solid solutions (ferrite), both inside grains and at their boundaries. In the cast iron tested, the solid solution (ferrite) appears only in pearlite, which constitutes the iron matrix. Structural degradation of material occurs and influences essential deterioration of its properties only in low-carbon unkilld steels (e.g. St3SX) [8, 12, 15]. Corrosive changes are also referred to as material degradation changes. The influence of corrosion on degradation of the material tested has to be considered as minimal. Corrosive changes described in the paper appeared as a result of long deposition of the plate in waters of the Strzegomka River. Such corrosive environment is many times as aggressive as atmospheric hazard in which the bridge had normally been operated.

Based on the description and interpretation of the corrosive tests we could conclude drawn that the corrosive factor (the ambient air) was negligibly small in the degradation of the Strzegomka bridge material. The theorem is more probable because, according to paper [4], the bridge platform had been made of cast iron plates on which sand bed had been placed, covered with pitcher. That way hazards resulting from the ambient air influence were not direct. A reflection also results from observation of corrosive phenomena in Versailles iron pipeline mentioned previously. At external surfaces (certainly protected against corrosion) of the pipe there may be no “visible corrosive changes”. However, most probably, the internal piping surfaces (those in contact with water) are characterized by similar corrosive changes as those shown in Figures 10–12.

Summing up the results of the tests and analyses conducted it can be stated that if there were no war damage to the Łazany bridge in 1945, and the following devastation (not degradation) of the object next year, it could still be in operation as “the first cast iron bridge on European continent”. Possibly, having restored many objects of technological culture of the past, it is worth undertaking the effort of reconstruction of the bridge from the same material and according to the same technology. However, the

initiative is not new. As early as in 1928 [1], an idea of transferring the bridge to Wrocław and setting it in the Szczytnicki Park (Scheitniger Park) emerged. The concept was raised again in [2] and local newspapers in 1942, with arguments that load capacity of the Łazany bridge was too low for that time (mining and transportation of argilla). Technical certifications issued by Technische Hochschule Breslau in 1928 allowed operating the bridge at maximum load of six tons, with safety factor 6 and “at low speed”.

Recently, Bridge Department of the Technical University of Wrocław as well as authorities of Strzegom town have undertaken actions aimed at restoring the bridge, which if existed today, would be a class “0” monument and would be specified on the UNESCO World Heritage List. Possibly, in the structures of European Union the financial barrier, which so far prevented the undertaking, could finally be lifted.

References

- [1] Katz P.: *Die älteste eiserne Straßenbrücke des europäischen Kontinents. Eine historisch-technische Studie*, TH Breslau, 1928.
- [2] Herrman W.: *Die alten schlesischen Brücken*, Dissertation TH Breslau, 1942.
- [3] Hintze E.: *Gleiwitzer Eisenkuntsguss*, Breslau, 1928.
- [4] Biliszczuk J., Rabięga J.: *Badania materiału pierwszego na kontynencie europejskim mostu żelaznego*, Inżynieria i Budownictwo, 1997, No. 6, pp. 308–309.
- [5] Biliszczuk J., Rabięga J.: *Dwieście lat mostów żelaznych na Śląsku*, Inżynieria i Budownictwo, 1996, 3, pp. 139–142.
- [6] Pasternak H., Rabięga J., Biliszczuk J.: *200 Jahre eiserne Brücken auf dem europäischen Kontinent auf Spurensuche in Schlesien und der Lausitz*, Stahlbau 65, 1996, No. 12, pp. 542–546.
- [7] Rabięga J.: Private collections.
- [8] Krajczyk A.: *Rozważania nad kryterium oceny stanu materiału konstrukcji nośnej koparek*, III Konserwatorium BDM, Conference Proceedings, Szklarska Poręba, 1997, pp. 159–168.
- [9] Staub F.: *Metaloznawstwo*, Śląskie Wydawnictwo Techniczne, Katowice, 1994.
- [10] Podrzucki G., Kaleta G.: *Metalurgia i odlewnictwo żeliwa*, Wyd. Śląskie, Katowice, 1974.
- [11] Baeckmann W., Schwenk W.: *Katodowa ochrona metali*, WNT, Warszawa, 1976.
- [12] Pękalski G.: *Materials aspects of the surface mining machinery degradation theory*, Mat. MPES, 2004.
- [13] Głuszko M., Konat Ł., Pękalski G., Rabięga J.: *Corrosion and structural degradation processes in steels used for construction of bridges*, “Corrosion 2004”, Conference Proceedings, 2004, No. 4, pp. 181–186, Lviv.
- [14] Haimann K., Konat Ł., Pękalski G., Rabięga J.: *Badania udarnośći i fraktografia przelomów jako kryteria oceny stanu degradacji stali mostowej. Badania materiałów budowlanych i konstrukcji inżynierskich*, Dolnośląskie Wydawnictwo Edukacyjne, Conference Proceedings, Wrocław, 2004.

- [15] Pękalski G.: *Degradacyjne zmiany struktury materiałów konstrukcyjnych mostów Wrocławia wybudowanych na przełomie XIX i XX wieku*, article prepared for publication.
- [16] Dobrzański L.A.: *Podstawy nauki o materiałach i metaloznawstwo*, WNT, Warszawa, 2002.

Badania materiałowe mostu na rzece Strzegomce wybudowanego w 1796 roku w Łażanach na Dolnym Śląsku

Badano fragmenty pierwszego w Europie „mostu żelaznego”, który wybudowano w 1796 roku. Most ten był już przedmiotem badań Katza (1928 rok, TH-Breslau) oraz Bliszczuka i Zabiegi (1997 rok). Po II wojnie światowej konstrukcja mostu uległa uszkodzeniu, a jej części leżały w nurcie rzeki Strzegomki przez około 50 lat.

Na tle krótkiej historii mostu i przeglądu materiałów wykorzystywanych do budowy przepraw mostowych przedstawiono rozbudowane, w porównaniu z danymi podanymi przez wymienionych autorów, wyniki badań próbek pobranych z płyt pomostu. Badania te obejmowały obserwacje makroskopowe i analizy chemiczne (grawimetryczna i spektralna), pomiary twardości, próby rozciągania i udarności, oszacowanie innych właściwości mechanicznych oraz badania metalograficzne metodami mikroskopii świetlnej i skaningowej. Na ich podstawie wykazano, że most wykonano z przedeutektycznego żeliwa szarego o osnowie perlitycznej z drobnym grafitem płatkowym i pseudodwuskładnikowej eutektyce fosforowej. W obszarach nie objętych zmianami korozyjnymi materiał ten spełnia pod względem właściwości mechanicznych, struktury i składu chemicznego wymagania, jakim musi obecnie odpowiadać żeliwo szare gatunku EN-GJL-150. Degradacja struktury materiału ogranicza się do zmian korozyjnych spowodowanych działaniem wody rzecznej na badane elementy mostu. Procesy korozyjne były zatem pomijalnie małe w rzeczywistych warunkach eksploatacyjnych mostu. Ocena wyników badań pozwala jednoznacznie stwierdzić, że gdyby nie powojenne uszkodzenia, most ten mógłby być w dalszym ciągu użytkowany. Ze względu na historyczną wartość tego obiektu już w 1942 roku proponowano jego demontaż i przeniesienie go do Parku Szczytnickiego we Wrocławiu. W konkluzji proponuje się podjęcie obecnie tej inicjatywy i wykorzystanie nielicznych już oryginalnych fragmentów mostu do jego rekonstrukcji.

Coefficients of buckling length of chords for out-of-plane instability of small-bay trusses

A. BIEGUS, D. WOJCZY SZY N

Wrocław University of Technology, Wybrzeże Wyspiańskiego 25, 50-370 Wrocław

The stability of chords in the case of out-of-plane buckling of small bay trusses has been analysed. Seven static schemes having different member stresses, topology and the way of support have been investigated. The computing model of a flat truss has been considered taking into account the virtual displacements and the spatial model of bar system as well. The comparative analysis of coefficients of buckling lengths has been made for chords in the case of out-of-plane buckling of the truss models considered.

Keywords: *one-way truss, out-of-plane buckling*

1. Introduction

Designing one-way trusses according to [1], we can assume coefficients of buckling length of chords for out-of-plane instability as $\mu_y = 1.0$. If the distance between the nodes of out-of-plane buckling mode contains few panels, this kind of estimation might be inadequately precise and in extreme cases leads to unnecessary material consumption or increases structural safety risk. This results from the model assumed in the analysis of stability of chords, according to [1], in which the single bar under constant axial compression force is isolated from the truss. This model ignores few significant conditions, i.e., real distribution of axial force, which may change itself gradually along the length of chords and also from the compression to tension, the method of connecting chords to web member, and the point of imposing the load relative to the axis of support of construction as well.

The attempt of taking all the enumerated factors into account in the out-of-plane stability analysis of chords has been made in [2]. The stability of the one-bay chords of roof trusses with web members in "N" configuration has been analysed. In the span length, the upper and lower nodes of these structures have been supported in the perpendicular direction towards truss plane by sway bracing. The analytical model of a chord as the bar isolated from the truss, which is loaded with gradually changing axial force, and the spatial model of the bar buckling (lateral buckling of truss) have been considered. The stability of chords has been analysed parametrically by changing both the number of panels $n = 2-9$ and the way of loading (in the upper and lower nodes of chords). Additionally, the effect of both, the chords to verticals' connection (fixed and hinged) and to supports connections (fixed and hinged in terms of torsion),

on the critical load have been studied as well. The consideration of the real distribution of axial force in the chord, the impact and stiffness of connection chords with bars and with support as well as the way of loading the structure allow considerably smaller values of μ_y (μ_y ranges from 0.9 to 0.4) than that proposed in [1]. However, for the small-bay trusses, in which the number of panels n is 2, $\mu_y \cong 1.10$, that is 10% more compared to [1]. The critical load for out-of-plane buckling obtained according to [1] leads to overestimation approaching 21%.

The coefficient of the buckling length of chords $\mu_y \cong 1.10$ has been obtained for the spatial model of the bar buckling (lateral buckling of truss), while for an analytical model of the bar isolated from the truss, loaded with varying axial force, $\mu_y \cong 0.94$. In the structures analysed, the bars were connected with chords in a hinged way. This paper deals with an attempt at explaining the differences in μ_y and with the identification of factors influencing the critical load of chord of small-bay trusses. As hypothetical essential factors, having the impact on critical load of chord of small-bay trusses, the influence of web members of the truss on its unsupported, indirect node and displacement of this node perpendicular to plane of structure were assumed. Moreover, it was assumed that the topology of bars and their axial stresses (compression or tension) might be essential in this case. That is why the trusses in which the topology of bars was changed, the ratio of their depth (h) to the length of panel (a) and the way of support were analysed.

The analytical solutions presented in this paper exemplify universal conception of load capacity estimation of flat trusses' chords for out-of-plane instability. It consists in the analysis of imperfect models, in which the virtual displacements of Δ_1 and Δ_2 nodes are taken into consideration.

2. The description of the problem analysed

The subject of this paper is the analysis of out-of-plane buckling of chords in small-bay trusses. The analytical model of a flat truss including the virtual lateral out-of-plane displacements and also the spatial model of the bar buckling (lateral buckling of truss) have been considered. The aim of research dealing with the model of a one-way truss was to consider in the stability analysis of chord its real distribution of axial force as well as the effect of web members. The analysis of the model of lateral buckling of the truss allowed us to consider, apart from its real axial stress and the other bars' impact, the geometrical parameters of structure, the point of imposing the load and also the way of connecting chords with the other bars as well as with the support. Moreover, it allowed us to verify the assumptions accepted in the stability analysis of the one-way model.

Seven single-span trusses K-1–K-7, whose static schemes are shown in Table 1, have been studied. The concentrated forces are applied to the upper nodes. In the span length, the upper and lower nodes are supported by sway bracing (marked: with “•” in Table 1). The bars of trusses are made of steel square tubes. Continuous chords are

hinge connected with verticals and diagonals. The trusses being analysed have different bar topology and the position of support axes for upper (K-1, K-2) and lower (K-3–K-7) nodes. Out-of-plane chord stability has been analysed parametrically by changing the truss depth h to the length of panel a ratio.

The out-of-plane critical loads of chords $N_{cr,y}$ (measured as the maximal value of their axial force) for the flat truss model have been obtained analytically, while for lateral buckling of truss model – numerically by FEM. On the basis of results the coefficients of out-of-plane buckling length of chords have been calculated from the following formula

$$\mu_y = \frac{\pi}{2a} \sqrt{\frac{EJ_y}{N_{cr,y}}}, \quad (1)$$

where: $N_{cr,y}$ – the out-of-plane critical load of chords measured as the maximal value of axial force in this member; EJ_y – the flexural stiffness in the plane of buckling of the chord.

3. The out-of-plane stability analysis of one-way truss chord in the presence of virtual displacements

The method used in out-of-plane stability analysis of chords of small-bay trusses is a modification of critical load estimation procedure of spatial buckling of two cross braces of “X” joint shown in [3]. This method is based on the energy criterion of stability.

The trusses analysed have been split into single unconnected bars: chords, diagonals and verticals. At the ends all of them were subjected to axial forces, whose values were taken from structural analysis of truss loaded in nodes with the force $P = 1$. Then a general deflection in an individual form was assumed for each bar, which satisfies all the boundary conditions, both geometric and static. Based on the displacements and taking advantage of the elementary theory of structures, the increase of energy in bending system (ΔU) was defined. Then the work of nodal force (ΔT) on the displacements in the direction of center line as the effect of buckling of bars was determined. The value of buckling load for a structure was obtained from the comparison of the increase of energy in the bending system ΔU and the work ΔT . As a result of calculations based on the energy equilibrium, buckling load of chord $N_{cr,y}$ is determined as a function of parameters of the static scheme of truss K- i . From Equation (1) the values of coefficients of buckling length of chords out-of-plane μ_y were defined.

In the one-way computational model of trusses for upper and lower chords (which are not supported in the direction being perpendicular to the principal plane of girder), the virtual lateral displacements Δ_1 and Δ_2 were adopted. The chords in the case of out-of-plane instability undergo those displacements. On their basis the functions of de-

flections of the trusses' center line of bars $x^i(z_i)$ have been assumed. In the static schemes of structures, the local axes z_{1i} have been assumed to overlap the direction of longitudinal axis of each of the members; however, the direction of the local axes x_{1i} is the same as the direction of the global axis x (Figure 1).

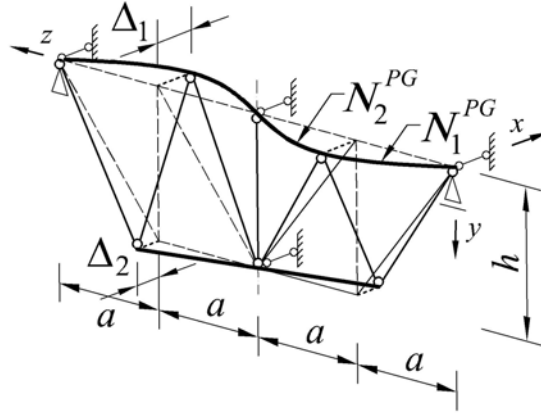


Fig. 1. The scheme of the computational model of the stability for the one-way truss K-1 in the presence of virtual displacements Δ_1 and Δ_2

For the hinged connection of the web members with the continuous chords and the designations shown in Figure 1 two types of displacements of bars have been studied: sinusoid half-wave in the following form

$$x^i(z_1) = \Delta_i \sin \frac{\pi z_1}{2a} \quad (2)$$

and linear functions.

The sinusoid describes the deformation of the upper chord for the trusses K-1 and K-2 and the deformation of the upper and lower chords for the cases K-3–K-7. The displacement of axes of the remaining bars has been assumed in the form of linear functions with the directional coefficients which are characteristic of the group of bars under examination.

The presented method of the analysis of stability of the upper chord out-of-plane buckling of small-bay trusses was discussed based on the example of K-1 truss with the static scheme of the computational model shown in Figure 1. This truss web comprises compression verticals and diagonals under tension. The axial force in the upper chord of the truss changes gradually: from $N_1^{PG} = -1.5 \text{ Pa/h}$ at the supporting zone to $N_2^{PG} = -2.0 \text{ Pa/h}$ for the median part. In this one-way structure, the virtual displacements of the upper truss node Δ_1 and the lower truss node Δ_2 were accepted in the analysis assuming the same directions but different senses. On the basis of the form of

the spatial instability accepted in this way, the functions of displacements for axial truss members were selected: for the upper chord in accordance with (2), and linear functions for the remaining members.

The increment of the bending energy ΔU in the chords of the truss analysed has been determined using the following formula

$$\begin{aligned} \Delta U = & \frac{EJ_{PG}}{2} \int_0^{2a} \left(\frac{d^2 x^{PG}(z_1)}{dz_1^2} \right)^2 dz_1 + \frac{EJ_{K_1}}{2} \int_0^{\sqrt{a^2+h^2}} \left(\frac{d^2 x_1^K(z_1)}{dz_1^2} \right)^2 dz_1 + \frac{EJ_S}{2} \int_0^h \left(\frac{d^2 x^S(z_1)}{dz_1^2} \right)^2 dz_1 \\ & + \frac{EJ_{K_2}}{2} \int_0^{\sqrt{a^2+h^2}} \left(\frac{d^2 x_2^K(z_1)}{dz_1^2} \right)^2 dz_1 + \frac{EJ_{PD}}{2} \int_0^a \left(\frac{d^2 x^{PD}(z_1)}{dz_1^2} \right)^2 dz_1, \end{aligned} \quad (3)$$

where: J_i – the out-of-plane moment of inertia (PG – for the upper chord, PD – for the lower chord, K_1 – for the diagonals, S – for the vertical member of the truss, respectively), E – Young's modulus, $x^i(z_1)$ – the assumed functions of deformations for the axes of the truss members.

Owing to the linear character of the accepted functions of the truss web and the lower chords as well, only the bending of the upper chord of trusses affects the calculated increase of the structure energy ΔU . The increment of the truss energy with the K-1 scheme is

$$\Delta U[a, EJ_{PG}, A_1] = \frac{\pi^4 EJ_{PG} A_1^2}{32a^3}. \quad (4)$$

To determine the force that is exerted on the displacements of the bar end connected with the deformations of the structure (on the basis of the structural stability analysis) the value of the internal forces in the truss chords N^i has been defined. The work of the nodal load has been calculated from

$$\begin{aligned} \Delta T = & -\frac{N_1^{PG}}{2} \int_0^a \left(\frac{dx^{PG}(z_1)}{dz_1} \right)^2 dz_1 - \frac{N_2^{PG}}{2} \int_a^{2a} \left(\frac{dx^{PG}(z_1)}{dz_1} \right)^2 dz_1 - \frac{N_1^K}{2} \int_0^{\sqrt{a^2+h^2}} \left(\frac{dx_1^K(z_1)}{dz_1} \right)^2 dz_1 \\ & - \frac{N^S}{2} \int_0^h \left(\frac{dx^S(z_1)}{dz_1} \right)^2 dz_1 - \frac{N_2^K}{2} \int_0^{\sqrt{a^2+h^2}} \left(\frac{dx_2^K(z_1)}{dz_1} \right)^2 dz_1 - \frac{N_2^{PD}}{2} \int_0^a \left(\frac{dx^{PD}(z_1)}{dz_1} \right)^2 dz_1, \end{aligned} \quad (5)$$

where $x^i(z_1)$ is the same as in Equation (3), N^i stands for the value of the axial forces in chords.

For the considered scheme of the truss K-1 we obtain

$$\Delta T[h, P, \Delta_1, \Delta_2] = \left(\frac{7\pi^2}{32} - \frac{1}{4} \right) \frac{\Delta_1^2 P}{h} + \frac{3}{4} \frac{(\Delta_1 - \Delta_2)^2 P}{h} - \frac{3}{2} \frac{\Delta_2^2 P}{h}. \quad (6)$$

The critical load of the truss K-1 due to out-of-plane instability condition of the truss chord has been determined by comparing (4) and (6)

$$P_{cr}[a, h, EJ_{PG}, k] = \frac{\pi^4 h EJ_{PG}}{[16 + 7\pi^2 + 48k - 24k^2] a^3}, \quad (7)$$

where

$$k = -\frac{\Delta_2}{\Delta_1}. \quad (8)$$

The coefficient of buckling length of the upper chord out of the plane μ_y (1) was defined on the basis of its critical force $N_{cr,y}$, under which the truss buckles (7). The calculated coefficient of buckling length of the chord is

$$\mu_y[k] = \frac{\sqrt{16 + 7\pi^2 + 48k - 24k^2}}{2\sqrt{2}\pi}. \quad (9)$$

The result obtained is the function of the variable k . The function μ_y reaches its extremum at $k = 1$, which means that the minimum value of the critical force occurs in the chord when the displacement Δ_2 is equal to Δ_1 , but has an opposite sign. In the stability analysis of the truss chord K-1, the deficiency of the displacement of the lower truss node Δ_2 ($k = 0$) is the most advantageous. The maximum critical loads of the structure P_{cr} and the corresponding coefficients of the analysed structure μ_y are shown in the form

$$\begin{aligned} k=0 & \Rightarrow P_{cr} = \frac{\pi^4 h EJ_{PG}}{[16 + 7\pi^2] a^3} \Rightarrow \mu_y = \frac{\sqrt{16 + 7\pi^2}}{2\sqrt{2}\pi} \cong 1.038, \\ k=1 & \Rightarrow P_{cr} = \frac{\pi^4 h EJ_{PG}}{[40 + 7\pi^2] a^3} \Rightarrow \mu_y = \frac{\sqrt{40 + 7\pi^2}}{2\sqrt{2}\pi} \cong 1.175. \end{aligned} \quad (10)$$

In the stability analysis of chords according to the method presented, the displacements Δ_1 and Δ_2 were hypothetically assumed to be the closest to the actual ones. The acceptance of these values, especially the ratios between them, has an essential influence on the estimation of μ_y .

Table 1. Coefficients of buckling length of chords for out-of-plane instability for the trusses μ_y

Symbol	Truss scheme	N_1^{PG} / N_2^{PG}	Buckling coefficient of the chord μ_y
1	2	3	4
K-1		$\frac{1.5P}{2P}$	$\mu_y = \frac{\sqrt{16 + 7\pi^2 + 48k - 24k^2}}{2\sqrt{2}\pi}$ $\mu_y, [k=1] \cong 1.175$
K-2		$\frac{1.5P}{1.5P}$	$\mu_y = \frac{\sqrt{8 + 3\pi^2 + 16k - 16k^2}}{\sqrt{3}\pi}$ $\mu_y, [k=0.5] \cong 1.185$
K-3		$\frac{1.5P}{2P}$	$\mu_y = \frac{1}{2\sqrt{2}\pi} \sqrt{\frac{16 + 7\pi^2 - 3k(16 + k\pi^2)}{1 + \alpha k^2}}$ $\mu_y, [k=0] \cong 1.038$
K-4		$\frac{1.5P}{1.5P}$	$\mu_y = \frac{1}{\sqrt{3}\pi} \sqrt{\frac{8 + 3\pi^2 - 2k(8 + k\pi^2)}{1 + \alpha k^2}}$ $\mu_y, [k=0] \cong 1.127$
K-5		$\frac{0}{1.5P}$	$\mu_y = \frac{1}{\sqrt{6}\pi} \sqrt{\frac{16(1-k) + (3-7k^2)\pi^2}{1 + \alpha k^2}}$ $\mu_y, [k=0] \cong 0.878$
K-6		$\frac{0}{2P}$	$\mu_y = \frac{1}{2\pi} \sqrt{\frac{8 + (2-3k^2)\pi^2}{1 + \alpha k^2}}$ $\mu_y, [k=0] \cong 0.838$
K-7		$\frac{0}{2P}$	$\mu_y = \frac{1}{2\pi} \sqrt{\frac{8 + (2-3k^2)\pi^2}{1 + \alpha k^2}}$ $\mu_y, [k=0] \cong 0.838$

The analogical procedure has been used for the trusses K-2–K-7. The values of the coefficients of out-of-plane buckling length of chords of these structures μ_y together with their most disadvantageous values are presented in the column 4 of Table 1 (in the formulas, the following assumption have been made: $\alpha = J_{PD}/J_{PG}$ – the ratio of the moment of inertia of the lower chord to the moment of inertia of the upper chord; for the trusses K-5–K-7 the parameter k is $k = \Delta_2/\Delta_1$).

4. The out-of-plane buckling analysis due to spatial instability of the truss

The flat trusses K-1–K-7 (Table 1) have been exposed to the same numerical studies as those of spatial structures. Their continuous chords are hinged to the truss web, both in the plane yz and the plane xy (Figure 1). The overall buckling of trusses has been analysed in the parametric form, changing the h/a ratio. The FEM calculations of the structures' stability were based on the SOFiSTiK system [4].

The trusses analysed undergo the overall instability in the same mode as in the case of the lateral buckling of beams. The out-of-plane buckling of the compressed chord has a direct effect on the buckling mode. The chosen results of the calculations of the coefficient of the buckling length of the chord μ_y (K-1–K-7) are presented in Table 2 (lines 1–7). For comparison purposes, in line 8 (Table 2) the coefficients μ_y obtained by using the method discussed in the point 3 are given, while the value recommended in [1] is shown in line 9 and the values of the estimation for the computational model of the isolated member [2] are shown in line 10.

Table 2. Coefficients of buckling length of chords for out-of-plane instability of the structure μ_y

No.	$\frac{h}{a}$	Coefficients of buckling length of chord μ_y						
		K-1	K-2	K-3	K-4	K-5	K-6	K-7
1	0.50	1.053	1.099	0.925	0.995	0.807	0.761	0.758
2	0.75	1.079	1.111	0.954	1.018	0.821	0.780	0.778
3	1.00	1.096	1.116	0.973	1.031	0.829	0.791	0.790
4	1.25	1.107	1.119	0.985	1.040	0.834	0.799	0.798
5	1.50	1.116	1.121	0.995	1.048	0.839	0.805	0.804
6	1.75	1.123	1.123	1.003	1.054	0.843	0.809	0.809
7	2.00	1.128	1.126	1.010	1.060	0.846	0.813	0.812
8	e.c. of s.	1.175	1.185	1.038	1.127	0.878	0.838	0.838
9	[1]	1.0						
10	[2]	0.936	1.0	0.936	1.0	0.727	0.727	0.727

5. Final remarks and conclusions

In the case of small-bay trusses (for instance: cantilever beam, space grid), ignoring the reaction of the web members of the truss in the out-of-plane stability analysis of the structure accepting $\mu_y = 1.0$ [1] can lead to the overestimation of their critical load $N_{cr,y}$. The analysis presented showed that the lateral displacement of the unsupported node causes an increase of buckling length coefficient ($\mu_y > 1.0$). In this intermediate

node of the chord, we have a virtual reaction of vertical and diagonal members, which is perpendicular to the principal plane of the truss and the axis of the chord. This causes additional stress of the compressed chord (the reduction of load-capacity) and buckling under the load being smaller than that in the case of the compressed truss member in which there is no reaction of the verticals and diagonals of the truss (models according to [1] in contrast with isolated chord according to [2]).

In the work, the structures of the perfect geometry of chords' axes hinged to the truss web were analysed. It is necessary to notice that the real constructions with initial deflections of the axis of the chords Δ_0 additionally decrease their load capacity. The reducing reaction of the verticals and diagonals has then more disadvantageous influence because it is responsible for the displacement Δ_0 (according to [5] the permissible flexure of the axis of the chord is $\Delta_0 = \max [L/500; 6 \text{ mm}]$, where L is the length of the chord). Simultaneously connections of the chords with the verticals and diagonals of the structures are not perfectly hinged and they have a certain rigidity that increases the critical out-of-plane load capacity of the chords analysed.

Coefficients of the buckling length of the chords studied $\mu_y > 1.0$ were found in the trusses K-1–K-4. The maximum values μ_y occur in the structures K-2 and K-4 (where the chord is compressed by the constant force along its length, $N_1^{PG}/N_2^{PG} = 1.0$) as well as in K-1. If the energy method is used, the obtained values of μ_y are higher than those given in [1] by 18.5% (for K-2) and 12.7% (for K-4). The difference in estimation of the critical load of the chord $N_{cr,y}$ in comparison to [1] is about 29% for K-2 and about 21% for K-4. In the structures K-1 and K-3, the ratio of the forces in the chord is $N_1^{PG}/N_2^{PG} = 1.5/2.0$. For such loading of the chord $\mu_y \cong 0.94$ [2] when the reaction of the verticals and diagonals is neglected; on the contrary, when the reaction is considered (point 3) $\mu_y \cong 1.175$ (for K-1) and $\mu_y \cong 1.038$ (for K-3). In comparison to the load capacity of the chord $N_{cr,y}$, according to [1] the difference approaches 28% (for K-1) and 7% (for K-3).

For trusses K-5–K-7, using the energy method, $\mu_y \cong 0.88$ (K-5) and $\mu_y \cong 0.84$ (K-6 and K-7) were obtained. In this case, the values $\mu_y < 1.0$ are affected by the force distribution in the compressed chords (zero-force N_1^{PG} at the supporting zone of the chord) and truss web as well as by topology of the verticals and diagonals. If only the actual distribution of the longitudinal force in the chord is considered, then $\mu_y \cong 0.73$ [2]. Owing to the reaction of the verticals and diagonals (according to the estimation in point 3) the increase of the value μ_y of about 21% (for K-5) and about 15% (for K-6 and K-7) in comparison with $\mu_y \cong 0.73$ was observed [2].

The stability analysis of the trusses using FEM allows more accurate defining the critical load for a chord than the estimation applied in point 3. Moreover, it allows considering among others: the characteristics of the truss nodes (fixed, hinged, flexible), the way of loading (in the upper or lower chord), the support (fixed and hinged in terms of torsion) as well as the characteristics of the geometry of the structure (h/a ratio). The values of μ_y obtained by means of FEM confirm the disadvantageous effects

of verticals and diagonals on the chords' resistance in the case of out-of-plane buckling. The differences in μ_y in comparison to that obtained in [1] range from 5 to 13% (for K-1), from 10 to 13% (for K-2) and to 6% (for K-4). Whereas, μ_y for K-5–K-7 is more advantageous than that proposed in [1]. It has to be mentioned that FEM allows us to observe the effect of the system geometry h/a on the quantity μ_y , which is ignored in the energy method.

References

- [1] PN-90/B-03200. *The Steel Structures. Design rules.*
- [2] Biegus A., Wojcyszyn D.: *The out-of-plane buckling length of chords of trusses*, *Inżynieria i Budownictwo*, 2004, No. 11.
- [3] Brzoska Z.: *The static and stability of the bar members structures*, Arkady, Warsaw, 1965.
- [4] SOFiSTiK. *Analysis Programs. V. 12.00 Manual*, SOFiSTiK AG., Oberschleissheim, 2002.
- [5] PN-B-6200:2002. *Building steel structures. Constructional steelwork specification. Basic Requirements.*
- [6] Biegus A., Wojcyszyn D.: *Współczynniki długości wyboczeniowej pasów z płaszczyzny ustroju "krótkich" kratownic*, III Sympozjon. Kompozyty. Konstrukcje warstwowe, Dolnośląskie Wydawnictwo Edukacyjne, Wrocław–Karpacz, 2004.

Współczynniki długości wyboczeniowej pasów z płaszczyzny ustroju „krótkich” kratownic

Analizowano stateczność pasów podczas wyboczenia z płaszczyzny ustroju „krótkich” kratownic. Badano 7 schematów statycznych kratownic, które różniły się wyężeniem prętów, topologią i sposobem podparcia. Rozpatrzono model obliczeniowy kratownicy płaskiej, uwzględniając jej przemieszczenia przygotowane oraz model przestrzennego ustroju prętowego. Wykonano analizy porównawcze współczynników długości wyboczeniowych pasów z płaszczyzny kratownic badanych modeli.

Tests of arch bridge made from corrugated steel plates

D. BĘBEN

Opole University of Technology, Katowicka 48, 45-061 Opole

Z. MAŃKO

Wrocław Technical University, Wybrzeże Wyspiańskiego 25, 50-370 Wrocław

The way in which a new road bridge made from *Super Cor* corrugated steel plates was tested during the three stages of its construction is described and the test results are presented. In construction stage I, the bridge was loaded with backfill and in stages II and III, with two ballasting vehicles. The box bridge spans the Bystrzyca Dusznicka River in Polanica Zdrój (Poland). The span's effective length is 12.27 m and its vertical inside diameter is 3.85 m. The steel span is founded on two reinforced concrete strip foundations. The average values of the displacements and strains (normal stresses) measured in selected points and on selected elements of the steel shell structure were much smaller than the ones computed for the same load. The conclusions drawn from this research can be helpful in determining the interaction between the steel shell and the backfill. Since this type of steel-soil structures are increasingly widely used in Poland and in the world, the conclusions can be extended to a whole class of similar bridge designs.

Keywords: *backfilling, corrugated plate, field static tests, road bridge, steel shell, backfill layer*

1. Introduction

Flexible box, arch, circular, elliptical, arch-circular or pear-shaped structures made from *Super Cor*, *Multiplate*, *Turvosider*, *Voest (Alpina)* and *Vario-Sec* corrugated steel plates [1, 2, 3] and founded on reinforced concrete continuous footings or on a sand or concrete mat laid on the ground [4] are highly suitable as small and medium-sized bridges (particularly road bridges) in situations when the latter are to be built in a relatively short time.

The results of the first in Poland static load tests of the road bridge made from *Multiplate* corrugated steel plates which spans the Plawna Stream in Stary Waliszów carried out after about four years of its service are reported in [5].

In this paper, the tests carried out during the three stages of construction of a single-span road bridge over the Bystrzyca Dusznicka River at the 1+470 km of the Polanica-Szczytna Zdrój district road 45117 in Polanica Zdrój are described. The bridge has a flexible superstructure made from *SC-54B Super Cor* corrugated steel plates which interacts with the surrounding backfill. High-tensile bolts joined the plates together. The bridge is founded on reinforced concrete strip foundations in the ground. The test results presented were verified by computations [6].

The various types of corrugated plates differ in, among others, the corrugation depth, pitch and width and in their thickness. For example, the plate thickness of *Mul-*

tiplate and *Super Cor* is 3.10 mm and 7.10 mm, respectively.

The aim of the tests was to check the performance of the new bridge structure under different loads during the three stages of its construction to verify the assumptions made in the static analysis and computations and in the test load design [6–8] and to determine the bridge's actual load capacity and the soil consolidation effect reducing the impact on its steel shell structure. During the three main bridge construction stages, i.e. soil compaction (stage I), bridge structure without deck (stage II) and completed bridge (stage III), deflections (vertical displacements) and strains were measured in selected points and cross sections in the steel shell in the longitudinal and transverse directions.

Those were the control and acceptance measurements required by the relevant bridge construction regulations [9–11]. Their aim was also to check whether the bridge span and strip footings (supports) had been solidly built and to provide the basis for a decision on putting in the bridge into service under a class B load (400 kN) in accordance with PN-85/S-10030 and for any post-construction and service recommendations. Mainly the actual stiffness of the corrugated plates in the single-span structure was estimated and the so-called mating (in carrying loads) width of the deck plate and the transverse distribution of load among the particular ribs of the corrugated plate were determined. The measurements were performed in three cross sections along the span length under loads symmetrical and asymmetrical relative to the span's longitudinal axis (three static load schemes I, II and III).

Considering the fact that the bridge is located on an important road in the Kłodzko Valley tourist area (and therefore heavily loaded) and that few steel-soil bridges with this kind of (prototype) span design and quite large effective spans are built in Poland or Europe (in 2001 it was the first and the longest bridge of this type in Europe), the initial routine range of acceptance tests on a bridge under a static load was extended by including, among others, tests under a backfill load, a dynamic load and a service load [6–8, 12, 13].

The conclusions drawn from the tests and the detailed displacement and strain analyses can be most helpful in bridge engineering practice [14], particularly in inspections and acceptance tests of steel-soil road and railway bridges made from corrugated or flat plates [1–8, 12–19]. It should be noted here that neither a universal computation method which would allow one to detail this kind of shell structures in a simple way [17–19] nor proper acceptance requirements have been developed so far. Hence this research may significantly contribute to the drawing up of such regulations.

2. Description of bridge

A previous bridge was damaged by the great flood in July 1997 – one of the bridgeheads was washed out and a part of the span slid into the river. Subsequently a detour (for cars only) was set up. In 2001, plans were made to rebuild the bridge using a flexible shell structure made from *Super Cor* steel zinc coated corrugated plates.

In the longitudinal section, the road bridge tested constitutes a restrained static single-span structure of the *box culvert* type – according to *Atlantic Industries Limited* (Canada) [6], having an effective span l_t equal to 12.270 m (Figure 1). In the cross section, the load-carrying structure is made from 140×380 mm steel corrugated plates of 7.10 mm thickness. The SB 8.8 class high tensile bolts M20 joined the plates together along the span width and length, using a twisting moment of 350–400 Nm [4, 18]. The steel shell structure of span was supported by means of steel uneven-armed channel sections, on two reinforced concrete strip foundations made from B30 grade concrete, placed between *Larssen* plate pile walls and braced (stiffened) at the top. On its circumference the bridge was finished with $0.40 \times 0.45 \times 0.95$ m reinforced concrete collars to increase the span transverse rigidity and to secure the embankment slopes and the slope cut-offs, faced with natural stone bonded with cement-lime mortar, on the two sides at 1:1.5.

Structural steel of the strength corresponding to that of Polish steel St3M (the yield point of the steel used to manufacture *Super Cor* corrugated plates is in the range of 275–380 MPa [6, 8]) was used for the shell structure.

The steel corrugated plates on both sides were coated with 85 μm thick layer of zinc. In addition, a 200 μm thick coating of epoxy paint was applied to the outer parts of the inlet and outlet up to a height of 1.50 m.

The shell structure was reinforced with additional corrugated plates spaced at every 380 mm in three places, i.e. in the crown and in the haunches (at the strip foundations) on the soil side on both sides of the bridge, to endow the superstructure with greater longitudinal and lateral stiffness since the computations and analyses made by the manufacturer (*Atlantic Industries Limited*) indicated that the largest bending moments and axial forces, and so the largest normal stresses, occurred in the above-mentioned cross sections. The load-bearing structure of span was designed as a flexible shell consisting of steel corrugated plates filled up with 0.20–0.30 m thick course of permeable soil with 10–32 mm grading, compacted to $I_D = 0.95$ (on the Proctor scale) for the soil being in direct contact with the steel shell and to $I_D = 0.98$ for the other backfill whereby a pavement could be laid on a broken stone subgrade. The soil which surrounds the shell carries a large share (about 70%) of the load through the so-called arching while the rest of the load is carried by the shell structure [4]. The overall height of the *Super Cor* plate corrugation is $h = 140$ mm. The structure width is $b_t = 13.60$ m at the top and $b_b = 20.60$ m at the bottom and its clear height is $h_o = 3.85$ m. In plan, the bridge is situated at a skew of $\alpha = 60^\circ$ relative to the river current. This had to be considered when positioning the test load on the bridge (Figure 1d).

The bridge has two culverts made from $\phi = 1000$ mm *Pecor* pipes to carry and discharge the increased flow of water during spring thaws or freshets, which constitute the main points of water thrust during a disaster (then the backfill around and above the shell is allowed to be destroyed to prevent damage to the steel shell). The shell was secured in the strip foundations by means of a 0.50 m high reinforced concrete flange (Figure 1). The bridge had two sidewalks, each 1.50 m wide, on both sides of the

roadway and typical SP-06 barriers. Two gabions, directing the flow of water through the bridge to protect the supports (the strip foundations) and the embankment cones against washing, were provided at the bridge entrance and exit [6].

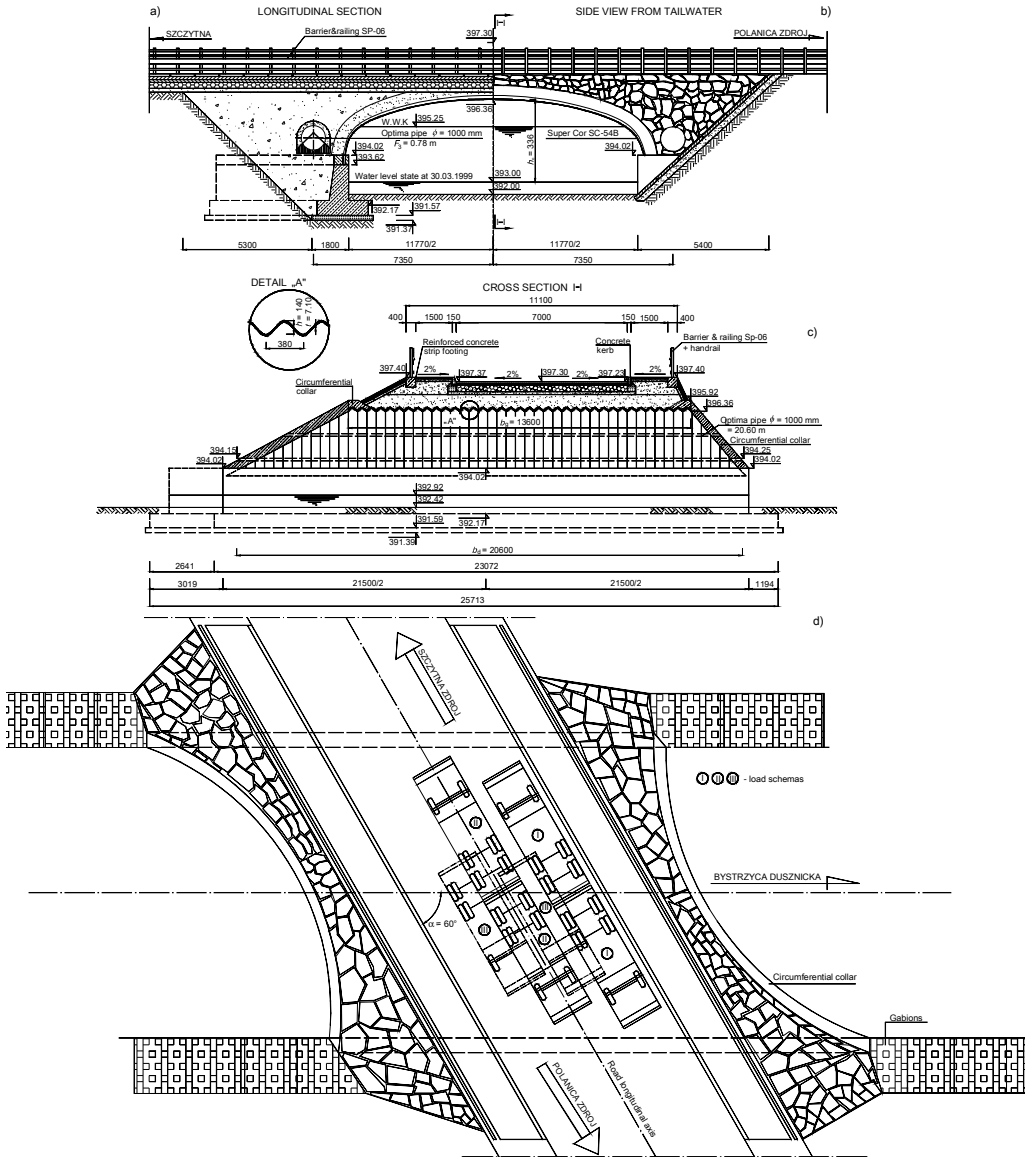


Fig. 1. Road bridge in Polanica Zdrój made from *Super Cor* steel plates: a) longitudinal section, b) tailwater side view, c) cross section and d) top view on load schemes

The span structure of the bridge was assembled in as few as 9 days by only seven workers and one low-capacity lift. All the work was supervised by the investor and the steel structure supplier [6].

3. Range of the tests carried out on the bridge

The strains and displacements of the steel shell were measured twice during backfilling and compaction (stage I) for selected soil (sand and broken stone) layers as shown in Figure 2. Two trucks (a Jelcz Steyer and Kamaz 5511) were used for the trial static and dynamic loading of the finished bridge (stage III) and for the measurements performed during its construction, i.e. when the bridge was still without its base road foundation (stage II), to produce effort in selected places and elements of the shell structure. The total weight of the two trucks amounted to over 500 kN. Each time the vehicles with possibly the heaviest axle loads were so positioned in the lateral and longitudinal directions of span as to produce maximum deflections and strains in the tested sections of the span. The vehicles were arranged symmetrically and asymmetrically in the span cross section to distribute the effort among the particular ribs of the corrugated plates. Also the ratio of test load effects to design load effects (i.e. for class B load in accordance with PN-85/S-10030) was determined. The ratio of test-load span bending moments to bending moments produced by moving service loads was 70–75%. This magnitude of the load was considered to be reliable in the light of the relevant Polish bridge standards [10, 11].



Fig. 2. Headwater side view of assembled steel shell structure before backfilling (test stage I)

During the tests not only the types of the vehicles but also their axle loads were changed from the ones originally assumed in the test load scheme [6, 7 and 8]. The

reason was that the vehicles' load was found to exceed their maximum authorized overload. The weighed front and rear axle loads together considerably exceeded the total weight of truck (including the load). Therefore the load surpluses were distributed proportionally to the vehicles' catalogue load capacities. The axle loads of the trucks used in test stages II and III are given in Table 1. The weighed axle loads and the loads calculated (using relevant catalogues) from the distribution of load capacity per axles are shown in the top and bottom rows, respectively. Since during the tests the rear axles (with larger loads) were positioned in the critical sections of span, the actual weighed axle loads were used in the computations to ensure a proper margin of safety for the structure. Because of so large differences between the weights of the delivered trucks and the test load program weights the expected static quantities (normal stress and displacement) had to be recalculated [6]. But the overloaded vehicles could be used to produce much stronger dynamic effects [12].

Table 1. Ballasting trucks' axle and wheel loads [kN] in test stages II and III

Test stages	Mark of truck	Truck number	Total weight	Axle loads		Wheel loads	
				Rear	Front	Rear	Front
II	Jelcz Styer (DKLL 997)	1	284.00	235 = 2×117.50 207 = 2×103.50	49.00 77.00	58.75 51.75	22.50 37.00
	Kamaz 5511 (WYB 3750)	2	233.00	192 = 2×96.00 169 = 2×84.50	41.00 64.00	48.00 42.25	20.00 32.00
III	Jelcz Styer (DKLL 997)	1	279.00	234 = 2×117.00 205 = 2×102.50	45.00 74.00	58.50 51.25	22.50 37.00
	Kamaz 5511 (WYB 3750)	2	221.00	181 = 2×90.50 159 = 2×79.50	40.00 62.00	45.25 39.75	20.00 31.00

The tests during stages II and III were to be carried out in the full range of static loads and they were to include measurements of displacements and strains (indirectly normal stresses) at selected points in several sections of the structure. Since in this kind of structure possible settlement of the strip foundations had already taken place and considering the fact that bedrock was beneath and no deviations or irregularities in the foundations' behaviour or work had been observed prior to the bridge tests, strip foundation settlement was not continuously recorded. Instead it was checked by means of a precision surveyor's level.

As originally planned, three load schemes (Figures 3–5), i.e. an asymmetrical load scheme (scheme I: both trucks positioned at one curb on the tailwater side) and two symmetrical load schemes (scheme II: the two trucks positioned in such a way that their longitudinal axes coincided with the longitudinal axis of the bridge and their rears touched at half of the effective span of bridge (in the crown) and scheme III: the trucks positioned on both sides of the longitudinal axis of bridge so that their rear axles were situated at half the bridge's effective span). The finished bridge put into service is shown in Figure 6.



Fig. 3. Top view of bridge during tests under load scheme II in test stage II



Fig. 4. View of bridge during tests under load scheme III in test stage II



Fig. 5. View of bridge during tests under load scheme III in test stage III



Fig. 6. Headwater side view of steel road bridge made from *Super Cor* corrugated plates located in Polanica Zdrój

Two measuring systems were used to measure strains and vertical (deflections) and horizontal displacements. Each system consisted of three basic components: measurements, control measurements and recording of results.

For each scheme of loading the bridge superstructure the following quantities were to be measured:

- strains (indirectly normal stresses) during the assembly of the steel shell (during the compaction of the soil layers) – stage I,
- horizontal and vertical (deflections) displacements in the particular span sections (in the middle and at the end of the crown reinforcement of shell and in the bridge haunch) in two test stages: without bridge road foundation – stage II and after bridge completion (the test loading proper) – stage III,

- strains in the selected sections of the corrugated plates (in the crown, at the end of the shell reinforcement and in the shell haunch) in two test stages: without bridge road foundation – stage II and after bridge completion – stage III,
- strip foundation settlement during the tests,
- the effect of dynamic interactions on the displacement (deflection) of the corrugated plates and on the strains in the selected points and cross sections of the bridge span,
- pressures in the ground.

Strains (indirectly normal stresses) were measured by electric resistance wire strain gauges which were stuck on at fixed points (the surface had been prepared by its grinding and cleaning with acetone or spirit). Appropriately aged (for better stability) RL 20/120 gauges (made by Tenmex in Łódź, Poland) were used. Their measurement base was 20 mm, the resistance $R = 120.6 \Omega \pm 0.2 \Omega$ and the constant $k = 2.15 \pm 0.5\%$.

Seven dial gauges were used to measure the vertical displacements (deflections) of the load-carrying structure in stage II and eight induction gauges WT50S with a reading accuracy of 1×10^{-5} m, connected by cables to a Hottinger UPM-60 bridge and to a six-channel instrumentation amplifier KWS673.A7 from which the output voltage signal was directed simultaneously to the input of the multipoint UPM-60 measuring device and to the inputs of an eight-channel fast recorder 330-P/8, were used in stage III.

Two Glöetzl hydraulic sensors (earth pressure cells), placed in the ground at a depth of 1.00 m from the road surface in the middle of the roadway and at its edge on the headwater side at a distance of about 0.50 m from the steel shell, were used to measure pressure in the ground.

Prior to the tests the measuring circuits in the recording instruments had been calibrated for a fixed displacement value, e.g. 30 mm. The first indications (zero readings) had been obtained before the load was brought onto the span. After the ballasting load was brought onto the span further readings were taken from all the instruments at every 10 minutes for at least 30 minutes and after unloading until the readings stabilized. If the difference between two consecutive readings was larger than 2%, the load had to remain on the span until the difference was below 2% [10, 11, 20, 21]. And similarly, readings were taken after unloading the span, i.e. at every 10 minutes for 20 minutes. At least three such readings were taken. The differences between the last indications of the dial (or induction) gauges and the electric resistance wire strain gauges after unloading and the initial readings represented the permanent deflections (strains) and the differences between the total deflections (strains) and the permanent ones constituted the elastic deflections (strains).

The condition of the shell span structure and the bridge supports was checked before, during and after the test static and dynamic loading [10, 11]. The main measuring setup was located in one of the culverts to protect it from rain [6, 7, 8]. All the measuring instruments and the auxiliary equipment were transported to the test site and stored in a delivery van. The whole setup was remotely controlled (direct manual control was also possible) from one measuring position.

4. Assessment of measurement accuracy

Probable measuring error δ_e for strains in the steel shell structure for the worst measuring setup was calculated from the approximate formula:

$$\delta_e = \sqrt{\delta_1^2 + \delta_2^2 + \delta_3^2 + \delta_4^2} = \sqrt{0.015^2 + 0.015^2 + 0.02^2 + 0.025^2} = \pm 3.84\% , \quad (1)$$

where:

$\delta_1 = 1.5\%$ – a strain gauge error,

$\delta_2 = 1.5\%$ – a channel selector compensating unit error,

$\delta_3 = 2.0\%$ – an instrumentation amplifier error,

$\delta_4 = 2.5\%$ – a steel elasticity modulus error.

The probable measuring error for displacements in the selected sections of the steel corrugated-plate shell structure at the best setup of converters and measuring instruments was calculated from the approximate formula:

$$\delta_f = \sqrt{\delta_5^2 + \delta_6^2 + \delta_7^2 + \delta_8^2} = \sqrt{0.015^2 + 0.01^2 + 0.02^2 + 0.01^2} = \pm 2.87\% , \quad (2)$$

where:

$\delta_5 = 1.5\%$ – a displacement converter error,

$\delta_6 = 1.0\%$ – a channel selector scale unit error,

$\delta_7 = 2.0\%$ – an instrumentation amplifier (bridge) error,

$\delta_8 = 1.0\%$ – a calibration error.

5. Measurements of strains and vertical displacements

5.1. General

A peculiarity of flexible bridge structures made from steel corrugated plates is that the backfill around the shell participates in carrying the live load originating from the soil layers (stage I) and from the wheels of the vehicles crossing the bridge (stages II and III). If the surrounding soil is to fully mating with the steel shell in carrying a substantial part of the load, the layers of it should be properly laid down around the shell and skilfully and carefully (so that the allowable stress in the plate metal is not exceeded) compacted to a proper degree, e.g. in the case considered I_D was respectively 0.95 and 0.98 on the Proctor scale. Soil is usually compacted using mechanical compactors whose action and the dead weight of the soil layers significantly affect the state of stress (strains) and the stability of the steel shell structure. If the permissible stresses in the shell are not to be exceeded they must be continuously monitored, e.g. through the measurement of strains. In order to get a comprehensive picture of the state of stress in the shell structure in the different stages of bridge construction,

strains and vertical displacements were measured during the assembly of the steel shell and during the compaction of the particular soil layers around it (stage I), after several road base layers and a 0.05 m thick asphaltic concrete layers were laid (stage II) and when the completed bridge was subjected to the test static load (stage III). The initial, maximum and final readings for all the measuring points used in the analysis are given in tables in [6].

The calculations results obtained differed considerably from the experimental ones due to the fact that it is extremely difficult to specify the interaction between the steel shell structure and the backfill [6] in the computing model.

The influence lines of the transverse distribution of load among the individual corrugated plates were used to calculate the expected values of the deflections f , the strains ε and the normal stresses σ .

The determination of the extent to which the steel shell structure mating with the surrounding backfill in carrying loads and the proper modelling of the interface between the corrugated plate structure and the soil presented major difficulties in the analyses. Computations were performed for the actual positions and loads of the ballasting vehicles' axles. The ordinates of the influence lines under the axles were read directly from computer printouts to avoid needless and extremely laborious (and also less precise) interpolation of the ordinates. The Robot Millennium computer program was used to verify the computations for the same or similar assumptions and the values obtained were close to the ones computed by the Cosmos/M program [22, 23].

5.2. Results obtained in the test stage I

- **Strains.** The diagrams of the maximum strains measured in three cross sections along the length of the steel shell, i.e. in the crown, at the end of the crown reinforcement and in the haunch, during the compaction of soil around this structure are shown in Figure 7. The measurements were performed twice – for two different layers of compacted soil, i.e. for sand (layer 6) and broken stone (layer 12 from the natural ground). In all, 18 layers (alternately sand and broken stone) were used in backfilling.

- **Vertical displacements.** Since it was impossible to erect scaffolding in the rapid current of the mountain river (the tests were conducted after heavy rains) neither vertical nor horizontal displacements of the selected steel shell points during the compaction of the selected soil layers could be recorded. Furthermore, the shell would deform quite considerably in all directions whereby proper recording of the actual displacements was rather impracticable, all the more because the construction work was being carried out on this structure.

5.3. Results obtained in the test stage II

- **Strains.** The variations of strains with time at selected points of the bridge shell structure for three load schemes recorded during construction stage II (without road-

way layers) are given in paper [6]. The traces of maximum strains in the transverse direction of span at the selected points of the structure for the three cross sections tested, i.e. respectively in the shell crown, at the end of the crown reinforcement and in the shell haunch for static load schemes I, II and III are shown in Figure 8.

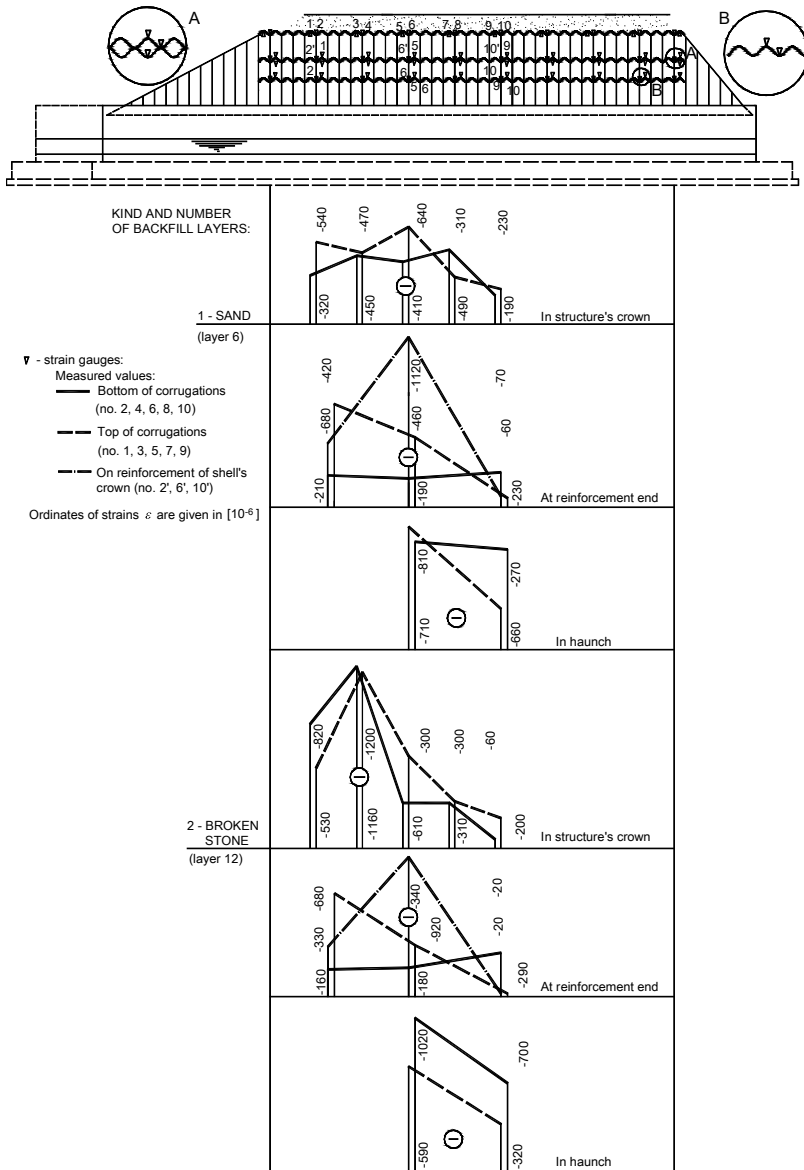


Fig. 7. Maximum strains in selected points of shell in transverse direction during compaction of backfill layers in stage I

• **Vertical displacements.** The variations of vertical displacements with time at the selected points of the shell structure are given in [6]. The traces of maximum vertical displacements in the transverse direction of span for load schemes I, II and III recorded during test stage II are shown in Figure 8a.

• **Pressures in ground.** The pressures in the ground measured by earth pressure cells located very close to the steel shell were neglected in the analysis since the readings were not accurate enough and sometimes no readings were obtained – probably the cables connecting the gauges with the measuring apparatus were damaged by too fast compaction of individual backfill layers close to the earth pressure cells by the different contractors or through the use of soil of not always proper grading (e.g. large stones or boulders dredged from the river).

5.4. Results obtained in the test stage III

• **Strains.** The variations of strains with time at the particular points for the particular cross sections (elements) of shell are given in paper [6]. The traces of maximum strains in the transverse direction of span at the selected points of the shell for the two cross sections tested, i.e. in the crown and at the end of the crown reinforcement, for test static load scheme I, II and III (test stage III) are shown in Figure 9.

• **Vertical displacements.** In order to carry out a comprehensive analysis of the test static load measurements, the traces of the vertical displacements with time of the points of steel shell in the particular cross sections along the bridge length were presented in detail in paper [6]. The traces of maximum displacements in the transverse direction of span for load schemes I, II and III were presented in Figure 9b.

5.5. Standard conditions for evaluation of test results

In order to obtain a passing grade for a bridge structure on the basis of the results of tests carried out at different stages of its construction and finally under the test load in accordance with the bridge code for typical steel bridges [9–11], the following conditions must be fulfilled:

- a) the computed and measured displacements and strains of bridge shell are similar,
- b) the tests did not cause any damage to the structural components or their joints,
- c) the steel shell structure deformed elastically within the allowable displacement range under loads close to the standard loads and the displacements did not exceed the calculated ones,
- d) the permanent deflections (vertical displacements) of the load-carrying structure amounted to less than 25% of the elastic deflections.

It should be noted here that guidelines or regulations for structures of this type do not yet exist in Poland whereby the contractors often have problems with the acceptance of such bridges by the bridge administration.

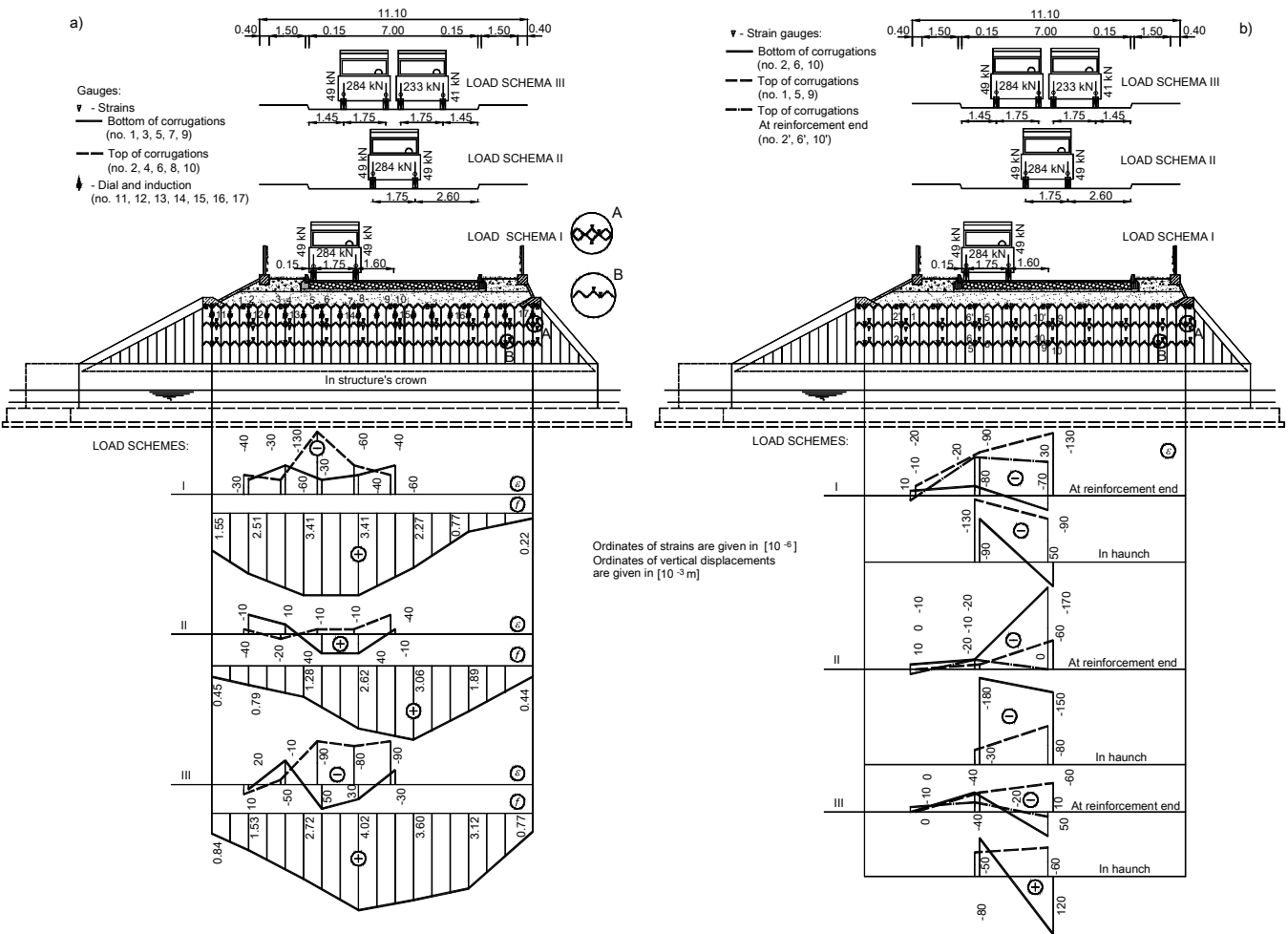


Fig. 8. Diagrams of maximum strains and vertical displacements in transverse direction: a) in crown and b) at reinforcement end and in shell haunch for three load schemes I, II and III in test stage II

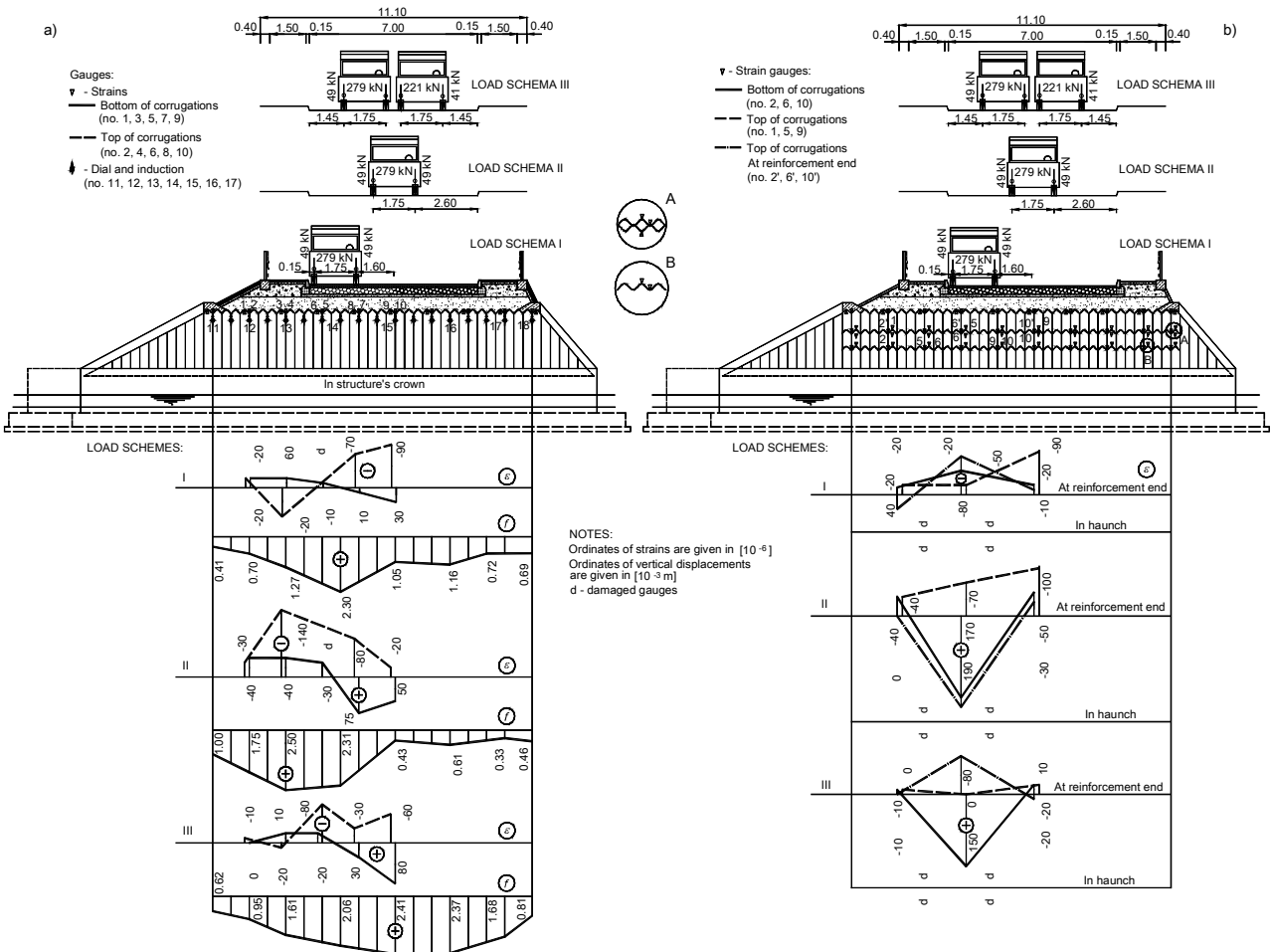


Fig. 9. Diagrams of maximum strains and vertical displacements in selected points of steel shell structure in transverse direction: a) in crown and b) at reinforcement end and in shell haunch for three load schemes I, II and III in test stage III

6. Analysis of test results

6.1. Normal stresses measured in corrugated plates

The strains measured in the three stages of testing the steel shell structure of bridge were used to compute the normal stresses shown in Tables 2 and 3. During static load test stages II and III also the vertical displacements (deflections) at the selected points and in the specified cross sections of the steel shell structure were measured (Table 4).

- **Test stage I.** The largest normal stresses – about 240 MPa – in the steel shell structure during the compaction of soil layers (i.e. layers 6 (sand) and 12 (broken stone)) occurred in its crown (on the top edges of the corrugations). During the compaction of sand layer 6 the maximum stresses recorded in the crown in the same cross section amounted to 130 MPa and they were concentrated in the bottom edges of the corrugations. In the next cross section considered, i.e. at the end of the crown reinforcement, the largest normal concentrations – about 225 MPa – occurred in the corrugations' top edges during the compaction of sand layer 6. During the compaction of broken stone layer 12 around the steel shell the largest stresses – about 185 MPa – occurred on the top edges of the structure reinforcement (the additional reinforcing corrugated plate). In the structure haunch (at the shell-strip foundation joint), the maximum strains were measured in the corrugations' bottom edges during the compaction of broken stone layer 6 and the normal stresses computed on this basis amounted to about 200 MPa. During the compaction of sand layer 6 the largest strains, and so the largest normal stresses – 160 MPa, were recorded in the corrugations' top edges (Figure 7).

- **Test stage II.** The largest normal stresses in the steel shell structure were obtained from the measurements of strains in the haunch, i.e. at the strip foundation, during construction stage II (cross section III–III) and they were as follows (Figure 8b):

- a) load scheme I (two trucks positioned at the roadway curb) – 27 MPa on the corrugations' top edges between the vehicles' wheels,

- b) load scheme II (two trucks positioned in the middle of the effective span (in the longitudinal direction) and in the middle of the bridge roadway (facing a transverse direction of the bridge) – nearly 37 MPa at the bottom edge of the corrugations towards the acute angle of the span skew,

- c) load scheme III (two trucks positioned parallel to each other at half of the effective span in such a way that the span longitudinal axis was between the two rear axles of vehicles taking into account the fact that the bridge is situated at a rather large skew in plan) – about 25 MPa on the corrugation bottom edges between the two trucks' wheels.

Slightly smaller strains (and thus normal stresses) were recorded in the cross section situated at the level of the end of the shell crown (cross sections II–II) and they were as follows (Figure 8b):

a) load scheme I – 27 MPa in the corrugations' top edges almost in the middle of the roadway width,

b) load scheme II – nearly 35 MPa concentrated in the corrugations' bottom edges between the vehicles' wheels,

c) load scheme III – about 12 MPa in the corrugations' top edges under the vehicles' wheels.

In the first cross section tested, i.e. in the crown of a steel shell structure (cross section I-I), the largest normal stresses computed on the basis of the strains measured were as follows (Figure 8a):

a) load scheme I – 27 MPa in the corrugations' top edges under ballasting trucks' wheels,

b) load scheme II – about 10 MPa both in the corrugations' bottom and top edges under the trucks' outside wheels,

c) load scheme III – 20 MPa in the corrugations' top edges directly under the trucks' wheels.

Table 2. Maximum normal stresses [MPa] in steel shell obtained from measurements in test stage I

Gauge number	Analyzed cross section at span shell level					
	Crown	Reinforcement end	Shell haunch	Crown	Reinforcement end	Shell haunch
	Sand (layer 6)			Broken stone (layer 12)		
1	66	139	–	168	139	–
2	111	86	–	109	68	–
2'	–	43	–	–	33	–
3	92	–	–	240	–	–
4	96	–	–	238	–	–
5	84	220	146	61	185	200
6	130	94	160	125	70	121
6'	–	39	–	–	37	–
7	100	–	–	61	–	–
8	64	–	–	64	–	–
9	39	47	55	12	59	66
10	47	14	135	41	4	144
10'	–	12	–	–	4	–

' – gauge located on top edge of reinforcing sheet.

• **Test stage III.** The largest normal stresses in the steel shell structure, based on the strains measured during the test loading of the bridge (test stage III) with two trucks, occurred at the end of the crown reinforcement of shell (cross section II-II) and they were as follows (Figure 9b):

a) load scheme I – about 20 MPa concentrated in the corrugations' top edges in the middle of the roadway width,

b) load scheme II – nearly 38 MPa in the corrugations' top edges (on the reinforcement) towards the span skew,

c) load scheme III – about 30 MPa localized in the corrugations' bottom edges towards the span skew.

Table 3. Maximum normal stresses [MPa] in shell structure obtained from measurements in test stages II and III

Load schemes	Gauge number	Cross section of shell in test stage II			Cross section of shell in test stage III		
		Crown	Reinforcement end	Shell's haunch	Crown	Reinforcement end	Shell haunch
I	1	8	2	–	4	8	–
	2	6	4	–	4	4	–
	2'	–	2	–	–	4	–
	3	6	–	–	12	–	–
	4	12	–	–	4	–	–
	5	27	19	27	d	10	d
	6	6	16	19	2	4	d
	6'	–	4	–	–	16	–
	7	12	–	–	14	–	–
	8	8	–	–	2	–	–
	9	8	6	10	19	4	d
10	12	27	19	6	19	d	
10'	–	14	–	–	2	–	
II	1	2	2	–	6	8	–
	2	8	0	–	8	8	–
	2'	–	2	–	–	0	–
	3	2	–	–	8	–	–
	4	4	–	–	29	–	–
	5	2	4	6	d	35	d
	6	8	2	37	6	15	d
	6'	–	4	–	–	39	–
	7	2	–	–	15	–	–
	8	8	–	–	16	–	–
	9	8	0	31	10	10	d
10	2	35	16	4	21	d	
10'	–	12	–	–	6	–	
III	1	4	0	–	0	2	–
	2	2	0	–	2	0	–
	2'	–	2	–	–	2	–
	3	2	–	–	2	–	–
	4	10	–	–	4	–	–
	5	19	8	10	4	31	d
	6	10	8	16	16	0	d
	6'	–	4	–	–	16	–
	7	12	–	–	6	–	–
	8	6	–	–	6	–	–
	9	19	10	25	16	4	d
10	6	2	12	12	2	d	
10'	–	12	–	–	4	–	

d – damaged gauge, ' – gauge located on top edge of reinforcing sheet.

For the crown of steel shell structure (cross section I–I) the following normal stresses were obtained (Figure 9a):

- a) load scheme I – about 20 MPa concentrated in the corrugations' top edges in the middle of the roadway width,
- b) load scheme II – nearly 30 MPa in the corrugations' top edges towards the span skew,
- c) load scheme III – about 17 MPa in both the top and bottom edges of the corrugations towards the span skew.

In cross section III–III, the strain gauges were damaged (probably while backfilling and compacting the soil around the steel shell) or their operation did not guarantee correct readings and so this cross section was passed over in the analysis.

On the whole, the strains (normal stresses) at the selected points of the shell, similarly as the deflections (vertical displacements) of the steel shell, would return to the original position during both test stage II and the test loading (test stage III). The results obtained were traced through the different stages of construction of the bridge shell structure. The behaviour of the shell structure in all the test stages did not raise any suspicions. Only the soil stabilization (distressing) was rather slow and after the unloading of the span the gauges took a rather long time to return to their original readings which might raise some suspicion, particularly in comparison with the behaviour of gauges in the case of conventional steel or concrete spans [6, 7, 8].

Similar observations can be made if one analyses, on the basis of the diagrams of the strains ε and the vertical displacements f shown in Figures 7–9, the distributions of strain (normal stress) in several cross sections of the steel shell structure, their linear distributions in the cross sections of the corrugations, the interaction between the particular corrugated plates and the interaction between the steel shell and the surrounding backfill.

A comparison of the results presented in the strain diagrams (Figures 7–9) shows that the maximal normal stress values obtained on the basis of the strain measurements for the same ballasting loads were the biggest at the crown (cross section I–I). There were no significant differences between the initial and final readings or the differences were so slight that they stayed within the extensometer reading accuracy limits of bridge [22].

6.2. Vertical displacements

• **General observations.** An analysis of the displacement values measured in all the selected points and cross sections of the steel shell made from *Super Cor* corrugated plates showed the elastic character in every case for all the three static load schemes [22].

The quite large differences between the initial and final readings (permanent displacements) were not roughly identical in all the considered points and cross sections for the three load schemes and the steel load-bearing structure took much longer to

distress in comparison with conventional steel or concrete bridges. This may indicate that the differences were to some degree due to the stabilization of soil (backfill) layers, the possible settlement of the strip foundations and small reading errors of the measuring devices and to a large degree due to the permanent deformations of the load-carrying structure of shell interacting with the ground because corrugated plates joined together by high-tensile bolts (and so forming a flexible structure) should not show substantial permanent deformations. But considering the fact that the reinforced concrete strip foundations (supports) and the soil-shell system were quite new (not subjected to such a considerable load before) one could expect that they would settle somewhat when first time subjected to a relatively heavy service load (over 500 kN) close to the standard load, and probably adjustment between some of its structural members, particularly between the corrugated plates and between the shell structure and the backfill around it, took place.

• **Results obtained in test stage II.** The largest vertical displacements of the shell structure (the corrugated-plate load-carrying structure of the bridge, Figure 8a and Table 4) during test stage II were registered under load scheme III, i.e. for two trucks positioned parallel to each other in the middle of the effective span in such a way that the longitudinal axis of span was between the two rear axles of vehicles (it should also be noted that the bridge is situated at a rather large skew). The maximum displacements were 4.02×10^{-3} m and they occurred directly under the trucks' wheels. Also under load scheme I, when the two trucks were positioned close to the curbs, the largest displacements of load-carrying structure amounted to 3.41×10^{-3} m and they also occurred under the ballasting vehicles' wheels. Under load scheme II, when the two trucks were positioned in the middle of the effective span (in the bridge longitudinal direction) and in the middle of the roadway (if one faces the road transverse direction), the deflections amounted to 3.06×10^{-3} m and they also were concentrated under the ballasting vehicles' wheels.

• **Results obtained in test stage III.** The largest vertical displacements of the shell structure (the corrugated-plate load-carrying structure) during test stage III were registered under load scheme II (Figure 9a and Table 4), i.e. when the two ballasting vehicles were positioned in the middle of the effective span (in the longitudinal direction) and in the middle of the roadway (if one face the bridge transverse direction). They amounted to 2.50×10^{-3} m and were concentrated in the direction of the acute angle of the spans skew. Under load scheme I the largest displacements of the load-carrying structure were 2.30×10^{-3} m and they occurred directly under the ballasting vehicles' wheels. Under load scheme III, i.e. when the two trucks were positioned in the middle of the effective span parallel to each other so that the span longitudinal axis was between the vehicles' two rear axles (it should also be noted that the bridge in plan is situated at a large skew), the maximum displacements amounted to 2.41×10^{-3} m and also occurred under the vehicles' wheels.

Table 4. Maximum vertical displacements [10^{-3} m] in selected points of steel shell structure obtained from measurements in test stages II and III

Gauge number	Load schemes					
	I	II	III	I	II	III
	Test stage II			Test stage III		
11	1.55	0.45	0.84	0.41	1.00	0.62
12	2.51	0.79	1.53	0.70	1.75	0.95
13	3.41	1.28	2.72	1.27	2.50	1.61
14	3.41	2.62	4.02	2.30	2.31	2.06
15	2.27	3.06	3.60	1.05	0.43	2.41
16	0.77	1.89	3.12	1.16	0.61	2.37
17	0.22	0.44	0.77	0.72	0.33	1.68
18	–	–	–	0.69	0.46	0.81

7. Conclusions

As a result of measurements carried out on the road bridge in Polanica Zdrój (during the construction of the shell and backfilling and under the main test static load) the vertical displacements (deflections) of the load-carrying structure and the strains (indirectly the normal stresses) in the selected points and cross sections of the span were determined. Taking into account the practical experience gained from the tests conducted using a static or dynamic load on other existing bridges made from *Super Cor* or *Multiplate* corrugated plates, e.g. in Szczytna Zdrój [7], in Gimån (Sweden) [1, 14, 16], in Stary Waliszów [5], in Poznań-Rubież [4] and in Trzebaw [3], and on natural-scale test stands [24, 25], the observations of the behaviour of the shell structure in this type of bridge during the tests and a comprehensive analysis of the measurement results, the following general and specific conclusions about the actual behaviour of the bridge can be drawn:

1. The performance of the bridge (the soil-shell system and the strip foundations) under the backfill load (stage I) and the static loads (stages II and III) did not give rise to reservations. The strain and displacement values obtained were very small and it was clear evidence of much greater stiffness of the span shell than the one assumed in the static analysis in which such a degree of interaction between the steel shell structure and the surrounding backfill was not foreseen (Tables 2, 3 and 4) [6, 22].

2. The measured deflections of the steel load-carrying structure made from corrugated plates joined together only by high-tensile bolts and the strains measured on the lower and top corrugations and on the additional reinforcing plates subjected to a load in the form of, among others, backfill during test stage I and the set of two trucks with a total weight of over 50 Mg during test stage II and III had practically elastic character. The rather large differences between the initial and final readings (permanent displacements and strains) were not roughly identical in all the cross sections under the three load schemes and the steel load-carrying structure took much longer to distress in comparison with conventional steel or concrete bridges. This may indicate that the

differences were rather due to small reading errors and errors of the measuring devices (changes in temperature and air humidity during the measurements) or due to the settling of the strip foundations and only to a slight degree due to the permanent displacements and strains of the load-carrying structure itself – most probably due to the uneven contact between the corrugated plates and the strip foundations since the corrugated plates joined together by high-tensile bolts should not show substantial permanent displacements.

3. The differences can be attributed to good mating between the steel shell and the ground and the road surface and to the fact that rather stiff road structure contributes to the distribution of the large concentrated load over a much larger area extending beyond the perimeter of the shell structure and the measuring area covered with the gauges. As a result the strains originating directly from the vehicles' wheels acting on the shell were reduced. In addition, the flexibility of the steel shell structure favourably affected the carrying of service loads and load arching manifested itself in the ground.

4. The permanent displacements (amounting to less than 2% of the total deflections) measured in the particular points and cross sections of the steel shell structure in the bridge tested differed from each other only slightly and they were not proportional to the elastic deflections. The line of transverse elastic deflections in the shell structure under the field loads obtained from the measurements had curvilinear character (broken curve).

5. The sharp bends in the deflection and strain diagrams in the cross section of the bridge (Figures 8 and 9) can be caused by bends at the high-tensile bolted joints between the corrugated plates or deformations of the steel shell under the ballasting trucks' wheel loads located in the central part of roadway where stiffening reinforced concrete collars were missing. They may also be due to the fact that the displacements (deflections) and strains of the corrugations were not measured across the entire width of the span cross section, but only at selected points of its cross section (the top and bottom of the corrugations) whereby the ordinates of the corrugations' deflections cannot be directly connected in a curvilinear way.

6. The registered settlements of strip foundations (supports) were slight and they were rather due to inaccuracy of readings or instrumental errors or irregularities between the corrugated plates and the foundation. The settlements were found to be so slight and uncertain that their influence on the other deflection or deformation values was neglected, especially in view of the considerable load capacity reserves in the shell structure of the bridge. Since it was the first time that the strip foundations were to be subjected to such a heavy static load, one could naturally expect some settlement, especially buckling of the plates at the joint with the foundation.

7. The position of the neutral axis in the cross sections of the load-carrying structure (corrugated plates) and the strain values prove that the steel structure interacts closely with the surrounding backfill and the pavement laid on the soil layers. This interaction was the main factor that affected the magnitude of the displacements and

strains obtained. The neutral axes of the cross sections of steel shell structure are situated slightly higher than it can be expected based on the strength computations [22].

8. The strains and vertical displacements measured tended to decline with successive measurements (test stages). Their highest values were obtained in test stage I under the backfill load when the shell structure is highly sensitive to external loads, and the lowest values were recorded in stage III under a proper static test load. This is a clear evidence that consolidation and stabilization of the soil around the steel shell structure take place and that the multilayer roadway structure contributes to a significant reduction in the shell effort – vertical displacements and strains (as a comparison of stages II and III shows).

9. During a close inspection of the bridge and its high-tensile bolted joints and during supplementary and control measurements the bridge was found to be in good condition, its performance under the large static (and dynamic) service load did not raise any suspicions and none of the structural elements suffered any damage.

10. To make complete the analysis of the state of strains, displacements and pressures in the backfill around the steel shell structure, supplementary measurements, i.e. of pressure distributions in the ground near this structure, are to be carried out in the future. Maybe then it will become possible to determine the causes of the inaccuracies in pressure measurements during the principle tests in stages II and III.

11. Having passed the backfill load test, the shell was accepted for further construction work, static and dynamic testing and ultimately normal class B load service [6, 10].

References

- [1] Bęben D., Mańko Z.: *The first in Scandinavia bridge made from steel corrugated plates Super Cor type* (in Polish), *Bezpieczne Drogi*, Warsaw, 2003, No. 11(59), 18–22.
- [2] Bęben D., Mańko Z., Janusz L., Vaslestad J.: *Tests of Gimån (Sweden) a road bridge steel shell made from corrugated plates, Super Cor SC-54B type, carried out during backfilling* (in Polish), 2nd Scientific-Technical Symposium on Bridge Testing and Diagnostics, Opole, 2003, 31–67.
- [3] Bęben D., Czyżewski P., Mańko Z.: *Construction of the largest in Europe bridge made from steel corrugated plates Super Cor type* (in Polish), *Inżynieria i Budownictwo*, Warsaw, 2004, No. 4, 74–77.
- [4] Madaj A., Vaslestad J., Janusz L.: *In situ testes of steel corrugated-sheet culvert used for retrofitting railroad framed overbridge* (in Polish), 9th Seminar on Modern Methods of Reinforcing and Retrofitting Bridges, Poznań–Kiekrz, 1999, 106–117.
- [5] Bęben D., Mańko Z.: *Static tests of road corrugated-plate bridge* (in Polish), *Roads and Bridges Research Institute Quarterly “Drogi i Mosty”*, Warsaw, 2003, No. 3, 5–30.
- [6] Bęben D., Mańko Z.: *Experimental tests of a road bridge with flexible structure made from steel corrugated plates of Super Cor SC-54B type, under static load* (in Polish), 2nd Scientific-Technical Symposium on Bridge Tests and Diagnostics, Opole, 2003, 69–120.
- [7] Bęben D.: *Tests of a road bridge made from steel corrugated plates Super Cor* (in Pol-

- ish), Scientific Papers of Silesian Polytechnic, Building Engineering Series, 3rd Conference of PhD Students of Building Engineering Faculties, Gliwice–Wisła, 2002, 65–74.
- [8] Bęben D., Mańko Z.: *Tests of a road bridge made from steel corrugated plates Super Cor type* (in Polish), XLVIII Scientific Conference of Polish Academy of Sciences, Civil Engineering Committee and Polish Association of Construction Engineers and Technicians Scientific Committee, Krynica, 2002, Scientific and Research Building Engineering Problems, Opole–Krynica, 2002, Vol. 4, 167–174.
- [9] PN-82/S-10052. *Bridge structures. Steel structures. Design.*
- [10] PN-85/S-10030. *Bridge structures. Loads.*
- [11] PN-89/S-10050. *Bridge structures. Steel structures. Requirements and tests.*
- [12] Bęben D.: *Dynamic tests of road bridge made from steel corrugated plates* (in Polish), Scientific Papers of Silesian Polytechnic, Building Engineering Series, 4th Conference of PhD Students of Building Engineering Faculties, Gliwice–Wisła, 2003, 79–86.
- [13] Bęben D., Mańko Z.: *Research of response behavior of steel road arch bridge*, 11th International Scientific Conference on Science, Education and Society, Zilina, Slovak Republic, 2003, section No. 1, 369–372.
- [14] Mańko Z., Bęben D.: *Acceptance tests of prototype arch road bridge made from steel plates* (in Polish), *Inżynieria i Budownictwo*, Warsaw, 2002, Vol. LVIII, No. 9, 506–509.
- [15] Madaj A., Janusz L., Vaslestad J.: *Tests of brick culvert reinforced with steel structure made from corrugated plates* (in Polish), 11th Seminar on Modern Methods of Reinforcing and Retrofitting Bridges, Poznań–Kiekrz, 2001, 98–105.
- [16] Madaj A., Bednarek B., Janusz L., Vaslestad J.: *Tests of steel corrugated-plate structure used to reinforce steel culvert, carried out after one year of service* (in Polish), 13th Seminar on Modern Methods of Reinforcing and Retrofitting Bridges, Poznań–Kiekrz, 2003, 173–181.
- [17] McCavour T.C., Byrne P.M., Morrison T.D.: *Long span reinforced steel box culverts*, Transport Research Board Committee A2CO6. Culverts and Hydraulic Structures, Washington, D.C, 1998.
- [18] Vaslestad J.: *Long-span corrugated steel structure at Dover. Observations of earth pressure, stresses, deformations and temperature* (in Norwegian), Internal Report, No. 1134, Norwegian Road Research Laboratory, Oslo, 1987.
- [19] Vaslestad J.: *Long-term behavior of flexible large-span culverts*, Transportation Research Record, 1990, No. 123, Transportation Research Board, Washington D.C., 14–24.
- [20] HSDHCP.: *Handbook of Steel Drainage & Highway Construction Products*, American Iron and Steel Institute, fifth edition, Chicago, 1994.
- [21] AASHTO.: *Standard Specifications for Highway Bridges*, American Association of State Highway and Transportation Officials, New York, 2002.
- [22] Mańko Z., Bęben D.: *Tests on soil-steel bridge structure made from corrugated plates located in Polanica Zdrój*, Scientific-Research Centre for Development of Bridge Industry MOSTAR, report no. 23/2002, Wrocław, December 2001.
- [23] Mańko Z., Bęben D.: *The study of road bridge structure made from Super Cor type SC-56B steel corrugated plates under static and dynamic load in Gimån* (Sweden), Scientific-Research Centre for Development of Bridge Industry MOSTAR, Wrocław, October 2002.
- [24] Bednarek B., Janusz L., Mielnik L., Wysokowski A.: *Tests of natural-size steel corrugated-sheet box culvert. Comparative analysis of stresses in structure wall during filling*

it with soil and under static load (in Polish), 2nd Scientific-Technical Symposium on Bridge Tests and Diagnostics, Opole, 2003, 23–29.

- [25] Wysokowski A., Korusiewicz L., Kunecki B.: *Report on tests carried out on MultiPlate culverts and DV/AROT OPTIMA pipes. Part I: MultiPlate (TW 26999/W-374)*, Roads and Bridges Institute, Żmigród–Węglewo, 1999.

Badania mostu łukowego wykonanego ze stalowych blach falistych

Prezentowano sposób przetestowania nowego mostu drogowego wykonanego ze stalowych blach falistych typu *Super Cor* i zaprezentowano wyniki otrzymane trzech etapach budowy. W I etapie badań obciążenie stanowiła zasyпка gruntowa, a w II i III etapie – dwa pojazdy balastujące. Badany most o podatnej konstrukcji „skrzynkowej” jest położony nad rzeką Bystrzycą Dusznicką w Polanicy Zdroju. Rozpiętość teoretyczna przęsła nowego mostu wynosi 12,270 m, a jego światło pionowe – 3,85 m. Przęsło stalowe jest posadowione na dwóch żelbetonowych ławach fundamentowych. Maksymalne wartości pomierzonych przemieszczeń i odkształceń jednostkowych (naprężeń normalnych) w wybranych punktach i przekrojach stalowej konstrukcji powłoki były stosunkowo małe i wywołane tym samym znanym obciążeniem. Wnioski z przeprowadzonych badań mogą być przydatne w określeniu współpracy powłoki stalowej z gruntem zasypany. W Polsce i na świecie coraz częściej stosuje się tego typu konstrukcje stalowo-gruntowe do budowy małych i średnich mostów położonych w ciągu linii drogowych i kolejowych, dlatego wnioski z badań przeprowadzonych w trzech etapach budowy, można uogólnić na całą klasę podobnych rozwiązań konstrukcyjnych.

Modelling the surfaces of grinding wheels whose structure is zonally diversified

K. NADOLNY, B. BAŁASZ

Technical University of Koszalin, ul. Raławicka 15-17, 75-620 Koszalin

This paper presents modelling the surfaces of grinding wheels whose structure is zonally diversified. New grinding wheels were designed in order to conduct a single-pass internal grinding process. It is possible to obtain a final machining result in one pass of grinding tool due to the application of alundum grains in rough grinding zone and microcrystalline aluminium oxide SG grains in finish grinding zone. A characteristic of a single-pass axial internal cylindrical grinding is presented. The paper deals with grinding tools of zonally diversified structure and the method of modelling their active surfaces. The method presented enables us to model single abrasive grains of different kinds which can be used for designing the model of active surface of grinding wheel. The model structure allows us to divide the tool active surface into the zones and to diversify the grain type, shape, size and arrangement in each zone. Additionally, this method makes it possible to modify the grinding wheel macrogeometry and to apply, for instance, a conic chamfer.

Keywords: single-pass internal grinding, grinding wheels of zonally diversified structure, modelling of active surface of grinding wheels

1. Introduction

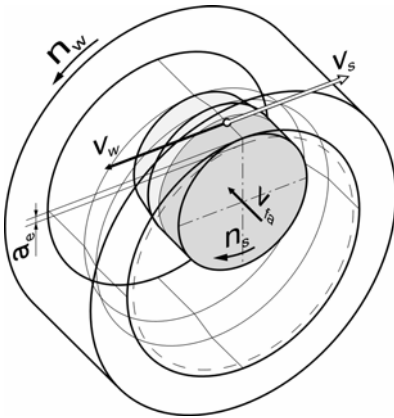
In modern metal industry, the shortening of a machining time along with maintaining high quality of machined surface is an urgent necessity. In internal grinding, one of the ways to increase its efficiency is the one-pass process [5, 6]. Examination of that process, which consists in modification of the structure of grinding wheels and the shape of active surface, is conducted at Technical University of Koszalin.

One of the new methods which assists in investigation of machining process modifications is computer modelling. It allows us to reduce the costs of designing new tools due to multicriterion optimization and discarding an incorrect or not beneficial conception without experimental investigations.

In the case under discussion, some significant modifications apply to the grinding wheel, therefore the possibility of precise modelling an active surface of new tools is very important. The model of zonally diversified structure of grinding wheels allows a division of active surface into zones, modifications of grain type, shape and size in each of zones, defining the porosity and macrogeometry of grinding wheel (conic chamfer). The model was developed on the basis of real grinding wheels in order to optimize their structure in such a way as to obtain the results and conditions of single-pass axial internal cylindrical grinding.

2. Single-pass axial internal cylindrical grinding process

Application of grinding wheel with conic chamfer to axial internal cylindrical grinding process enables us to achieve a final result of machining in one pass. In such a type of grinding wheel, rough grinding and finish grinding take place in two zones. In the first zone, a substantial reduction of material takes place (the angle χ of rough grinding is matched to include all machining allowance), in the second zone, a sufficiently high quality of grinding surface is assured [3, 4] (Figure 1).



- a_e – Working engagement
- n_s – Grinding wheel rotational frequency
- n_w – Workpiece rotational frequency
- v_{fa} – Axial table feed speed
- v_s – Grinding wheel peripheral speed
- v_w – Workpiece peripheral speed

Fig. 1. Scheme of single-pass internal cylindrical grinding process with zonally diversified structure of grinding wheel with conic chamfer

In axial cylindrical internal grinding process with grinding wheel whose conic zone is fitted for rough grinding, the value of working engagement a_e is not constant along the width of a grinding wheel. Variations in effective working engagement $a_{e\,eff}$ allow separation of four areas of variable load of grinding wheel (see Figure 2). In the first zone, an increase in load of grinding wheel occurs up to its constant value in the area II.

In zone II, the load value can be determined by the rate of material removal per unit active width of grinding wheel defined as follows [5, 6]:

$$Q'_{w\,eff} = \pi \cdot d_w \cdot n_w \cdot a_{e\,eff} \quad [\text{mm}^3/\text{mm} \cdot \text{s}]. \quad (1)$$

In the zone III, a decrease in the load of grinding wheel analogous to its increase in the area I occurs. However, in this zone also finish grinding as well as removal of machining allowance take place. In the area IV, sparking out occurs, because theoretically the process of material removal does not take place. However, due to the fact that elastic strain has been caused by grinding forces between the workpiece and spindle of grinding tool, also in this section decrement of machining material may occur [5].

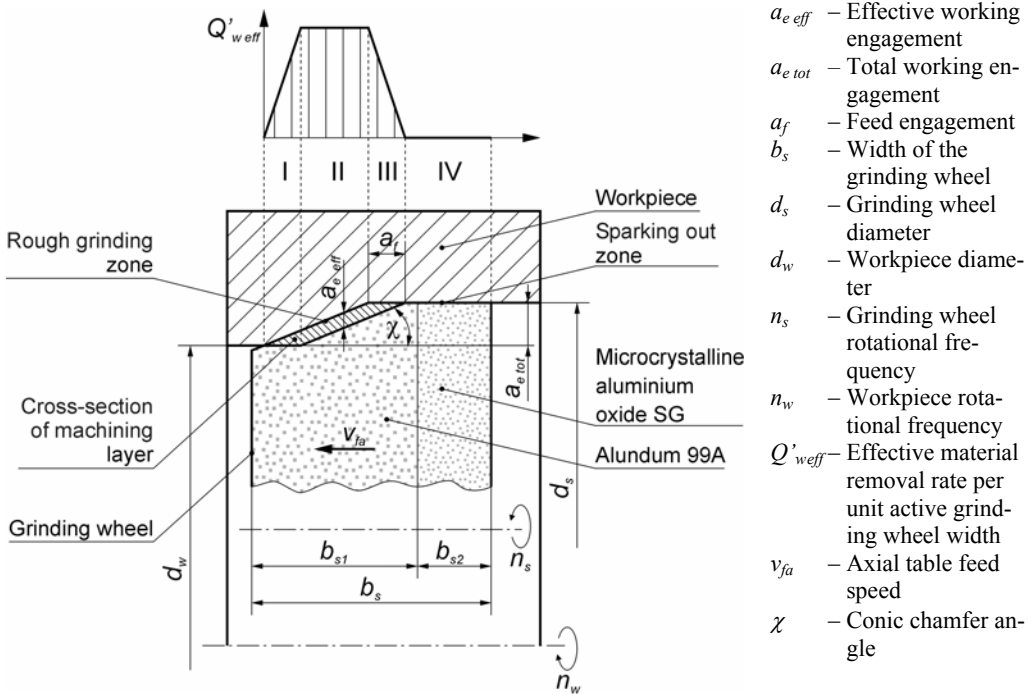


Fig. 2. Variable load areas of zonally diversified structure of grinding wheel with conic chamfer in axial internal cylindrical grinding

In the first three zones (rough grinding), we aim first of all to remove a specified layer of material from a workpiece. In the zone IV (finishing grinding and sparking out), our main aim is to generate very high quality of surface and to minimize roundness deviation by multiple grinding of workpiece surface [5].

3. Vitrified bonded (grinding) wheels of zonally diversified structure

Grinding wheels with different grain types in the zones of rough and finish grinding are subjected to modelling. Grinding tool of such type was designed at Technical University of Koszalin on the basis of glass-crystalline bond (Figure 3).

An overall grinding wheel width b_s equals 20 mm and its diameter d_s is 35 mm. A rough grinding zone ($b_{s1} = 14$ mm) was built of alundum 99A grains of granularity 60. In finish grinding zone ($b_{s2} = 6$ mm), we can find microcrystalline aluminium oxide SG grains of granularity 80. In rough grinding zone, there is a conic chamfer whose angle and length were matched to include all working allowance.

Experimental investigations with this type of grinding wheels showed the possibility of conducting single-pass internal grinding with working engagement of 0.15 mm. This parameter allow us to determine the conic chamfer angle $\chi = 1^\circ$.

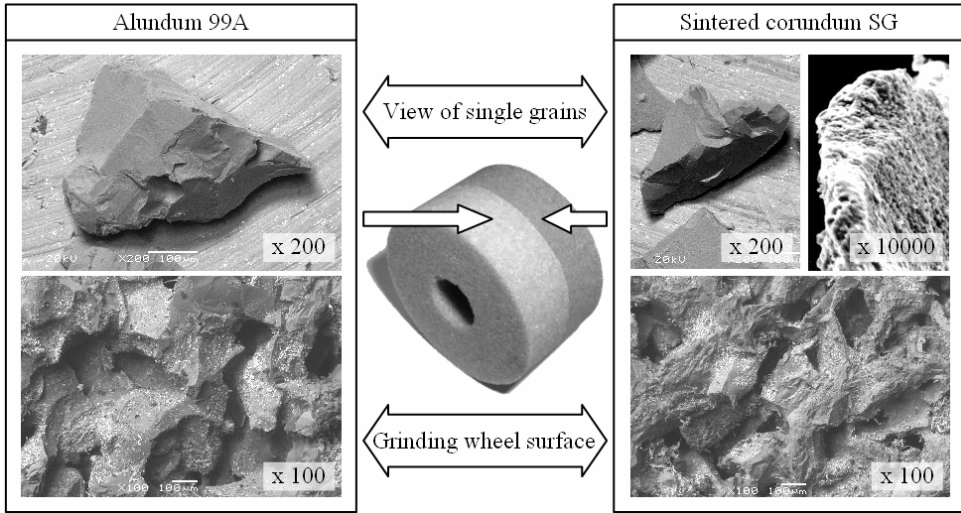


Fig. 3. Zonally diversified structure of grinding wheel of alundum 99A and microcrystalline aluminium oxide SG grains

Combining in one grinding wheel both alundum and SG grains enables intensive machine cutting by large monocrystals and simultaneously smoothing and sparking out the surface roughness by microcrystalline grains.

4. Modelling of abrasive grains

In the simulation method presented, we assume that in grinding process, the abrasive grains which protrude from the grinding wheel surface are of a special importance. The most important are their shapes and the sizes of protruding parts, because only those parts of grains are in contact with workpiece.

The surfaces of grains are described by the function whose components determine the shape of grain $f_{\text{shape}}(x, y)$ and its microtopography $f_{\text{mtp}}(x, y)$. The elements of function are additive or multiplicative connecting (2):

$$Z_s(x, y) = f_{\text{shape}}(x, y) + f_{\text{mtp}}(x, y). \quad (2)$$

Numerical notation of the grain shape is a real number matrix Z_s (3) whose dimensions are defined by assumption concerning the size of a grain subjected to modelling:

$$Z_s(x, y) = \begin{bmatrix} z_{11} & z_{12} & \dots & z_{1n} \\ z_{21} & z_{22} & \dots & z_{2n} \\ \dots & \dots & \dots & \dots \\ z_{m1} & z_{m2} & \dots & z_{mn} \end{bmatrix}, \quad (3)$$

where $z_{ij} = f_{\text{shape}}(x_i, y_j) + f_{\text{mpt}}(x_i, y_j)$.

Numerical notation of the grain surface topography enables modifications of grain shape during simulation process. Changes are generated by grain wear in grinding process and by grinding wheel honing process.

The models of grain surface are added to elementary strip model $[x_s, y_s]$ of grinding wheel surface (Figure 4). That strip is situated along the generating line of grinding wheel and its width has an influence on the modelling tool characteristic. Position of grain on grinding wheel surface is random. To assure a proper arrangement of grains on the grinding wheel surface, modelling takes into account the values of indexes that determine grain location l_x, l_y in accordance with the random numbers' distribution that concerns the grains spacing on the surface of a real grinding wheel.

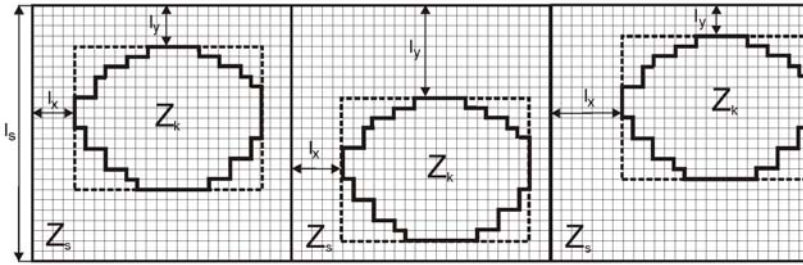


Fig. 4. Scheme of grains' location on base surface

An example of surfaces' ordinate diagram of abrasive grain model is presented in Figure 5.

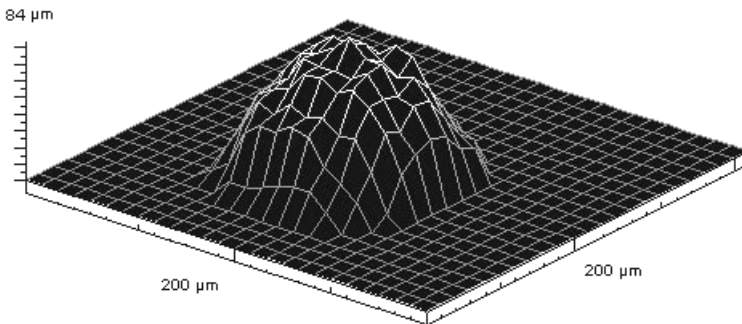
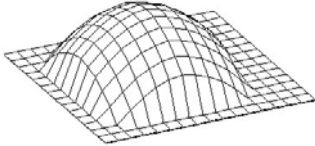
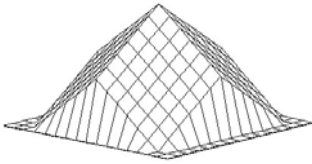
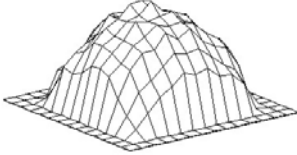
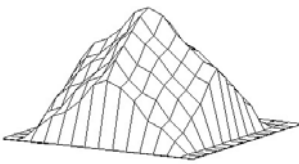
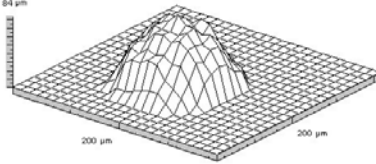
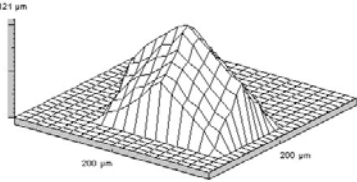
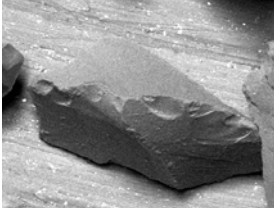


Fig. 5. Example of abrasive grain model

The modelling method described enables us to create the models of abrasive grains of different kinds. This is possible due to a suitable choice of function which describes the grain shape and proper values of its coefficients. Stages of creating models of alundum and SG grains are presented in the Table.

Table. Stages of creating models of alundum and SG grains

	Alundum	SG
Function of shape	$f_{\text{shape}}(x, y) = ((x^2 + y^2) / w_k + a x + by) - \text{Max}((x^2 + y^2) / w_k + a x + by)$	$f_{\text{shape}}(x, y) = ((x + y) / w_k) - \text{Max}((x + y) / w_k)$
		
	↓	↓
+ function of microtopography	$f_{\text{mp}}(x, y) = \text{random}(\text{real}, \{a_i, b_i\})$	$f_{\text{mp}}(x, y) = \text{random}(\text{real}, \{a_i, b_i\})$
		
	↓	↓
+ function of grain location	$f_{\text{location}}(x, y) = \text{random}(\text{integer}, \{0; l_{\text{max}}\})$	$f_{\text{location}}(x, y) = \text{random}(\text{integer}, \{0; l_{\text{max}}\})$
Grain model		
Real grain		

5. Modelling of active surface of grinding wheel

The surface of grinding wheel is modelled by assembling basic cells with elementary strips of grinding tool surface w_{sc} . In order to make a random manner of grains spacing on the whole surface of grinding wheel more efficient, each row of grains is additionally shift along next row by the random value p_{wsc} (Figure 6).

Model of grinding wheel surface is recorded in real number table, and its size is based on the grinding tool parameters. Model of grinding wheel topography includes not only abrasive grains, but also models of bond and pore structure.

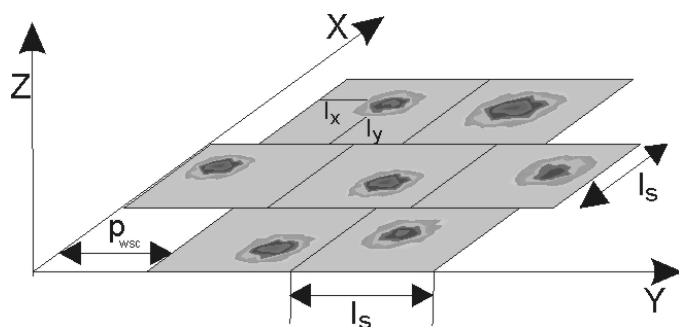


Fig. 6. Arrangement of grains on grinding wheel surface

The method described enables us to generate an active surface of grinding wheel with specified microgeometry for rough (Figure 7a) and finish grinding zones (Figure 7b).

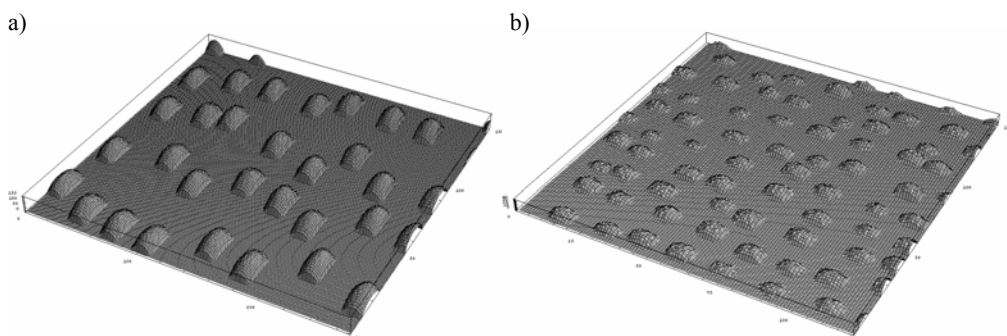


Fig. 7. Modelling surface of rough (a) and finish (b) grinding zones of zonally diversified structure of grinding wheel

Conic chamfer of grinding wheel is implemented in grinding simulation process by determining an angular orientation of adequate element of modelling surface.

6. Conclusion

In the design of new grinding wheels, simulated methods which allow verification of innovations without building real tools are of a special importance. Our method of modelling an active surface of grinding wheel enables numerous modifications to grinding tool structure (e.g. separating the zones of different kinds, shapes and sizes of abrasive grains). The method of modelling an active surface of zonally diversified structure of grinding wheel being designed to single-pass internal grinding has wide application.

References

- [1] Klocke F., Hegener G., Deacu L.: *Hochleistungs-Aussenrund-Formschleifen. Innovatives Fertigungsverfahren vereint hohe Flexibilität und Produktivität*, ZWF, 1996, 91, 4, 164–167.
- [2] Nadolny K., Plichta J.: *Badania procesu szlifowania otworów ściernicą o strefowo zróżnicowanej charakterystyce*, Materiały XXVI Naukowej Szkoły Obróbki Ściernej, Łódź, 2003, 153–158.
- [3] Niżankowski C., Przybylski L.: *Materiały i narzędzia ścierne – trendy rozwoju w XXI wieku*, Materiały XXV Jubileuszowej Naukowej Szkoły Obróbki Ściernej, Wrocław, 2002, 17–32.
- [4] Oczos K.E.: *Charakterystyka trendów rozwojowych szlifowania ściernicowego*, Materiały XXIII Naukowej Szkoły Obróbki Ściernej, Rzeszów, 2000, 13–62.
- [5] Oczos K.E.: *Rozwój innowacyjnych technologii ubytkowego kształtowania materiałów*, Cz. II. *Szlifowanie*, Mechanik, 2002, 75, 10, 627–637.
- [6] Weinert K., Finke M.: *Innenrund-längsschleifen von Futterteilen – Bohrungen in einem Überschleiff fertig schleifen*, Materiały XXIV Naukowej Szkoły Obróbki Ściernej, Łopuszna, 2001, 37–44.

Modelowanie powierzchni narzędzi ściernych o strefowo zróżnicowanej budowie

Przedstawiono metodę modelowania powierzchni ściernic o strefowo zróżnicowanej budowie. Nowe ściernice opracowano, aby prowadzić jednoprzęściowy proces szlifowania otworów. Zastosowanie ziaren elektrokorundu szlachetnego w strefie szlifowania zgrubnego oraz mikrokryształicznego tlenku glinu SG w strefie szlifowania wykańczającego umożliwia uzyskanie ostatecznego rezultatu obróbkowego w jednym przejściu narzędzia. W pracy podano charakterystykę jednoprzęściowego osiowego szlifowania otworów i szczegółowo opisano narzędzia ścierne o strefowo zróżnicowanej budowie, a także metodę modelowania czynnej powierzchni ściernic tego typu. Zaprezentowana metoda umożliwia modelowanie pojedynczych ziaren ściernych różnych gatunków i tworzenie z nich modelu czynnej powierzchni. Struktura modelu pozwala podzielić czynną powierzchnię narzędzia na strefy i zróżnicować rodzaj, kształt, wielkość i rozmieszczenie ziaren w każdej z nich. Dodatkowo możliwa jest modyfikacja makrogeometrii ściernicy i zastosowanie np. nakroju stożkowego.

Load rate of the circumferential sector of soil-steel bridge structures

CZESŁAW MACHELSKI, GRZEGORZ ANTONISZYN

Wrocław University of Technology, Wybrzeże Wyspiańskiego 27, 50-370 Wrocław

In order to calculate the parameters soil-steel structure, a special software based on a 2D model is used. The concentrated forces of a bridge roadway generated by vehicles are being related in this model to a selected sector based on Boussinesq's theory. This theory, however, does not fully confirm the work effect (internal forces) of soil-steel structures as flexible structures cooperating with soil in carrying external loads. The effectiveness of this theory was estimated according to the 3D model built out of FEM elements. For this reason a comparison algorithm was constructed based on the influence function of internal forces for a selected strip of steel shell. The analysis showed the influence of general parameters of the bridge (width, span) on internal forces being neglected in developing the guidelines for such bridges. The parametric analysis given in this paper refers to a completed construction of a classical soil-steel bridge built in Szczytna. As variable characteristics of the object we assume: thickness of backfill, shell span, haunch radius, kind of steel corrugation as well as sheet thickness of the shell types applied. The analysis proved that some of them essentially influence the system of internal forces. The results of analysis of geometric parameters of the steel shell indicate the possibility (theoretical) of such a modification of the structures that allows reduction in steel usage.

Keywords: *soil-steel bridges, moving loads, shell effort*

1. Introduction

The soil-steel bridges are composed of the following main structural elements: an elastic shell of corrugated sheet, most often a steel one, soil backfill surrounding the shell and cooperating with it and road surface (Figure 1). Such structures are designed and made in a way that ensures an advantageous cooperation of a shell with two other elements considered in a bridge construction as non-structural ones [1].

For soil-steel structure calculations, there are used special computer programs based on a flat 2D model built out of FEM elements (Figure 2a). The model well represents the systems of internal forces generated as a result of constant loads (dead weight of bridge). In the case of live loads (generated by vehicles), concentrated forces from the roadway surface are reduced to the analyzed shell strip (model 2D) using Boussinesq's theory. Such a procedure is also used in bridge designing [2]. The spatial 3D model of a structure (Figure 2b) enables more reliable representation of internal forces in the shell from local loads. However, this model requires a big number of elements and increased cost of labour for discretisation of the object [3]. In such calculations, general FEM systems are normally used.

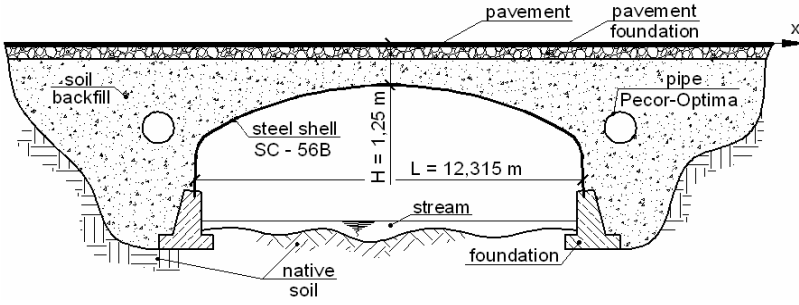


Fig. 1. Longitudinal section of the soil-steel bridge in Szczytna

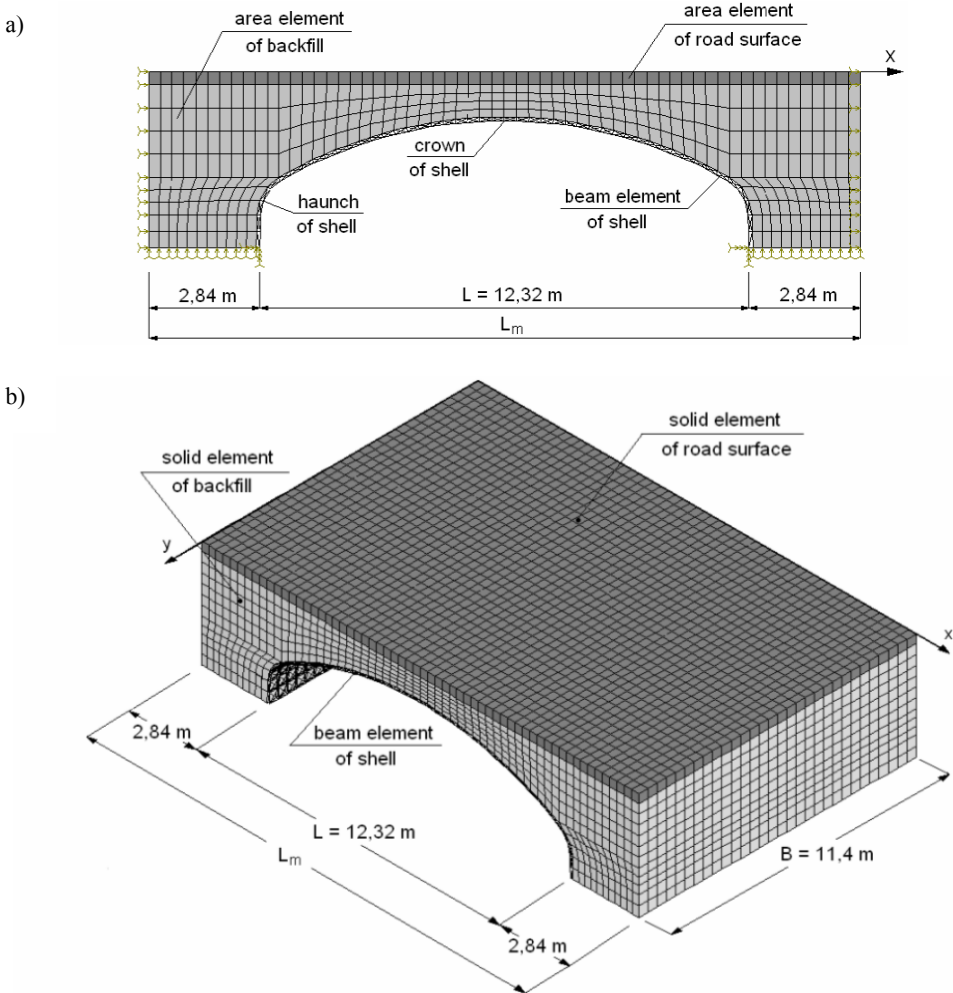


Fig. 2. Numerical models of the bridge: a) 2D model, b) 3D model

The 3D model used here has been made based on numerical testing of many models of the shell surrounded by soil and on the results of tests on real objects [4, 5]. In this paper, we considered two models (Figure 2), where [4]:

- the corrugated sheet was simulated as beam elements,
- the soil backfill was simulated as 2D or 3D isotropic continuum,
- the road surface was simulated as surface or volumetric isotropic elements,
- the interface was simulated by using 1D elastic elements.

In the case of both models, a numerical discretisation of bridge models was carried out based on isotropic volume and area elements that allowed us to model the road surface whose material characteristics were as follows: $E = 350$ MPa and $\nu = 0.2$. The soil backfill surrounding structural corrugated plates was also modelled based on isotropic volume and area elements of the following material characteristics: $E = 155$ MPa and $\nu = 0.2$ [11]. Geometrical characteristics of the corrugated plate of the SC 380·140·7 type, i.e. the plate depth $t = 7$ mm, the corrugation length $a = 380$ mm and the corrugation height $f = 140$ mm, are taken from the design guidelines laid down by the Corrugated Steel Pipe Institute & American Iron and Steel Institute [15]. Material characteristics of steel plates of shell were as follows: $E = 205$ GPa and $\nu = 0.3$ [4, 11].

The numerical analysis was carried out by using the *COSMOS/M* system. The examples of numerical analysis were based on geometric parameters of the bridge at Szczytna town as shown in Figure 1 [6, 7].

2. Load rate of 2D model

2.1. Boussinesq's model

In classical design calculations [2], there is considered a flat 2D model of the construction (a shaded outline in Figure 3). The moving loads from the roadway being laid in the plane xy are reduced to the line $y = y_o$, which is a top edge of 2D model. The reduced load is obtained from the condition of a normal stress σ_z (the pressure onto the top surface of the shell) at the point A .

In the case of the load q distributed uniformly by along the line parallel to the y -axis, as in Figure 3, the pressure exerted onto the shell along the line passing through the point A is uniform as well:

$$\sigma_z = \frac{2p}{\pi} \frac{H^3}{s_q^4}. \quad (1)$$

In the case of the concentrated load imposed at the point $P(x_p, y_p)$, the pressure exerted onto the shell at the point $A(x_o, y_o)$ equals:

calculated on the basis of q , but of the result equivalent to the force P as in the light of the criterion adopted in (3) they are equivalent. The value P_a depends on the constant parameters (P , H , a) and the variables in which the position of the points P and A is taken into account. The function

$$\mu_B(x, y) = \frac{3a}{4} \frac{[H^2 + (x_o - x_p)^2]^2}{[H^2 + (x_o - x_p)^2 + (y_o - y_p)^2]^{\frac{5}{2}}} \quad (7)$$

adopted in (6) can be treated as the influence surface of the P_a caused by vertical force $P(x_p, y_p)$ acting on the roadway surface and being related to the analyzed point $A(x_o, y_o)$ of the shell strip.

If the force acts over the analyzed point $P(x_o, y_o)$, Equation (7) simplifies to the dimensionless parameter

$$\mu = \frac{3}{4} \frac{a}{H}. \quad (8)$$

2.2. Numerical model

The influence surface of internal force S (of the bending moment, of the axial force or of the normal stress) at the analyzed point $A(x_o, y_o)$ of the shell obtained using 3D model can be presented in the form of two profiles given in Figure 4:

- longitudinal profile representing the force moving along the x -axis ($y_p = y_o$),
- transverse profile representing the force moving along the y -axis ($x_p = x_o$).

According to the definition of the influence surface, the internal force S induced by an optionally applied concentrated force P can be defined as follows:

$$S(x_o, y_o) = \eta(x_o, x_p, y_o, y_p) \cdot P. \quad (9)$$

In a specific case, when the force P is applied directly over the point $A(x_o, y_o)$, the following equation should be used:

$$S(x_o, y_o) = \eta(x_o, y_o) \cdot P. \quad (10)$$

If 2D model is used, the internal force $S(x_n)$ generated by a concentrated load P is expressed by the following equation:

$$S(x_o) = \xi(x_o, x_p) \cdot P_a, \quad (11)$$

where P_a stands for the load that is caused by the concentrated force $P(x_p, y_p)$ and that acts on the structure sector of the width a . In a specific case, when the force P is applied directly over the point $A(x_o, y_o)$ being analyzed, we obtain:

$$S(x_o) = \xi(x_o) \cdot P_a . \tag{12}$$

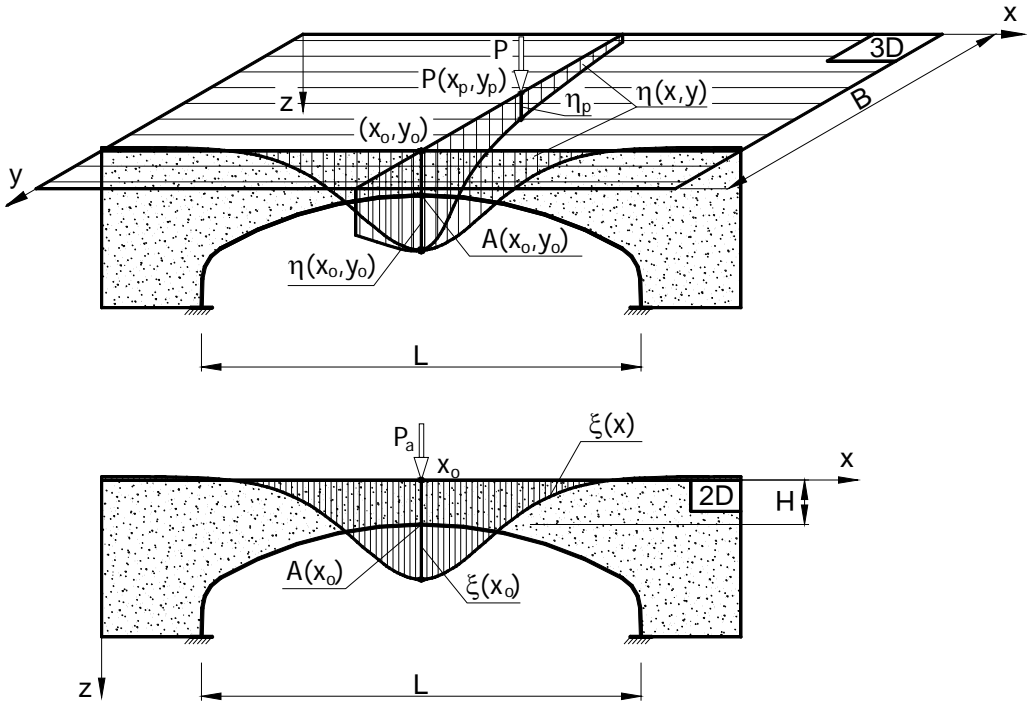


Fig. 4. Sections of influence surface and influence line of internal force S

Comparing (10) with (12) we arrive at:

$$C = \frac{P_a}{P} = \frac{\eta(x_o, y_o)}{\xi(x_o)} . \tag{13}$$

Taking account of the above, we can calculate the load P_a of the shell strip based on the influence function of an internal force

$$P_a = \eta(x, y) \frac{1}{C} \cdot P = \mu_{\text{num}}(x, y) \cdot P . \tag{14}$$

The function $\mu(x, y)$ is the influence surface P_a related to the analyzed point $A(x_o, y_o)$ of the shell strip and generated by vertical forces on the roadway surface $P(x_p, y_p)$, compare Equation (7).

Figure 5 shows some examples of transverse and longitudinal profiles of the influence surface of normal stress for the strip $y_o = 3B/4$ and the point lying in the crown of the shell ($x_o = L/2$). Geometrical parameters of this bridge were the same as these of the bridge in Szczytna [6, 7] (Figure 1), where the width B of the road crown was 11.40 m. The diagrams also show how the soil backfill thickness H influences the value of the ordinates of the stress influence surface.

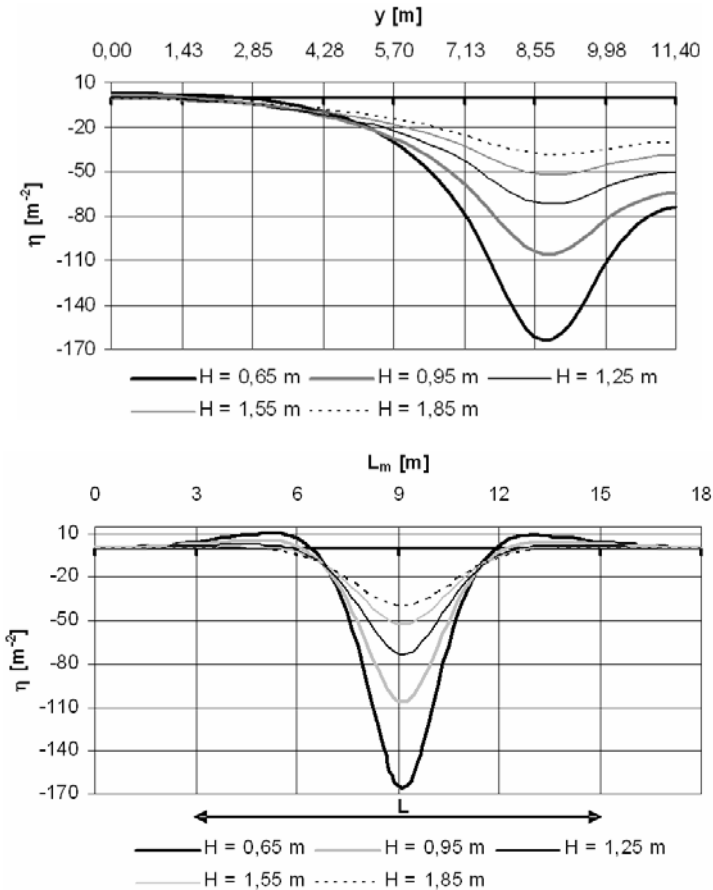


Fig. 5. Transverse and longitudinal sections of the influence surface of normal stresses depending on the depth of the cover

Based on the function $\eta(x, y)$ we can see that along with an increase in the thickness H the value of η decreases. This provides evidence of a diminishing influence of

local loads (concentrated) on the shell strain. If the cover is thick enough, the concentrated loads are evenly distributed along the entire width of the shell. An advantageous influence of an increased thickness of the cover is reduced by the stresses generated by the soil backfill dead weight.

2.3. Comparative analysis

Equations (7) and (14) enable the comparison of the models of soil-steel structures analyzed above. The values μ_{num} obtained from 3D model and Equation (14) as well as the results obtained from (7) and denoted by μ_B can be compared as the physical sense of these values is the same. We obtained both values based on totally different assumptions.

Figure 6 presents μ versus the soil backfill thickness H and the place where the concentrated force P was applied to the shell strip of the width $a = 0.38$ m (the length of the wave). The strip $y_o = 3B/4$ and the point in the shell crown were analyzed. We assumed three places where the concentrated force was applied: over the point ($y_p = y_o$) being analyzed and two cases where the force was applied at the same distance from the point analyzed:

$$\Delta y = |y_o - y_p| = \frac{B}{8}. \quad (15)$$

The values of forces P_a caused by the concentrated forces in the 2D model can be calculated based on the curves μ charts given in Figure 6. For example, at $H = 1.25$ m the loaded sector over the point A (the top curve) is subjected to the force $0.20P$ (Boussinesq's) and $0.07P$ (numerical result). In the case of the indirect load (the bottom curves), at $y_p = 5B/8$ we obtain respectively $0.046P$ and $0.053P$ and at $y_p = 7B/8$ we obtain $0.046P$ and $0.063P$.

The results given in Figure 6 indicate that the influence of the soil backfill thickness on the load distribution in the soil-steel structure is considerably greater than can be expected based on force distribution itself in the soil medium according to Boussinesq. We found especially big differences in the results for these structures when H reached a minimum value. However, a small thickness of the soil backfill seems to be advantageous because in such a case a space under the bridge is quite large [5]. The curves in Figure 6 prove that the sign of Δy (Equation (15)) is also important.

In Figure 7, there are given the transverse profiles of the influence surface of normal stresses in the shell crown for some selected shell strips. The lay-out of the analyzed strips at cross sections of the bridge is defined by the equation:

$$y_o = B \frac{15 + 2i}{30} \quad \text{for } i = 0, 1, 2, \dots, 7. \quad (16)$$

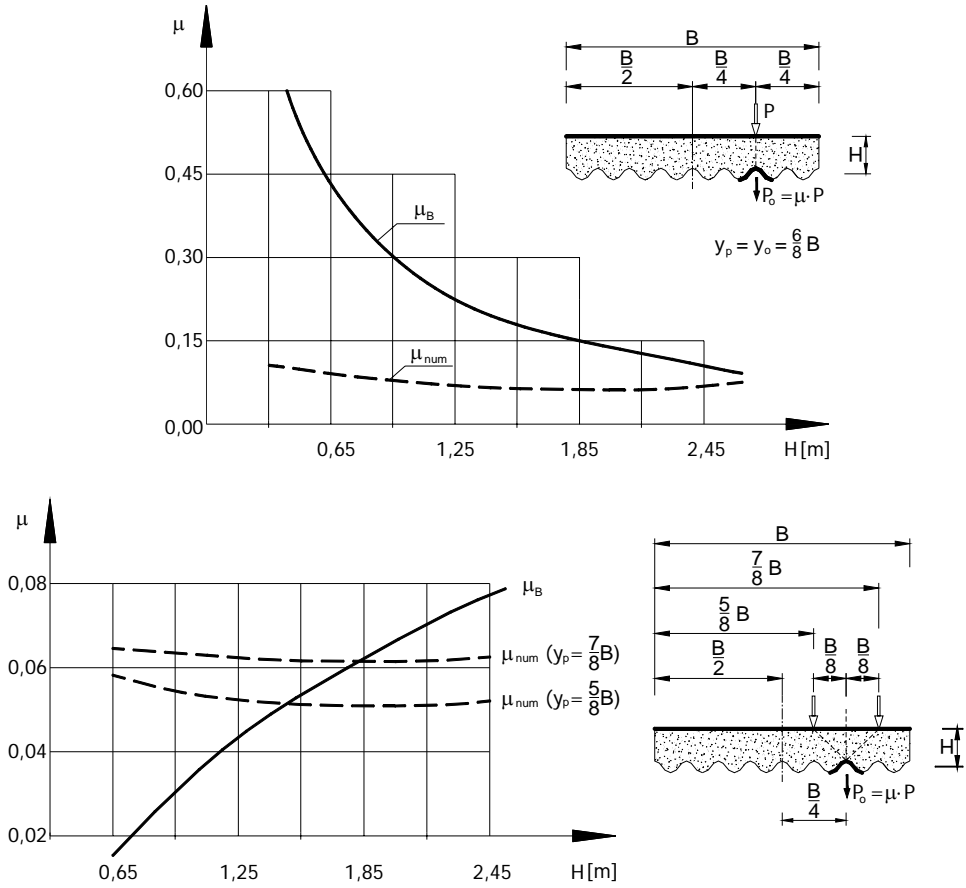


Fig. 6. The values of the coefficients μ_B and μ_{num} depending on the depth of the cover H

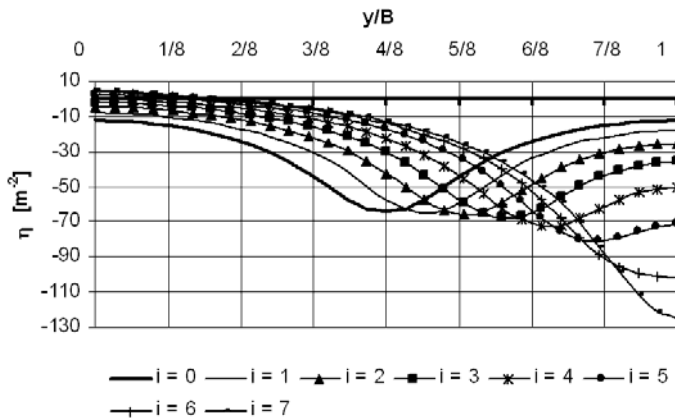


Fig. 7. Transverse cross sections of influence surface for selected strips of a shell

The lay-out of the curves presented in Figure 7 is such that extreme values of the ordinates are identical for the strips included in the following range:

$$\frac{B}{5} < y_o < \frac{4B}{5}, \quad (17)$$

where B is the width of the bridge structure. The extreme strips are normally overloaded because the values $\eta(y)$ for $y_o > 0.8B$ evidently increase. The embankments of bridge structures are paved so those parts of bridges are not exposed to concentrated loads caused by vehicle wheels. Considering the above we can conclude that circumferential strips of a shell which are underneath a roadway are stressed in the same way.

3. Influence lines of internal forces

The influence of geometrical parameters on internal forces in a shell was analyzed by using 2D model. The soil backfill thickness of 90 cm and the road surface thickness of 35 cm ($H = 1.25$ m) were assumed to be constant. The changes of geometrical parameters were related to the bridge built at Szczytna town (Figure 1). Two cross sections of the bridge were thoroughly analyzed: in the middle of the shell span and in the middle of the haunch. In these sections, the highest normal stress was measured on the top and bottom edges of the corrugated sheet. In this paper, there were analyzed the changes of geometrical parameters in the range given in the Table. In two cases, we did not analyze regular changes of parameters and we took the values that complied with standards of a real object, i.e. $L = 12.315$ m and the radius $R_n = 1.016$ m.

Table. Geometrical parameters of the bridge structure

Variable parameter of shell		Range of variability
L	span	8–20 m
R_n	haunch radius	0.5–3.0 m
geometry of sheet corrugation		MP 150·50, MP 200·55, SC 380·140, SC 400·150
t	sheet thickness SC 400·150	3–7 mm

The method used for static analysis was based on comparing the influence lines (2D model) of internal forces (S) drawn for characteristic points of shell strip [10, 11]. This allows an objective comparison of the changes in the parameters analyzed and additionally calculation of internal forces caused by live loads (e.g. true vehicles or imaginary vehicles meeting standards) optionally set along the roadway. In order to arrive at the influence function of internal forces S , the kinematic inputs were used [11, 12].

3.1. Shell span

In order to maintain the proportion of radial changes of the shell curvature together with the span change L_i , the model of the object was scaled as shown in the following equation:

$$s_i = \frac{L_i + 2}{L_i} \quad \text{for } i = 2, 3, \dots, 6, \quad (18)$$

but for $i = 1$ we have $s_1 = 8.00/12.315 = 0.6469$.

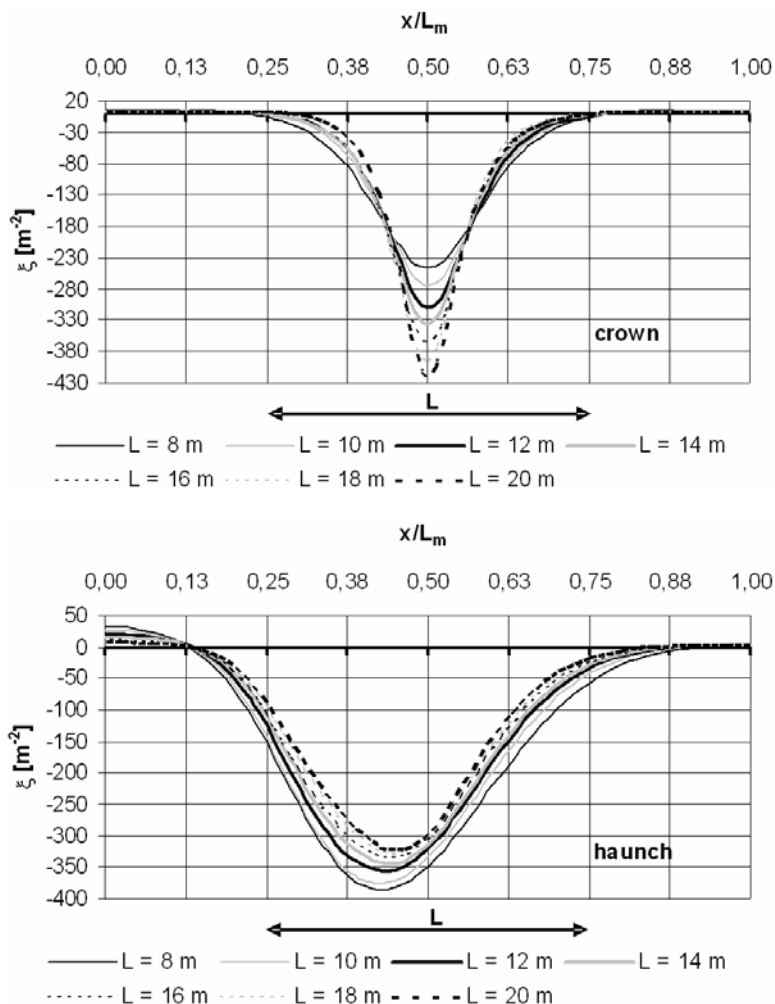


Fig. 8. Influence line of normal stresses depending on the span of the shell

The results given in Figure 8 show that normal stresses in the crown of shell ($x_o = L/2$) increase considerably due to increase in the shell span L . It should be stressed that this phenomenon is different from that observed during earlier numerical analyses of the soil-steel objects [10]. A different geometry of the object analyzed and a different kind of a shell sheet are responsible for above difference. Lower values of the ordinates of the influence lines of normal stresses for the shell haunch result from the model scaling. During scaling the radius of curvature of the haunch was increasing. This phenomenon is discussed in a detail in further part of this paper.

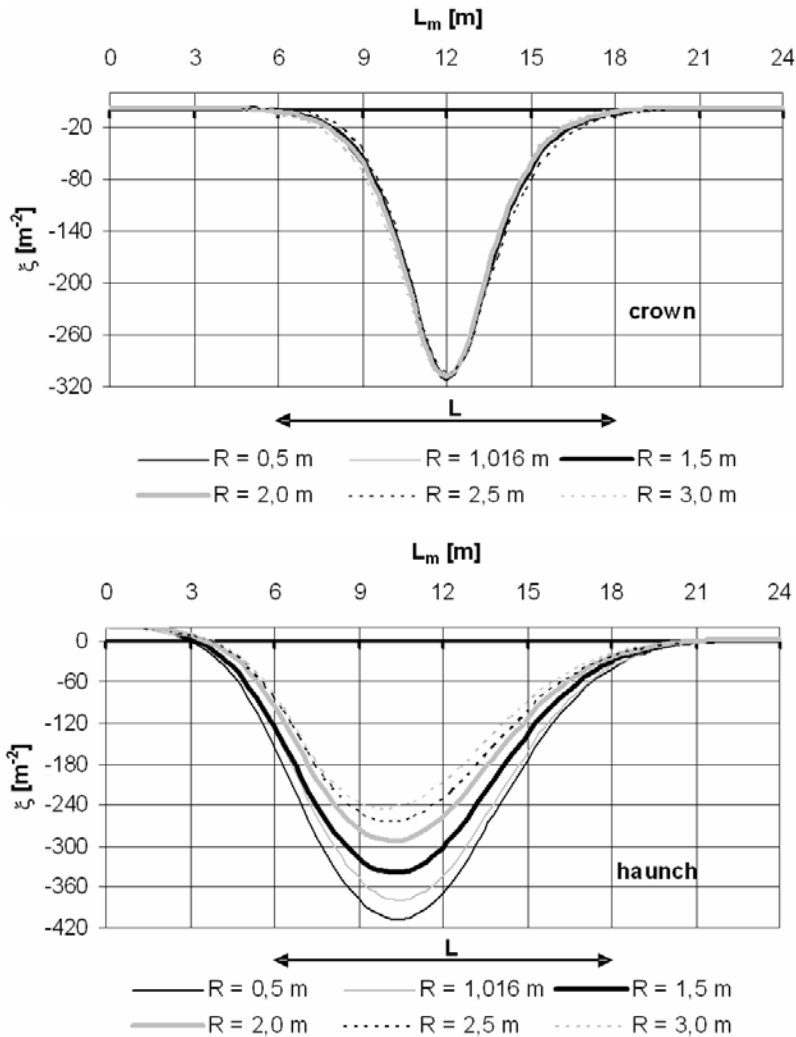


Fig. 9. Influence line of normal stresses depending on the change of haunch radius

3.2. The radius of shell haunch

The change of the radius of curvature R_n of haunch (Figure 9) affects the ordinates of influence lines of normal stress at the analyzed points of the shell in the crown and in the haunch in different way. The radius of curvature of shell haunch influences only slightly its effort in the middle of the span. The change in the shell geometry in the vicinity of the point analyzed influences greatly the effort in this section which manifests itself as a decrease influence lines' ordinates of normal stress and as an increase in the haunch radius. This phenomenon is in agreement with the theory of a ring compression [13, 14] and suggests that shell haunches of real structures have greater radius of curvature in order to reduce their effort. We can also conclude that in the analyzed points of the shell the bending moment affects most significantly the shell effort. This fact confirms the validity of using reinforcements in the form of additional corrugated sheets in these sections.

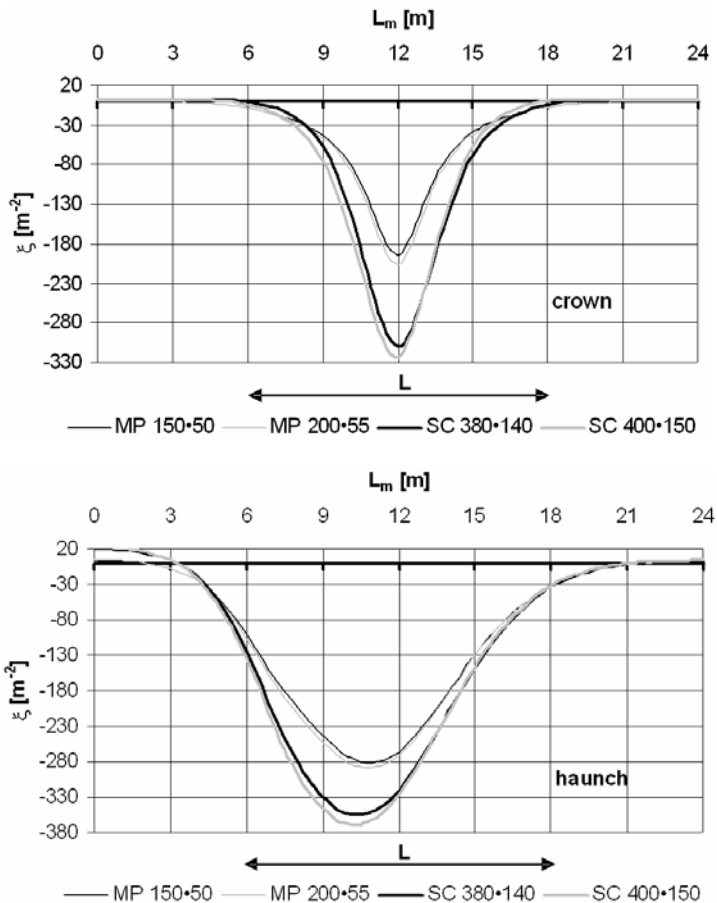


Fig. 10. Influence line of normal stresses depending on the kind of sheet corrugation

3.3. Geometry of the shell sheet corrugation

The influence of the geometry of the shell corrugation on its effort at a constant thickness of the sheet $t = 7$ mm is presented in Figure 10. The results obtained testify to the increase in the ordinate values of the influence lines with every change in the corrugation type of shell sheet whose height is considerable. This phenomenon is due to a substantial increase in the moment of inertia in respect of the cross-sectional area which in the case of the all analyzed kinds of sheets is similar (A ranges from 8.71 to 9.64 mm²/mm [15]). The greater height of the wave of the corrugated sheet causes that

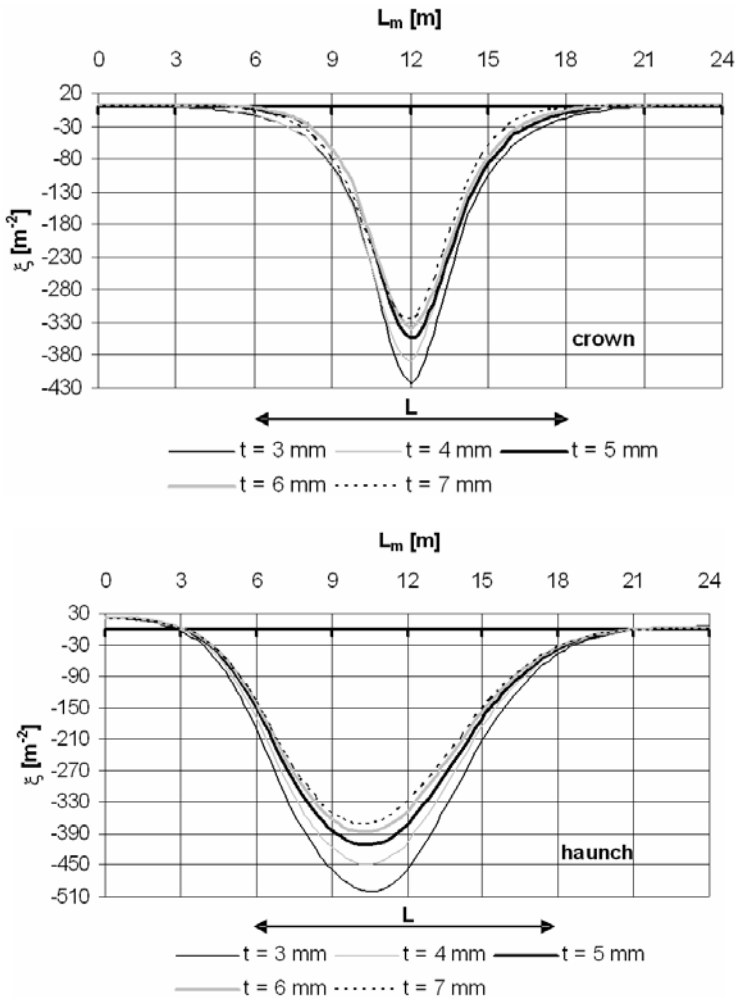


Fig. 11. Influence line of normal stresses depending on the change in the thickness of the shell SC 400·150

the more external loads the shell must take. In Figure 10, we can see clearly two separate groups of curves which allows us to divide the analyzed types of corrugation of the sheet into flexible (MP 150·50, MP 200·55) and stiff ones (SC 380·140 and SC 400·150).

3.4. Thickness of the shell sheet

The changes in the sheet thickness of the shells being considered earlier were analyzed. Due to very similar curves we present the results for the SC 400·150 shell only. Based on curves in Figure 10 we can conclude that in the shell made from a sheet of a smaller thickness, greater normal stresses are generated regardless of the kind of corrugation and the cross section analyzed (crown or haunch). A 50% increase in the sheet thickness results in a 15% decrease in stresses only, thus in the soil-steel structures the sheets of a minimum thickness are considered to be the best because of economical reasons. The above statement also leads to certain technological simplifications (rolling of thinner sheets).

3.5. Summary of analysis

In Figure 12, there are presented the changes in the pressure, defined by the $\mu(x, y)$ function (Equation (14)), exerted on the shell strip analyzed depending on such basic geometrical parameters of the bridge as: B, L, H . The curves $\mu(x_0, y_0)$ are plotted in the same figure with the central point where they assume the same values as those representing the bridge in Szczytna (Figure 1). The results obtained (Figure 12) are also valid for the sizes of the bottom view of B and L which according to Boussinesq's theory are not contained in Equation (5). These results and also the thickness of the soil backfill H influence considerably the values of μ .

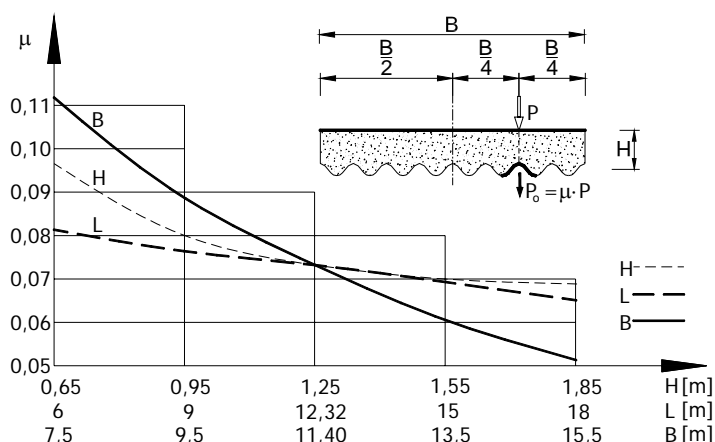


Fig. 12. Function $\mu(x, y)$ depending on basic shell parameters

4. Conclusions

Special software based on a 2D model is used for calculations made in designs of soil-steel structures. The concentrated forces generated by vehicles which load roadway of a bridge are brought, based on Boussinesq's theory to a selected section (2D model). In this paper, the validity of a commonly applied Boussinesq's theory was tested with respect to the FEM 3D and 2D models. For this reason, comparative algorithm was constructed based on the influence function of internal forces in a selected strip of a steel shell. The analysis carried out shows that we deal with considerable differences in the models, and especially in the objects with a minimum thickness of soil backfill. Also geometrical parameters of the object (width, span) are responsible for internal forces being neglected in designing guidelines for bridges. Taking account of the results this theory does not fully represent the work of soil-steel bridge systems (internal forces) as flexible structures cooperating with the soil in carrying external loads.

The parametric analysis presented here was related to the classical bridge of soil-steel structure built in the Szczytna town. The analysis results are given in the form of longitudinal profiles of the influence surface or influence lines of normal stresses i.e., in the form independent of the kind of load, because it is easier to process such a form. The following features: thickness of the cover, shell span, haunch radius, kind of the sheet corrugation and the sheet thickness in individual types of shells are considered to be the variables of the characteristics. Some of these features exert an essential influence on the system of internal forces. The results of the analysis of geometrical characteristics of the steel shell show that there is (theoretical) possibility of modifying the objects which leads to effective designing of shells and simultaneously a lower consumption of steel. They also show the directions of reasonable changes in shell forms of SUPER-COR type.

Based on the results of tests and many numerical analyses of soil-steel structures [3, 4, 5, 6, 10, 11, 13, 16, 17] we can conclude that these objects do not belong to the same group. We should not extend the results of tests and calculations to all kinds of such objects either. This can be done in the case of certain classes or groups of such objects only.

References

- [1] Machelski Cz., Antoniszyn G.: *Internal forces in soil-steel bridge structures* (in Polish), Drogi i Mosty, 2003, No. 2, pp. 33–57.
- [2] Pettersson L., Sundquist H.: *Design of Long Span Metal Culverts*, TRITA-BKN, Report 58, Brobyggnad 2000, English edition, 2003.
- [3] Girges Y., Abdel-Sayed G.: *Three-dimensional analysis of soil-steel bridges*, Canadian Journal of Civil Engineering, 1995, Vol. 22, pp. 1155–1163.

- [4] Antoniszyn G.: *Carrying capacity of soil-steel bridges under live loads on the basis of in situ research and numerical analysis* (in Polish), Zeszyty Naukowe Politechniki Śląskiej, seria: Budownictwo, z. 102, No. 1644, Gliwice, 2004, pp. 51–58.
- [5] Machelski Cz., Antoniszyn G.: *Investigation of soil-steel culverts of small structural height* (in Polish), Inżynieria i Budownictwo, 2004, No. 4, pp. 91–119.
- [6] Bęben D., Mańko Z.: *Research of road bridge made of steel corrugated plates of Super Cor SC-56B type under statical load* (in Polish), Diagnosis and Test of Bridges – Symposium, Opole, 4th – 6th Apr, 2001, pp. 27–70.
- [7] Krajnik D., Michalski J.B.: *First Canadian bridges in Europe* (in Polish), Inżynieria i Budownictwo, 2002, No. 3–4, pp. 159–165.
- [8] Wiłun Z.: *Zarys geotechniki*, WKŁ, Warszawa, 1987.
- [9] Webb M.C.: *Improved Design and Construction of Large-Span Culverts*, PhD Thesis, Amherst, University of Massachusetts, 1999.
- [10] Antoniszyn G.: *Parametric analysis of steel shell embedded in soil*, Drogownictwo, 2004, No. 4, pp. 135–139.
- [11] Machelski Cz., Antoniszyn G.: *Influence of live loads on the soil-steel bridges*, Studia Geotechnica et Mechanica, 2004, Vol. XXVI, No. 3–4, pp. 91–119.
- [12] Machelski Cz.: *Application of kinematic method to indicate the influence of internal forces on rod systems* (in Polish), Inżynieria i Budownictwo, 1998, No. 7, pp. 372–375.
- [13] Vaslestad J.: *Soil structure interaction of buried culverts*, Institutt for Geoteknikk, Norges Tekniske Hogskole, Universitetet I Trondheim, 1990.
- [14] Abdel-Sayed G., Bakht B.: *Soil-steel structure design by the Ontario Code: Part 2. Structural considerations*, Canadian Journal of Civil Engineering, 1981, Vol. 8, No. 3, pp. 331–341.
- [15] *Handbook of Steel Drainage & Highway Construction Products*, Corrugated Steel Pipe Institute & American Iron and Steel Institute, Second Canadian Edition, 2002.
- [16] Machelski Cz., Michalski B.: *Deformations of soil-steel bridges* (in Polish), Drogi i Mosty, 2005, No. 2, pp. 91–110.
- [17] Kunecki B., Kubica E.: *Full-scale laboratory tests and FEM analysis of corrugated steel culverts under standardized railway load*, Archives of Civil and Mechanical Engineering, 2004, Vol. IV, No. 4, pp. 41–53.

Intensywność obciążenia wycinka obwodowego mostowej konstrukcji gruntowo-powłokowej

Do obliczeń konstrukcji gruntowo-powłokowych wykorzystuje się specjalistyczne oprogramowanie oparte na modelu dwuwymiarowym (2D). Siły skupione pochodzące od pojazdów, będące obciążeniem jezdni obiektu mostowego, są w tym modelu sprowadzane z zastosowaniem teorii Boussinesq'a do wydzielonego wycinka. Teoria Boussinesq'a nie oddaje w pełni istoty pracy (siły wewnętrzne) mostowych układów gruntowo-powłokowych jako konstrukcji podatnych, współpracujących z gruntem w przenoszeniu obciążeń zewnętrznych. W pracy poddano ocenie skuteczność tej teorii w odniesieniu do modelu 3D utworzonego z elementów MES.

W tym celu dla wybranego pasma powłoki stalowej opracowano algorytm porównawczy oparty na funkcjach wpływu sił wewnętrznych. W wyniku przeprowadzonej analizy wykazano

wpływ ogólnych parametrów geometrycznych obiektu (szerokość, rozpiętość) na siły wewnętrzne, które są pomijane w wytycznych projektowania tych mostów. Analizę parametryczną podaną w pracy odniesiono do wybudowanego klasycznego mostu o konstrukcji gruntowo-powłokowej. Jako zmienne charakterystyki obiektu przyjęto: grubość zasypki gruntowej, rozpiętość powłoki, promień naroża, rodzaj falowania blachy oraz grubość blachy stosowanych typów powłok. Wykazano, że część z nich wpływa w stopniu istotnym na układ sił wewnętrznych. Wyniki analizy dotyczące charakterystyk geometrycznych stalowej powłoki wskazują, że można (teoretycznie) tak zmodyfikować te konstrukcje, aby zmniejszyć zużycie stali.

Information for Authors

Send to: *Archives of Civil and Mechanical Engineering*
Polish Academy of Sciences, Wrocław Branch
Podwale 75, 50-449 Wrocław, Poland

Archives of Civil and Mechanical Engineering (ACME) publishes both theoretical and experimental papers which explore or exploit new ideas and techniques in the following areas: structural engineering (structures, machines and mechanical systems), mechanics of materials (elasticity, plasticity, rheology, fatigue, fracture mechanics), materials science (metals, composites, ceramics, plastics, wood, concrete, etc., their structures and properties, methods of evaluation), manufacturing engineering (process design, simulation, diagnostics, maintenance, durability, reliability). In addition to research papers, the Editorial Board welcome: state-of-the-art reviews of specialized topics, letters to the Editor for quick publication, brief work-in-progress reports, brief accounts of completed doctoral thesis (one page is maximum), and bibliographical note on habilitation theses (maximum 250 words). All papers are subject to a referee procedure, except for letters, work-in-progress reports and doctoral and habilitation theses, which are briefly reviewed by the Editorial Board.

The papers submitted have to be unpublished works and should not be considered for publication elsewhere.

The Editorial Board would be grateful for all comments on the idea of the journal.

Submit three copies, each complete with abstract, tables, and figures.

Detailed information about the Journal on web:

<http://www.pan.wroc.pl>

www.ib.pwr.wroc.pl/wydzial/czasopismoACME.html

<http://www.wmech.pwr.wroc.pl>

Price 14 zł
(0% VAT)

Subscription orders should be addressed to:
Oficina Wydawnicza Politechniki Wrocławskiej
Wybrzeże Wyspiańskiego 27
50-370 Wrocław